Investigation of the hydrodynamics of a two component lattice Bhatnagar-Gross-Krook fluid.

THOMPSON, Stephen Peter.

REFERENCE

INVESTIGATION OF THE HYDRODYNAMICS OF A TWO COMPONENT LATTICE BHATNAGAR-GROSS-KROOK FLUID

STEPHEN PETER THOMPSON, BSc (Hons.)

A thesis submitted in partial fulfilment of the requirements

of Sheffield Hallam University for the degree of

Doctor of Philosophy

3 October, 1999

Materials Research Institute, Sheffield Hallam University.

Abstract

We present results from a computer simulation of an immiscible two component fluid, using a Lattice Boltzmann BGK $D2Q9$ scheme. Each fluid component is identified by a colour tag (either red or blue), and the immiscible behaviour arises from the implementation of colour segregation imposed on the lattice fluid. For two dimensional, microcurrent free planar interfaces between the two immiscible fluids we derive expressions for static interfacial tensions and interfacial distributions of the two fluids. Extending our analysis to curved interfaces, we propose a scheme for incorporating the influence of interfacial microcurrents that is based upon general symmetry arguments and is correct to second order in lattice velocity. The analysis demonstrates that the interfacial microcurrents have only second order influence upon the macroscopic behaviour of the model. We find good agreement between our calculations and simulation results based on the microcurrent stream function and surface tension results from the pressure tensor or Laplace law.

We examine the tangential stress transmission in the immiscible interface, by the investigation of the relationship between fluid shear and fluid viscosity across a planar symmetric interface. We find comprehensive agreement with theory, for the tangential hydrodynamic boundary condition. The examination of normal stress transmission in our two dimensional simulation is facilitated from correct behaviour of tangential stress. We develop a Fourier analysis technique which allows a quanti-

tative analysis of the anisotropy of the interface. This technique has facilitated the development of a further modification to the interface perturbation, which improves the macroscopic surface tension isotropy and reduces the magnitude of the parasitic microcurrent.

As an application of our model we simulate the induced deformation and burst of neutrally buoyant fluid drops subjected to external simple shear and solenoidal irrotational flow. Qualitatively the drops are seen to deform and orientate correctly, with respect to the external flow. Measuring the dependence of critical shear rate for drop rupture on flow parameters, our results validate the method over a range of simulation variables. The model's interfacial tension parameter σ, undeformed drop radius R, and BGK relaxation parameter ω are all found to have the correct influence upon the burst process as required by hydrodynamic theory. We note that the macroscopic surface tension and fluid viscosity are coupled, however this does not limit the application of the model.

Publications

This thesis contains work published in the following journals:

Induced Burst of Fluid Drops in a Two-Component Lattice BGK Fluid, I. Halliday, C.M.Care, S.P. Thompson and D. White, Physical Review E., Vol. **54** (3) pp. 2573–2576 1996.

Macroscopic Surface Tension in a Lattice Bhatnagar Gross Krook Model of Two Immiscible Fluids, I. Halliday, S.P. Thompson and C.M.Care, Physical Review E., Vol. **57** (1) pp. 514–523 1998.

Mesoscopic Hydrodynamics of a Diphasic Lattice Bhatnagar Gross Krook Fluid Interfaces, S.P. Thompson, I. Halliday and C.M.Care, Physical Chemistry and Chemical Physics, The Royal Society of Chemistry, Vol. **1** pp. 2183–2190 1999.

Acknowledgements

The body of this work would not have been possible without the help and constant support of those around me. Firstly, I must thank my parents Peter and Brenda Thompson for always being there, topping up my enthusiasm whenever needed and providing the inevitable financial support throughout my numerous years of study. I am also indebted to my partner and best friend Lynn. There are so many things I need to thank her for that are impossible to put into words. Thank you Lynn for your love, faith and encouragement. I would like to thank my brother Paul for his friendship and my oldest friends Dean Maude for suggesting that university would be fun and a good idea and Ian Bowers for buying me a beer when I was at my poorest.

It has been a great pleasure to work for Ian Halliday, who has nurtured my strengths, increased my vocabulary and endured my shortcomings, with his characteristic good humour and patience. Working for Ian has been an experience I will never forget. I would also like to thank very much Chris Care for his support and his excellent work in championing the virtues of the modelling lab.

I am very grateful to all those who have made me feel so welcome in Sheffield and made my time so enjoyable. In particular to my good friends; Stuart Mills for his off-road cycling trips and Moroccan Chicken, Darren Cammack for the Enchiladas and eternal good spirits and Steve McHugh for the use of the Edgecumbe Ranch and of course the cheese. Thanks also to Darren White, Tom Dalby, Martin Callaway, Richard Bemrose and Adrian Craven for all their help over the years.

Contents

Chapter 1

Introduction

In this thesis we present the analysis and application of a newly developed lattice Boltzmann BGK model similar to one proposed by Gunstensen *et al.* [1], for the simulation of immiscible two component fluid flow. The development of a computationally efficient technique, for modelling two component flows of engineering importance is the long term aim of this research.

The simulation of multi–component flows is a challenging problem with considerable technological and theoretical interest. Traditional finite–element and finite–volume schemes used in computational fluid dynamics (CFD) [2] struggle to accurately track interfaces efficiently. CFD schemes are most suited to tracking single component macroscopic variables such as fluid density ρ, velocity $\mathbf{u}$ and temperature T. Only recently have new techniques been developed to examine droplet deformation and breakup, employing CFD techniques [3, 4]. The strengths of CFD lie in the macro-

scopic simulation of single component, turbulent, large eddy and multiphase mixture approximation flows, with major applications in aerodynamics.

In Molecular Dynamics simulations of fluids [5], the individual fluid molecules are modelled and the interactions between colliding molecules are calculated from Newtons laws of motion in order to simulate flow. This requires the updating of position and velocity for each molecule from their previous positions at small time step intervals. The simulation of several hundred molecules becomes computationally expensive and produces information on a scale of only fractions of a second [6]. This has resulted in the development of novel numerical schemes, which bridge the macroscopic numerical schemes of CFD and the Molecular Dynamics representations of systems. Borrowing ideas from both techniques, to allow the simulation of fluid systems at a meso–scopic, scale which is both computational efficient for large systems and inherently tracks individual particles. These lattice gas and lattice Boltzmann models exhibit correct macroscopic hydrodynamic behaviour whilst requiring greatly reduced numbers of particles and computer memory. Subsequently, these competitor schemes have been developed and applied to areas where traditional simulation techniques have failed. Lattice Boltzmann models are particularly suited to the simulation of complex fluid interfaces as they do not explicitly track interfaces, but intrinsically track the underlying fluid particles themselves, allowing distinctions to be made between different fluid components.

The motivation to use computer simulation as an aid to understanding engineering problems and specifically fluid dynamics, is simply that they allow exact results to

be calculated. Computer simulation may be used as a testing ground for theories and the results may be compared with experiment. Finally and most importantly the results are not only of academic interest, but are often technologically useful and relevant.

1.1 Aims

In this thesis we develop a new immiscible lattice Boltzmann LBGK scheme to simulate immiscible two component fluid flow. The main aims of this research are

- to develop a computationally efficient immiscible two component lattice Boltzmann model and undertake appropriate analysis to examine the models surface tension.
- to develop a test procedure which may be employed to investigate and test the hydrodynamic boundary conditions of our model and other immiscible Lattice techniques.
- to apply the model to an industrially relevant engineering application.

1.2 Summary of thesis

In chapter 2 we investigate the single component lattice gas (LG) and lattice Boltzmann (LB) models and their extension to model immiscible fluid components. We

highlight the advantages of the lattice Boltzmann technique for the simulation of two component flows and examine the different ways an immiscible interface may be generated. The applications of the technique for the study of drop deformation and flow in porous media is then examined, to highlight the versatility of the model to simulate flows of engineering importance.

In chapter 3 the lattice Boltzmann BGK scheme is introduced and extended to simulate two immiscible fluid components. The implementation of the technique is described and issues relating to the computational efficiency of the scheme are discussed.

In chapter 4 expressions for the static interfacial tension between the immiscible fluids in simple plane interfaces are developed. This analysis is then extended to incorporate curved interfaces. We compare our calculations with simulation results and perform pressure tensor and Laplace law tests to confirm hydrodynamics.

In chapter 5 we examine the tangential and normal stress transmission in the immiscible interface, by developing a Fourier based analysis technique. A quantitative analysis of the isotropy of the interface is then made. Following this investigation, we introduce a modification to the interface perturbation, which improves the macroscopic surface tension isotropy.

In chapter 6 we simulate an application of the model, to induced droplet deformation and burst under simple shear flows. These results are then compared with experiment.

Chapter 2

Immiscible lattice fluid models

2.1 Introduction

In this chapter an examination of different immiscible lattice gas (LG) and lattice Boltzmann (LB) models is made. All of the techniques are extensions of the original lattice gas single component fluid models [7]. The extensions are made through the inclusion of a modified collision operation creating surface tension at the interface between fluids of differing species or through a modification of the equilibrium distribution function. Athermal and thermal interface generating models are examined along with benchmark tests and physical applications of these techniques. The chapter concludes with a brief look at other numerical schemes used to simulate immiscible fluids. The interested reader is also directed to the excellent review by Rothman and Zaleski [8], although this review is now some years old.

2.2 Foundations of the two component models

Immiscible lattice Boltzmann models have been evolved as algorithmic extensions to LG and LB models, developed as novel numerical techniques to investigate incompressible fluid flow. Extensive review papers are at present in press [8, 9, 10, 11] which examine applications and developments in LG and LB models. We refer readers to these papers and make only a brief introduction of the single component LG and LB models in this thesis.

2.2.1 The HPP Model

Hardy, Pomeau and de Pazzis (HPP) [12, 13] introduced the first lattice gas model. Idealised particles are restricted to move on a square lattice, whose links connect neighbouring sites by unit vectors $\mathbf{c}_i$ where $i = 1..4$. Particles propagate at unit speed, moving from one lattice site to a neighbouring site in discrete time steps. An exclusion principle is applied, permitting only one particle to travel along a link with a particular velocity at one time. When particles arrive at a site they are collided according to a set of pre–determined collision rules. These collision rules are designed to conserve particle number and momentum. It was found that the square lattice was not isotropic enough to allow for the simulation of a real fluid, this leads to the development of a model using a more isotropic lattice.

2.2.2 The FHP Model

Frisch, Hasslacher and Pomeau (FHP) [7] introduced in 1986 a lattice gas model based on a hexagonal lattice. The FHP model is the simplest lattice gas model, that is capable of recovering the continuity and Navier-Stokes equations. Idealised particles are propagated and collided on a lattice and an exclusion rule is applied preventing simultaneous occupation of any link by more than one particle travelling with the same velocity. Each lattice site is connected to its six nearest neighbours by unit vectors $\mathbf{c}_i$ where $i = 1..6$ and the occupancy of the link is denoted by a six-bit state $n_i(\mathbf{x}, t)$ where $n_i = 1(0)$ indicates the presence (or absence) of a particle. Rest particles may also be introduced into the model residing on the lattice sites, with a velocity $\mathbf{c}_0$ and they may interact with other particles arriving at that site during the collision process.

As time is evolved discretely, the particles move one link in the direction of their velocity and collide with incoming particles. Examples of different particle collisions on the FHP lattice are shown in Figure 2.1, a full explanation of these collisions is given in the figures caption. We note the dynamics of the FHP model are invariant under all discrete translations, mirror symmetries and rotations of $\frac{\pi}{3}$. Both deterministic and non-deterministic collision rules are implemented and are designed to conserve mass and momentum. The collision rules must be carefully chosen to prevent spurious particle conservations [7], for in the case of head-on collisions see Figure 2.1 (A), not only particles number is conserved, but the difference in particles number in any pair of directions is also conserved.

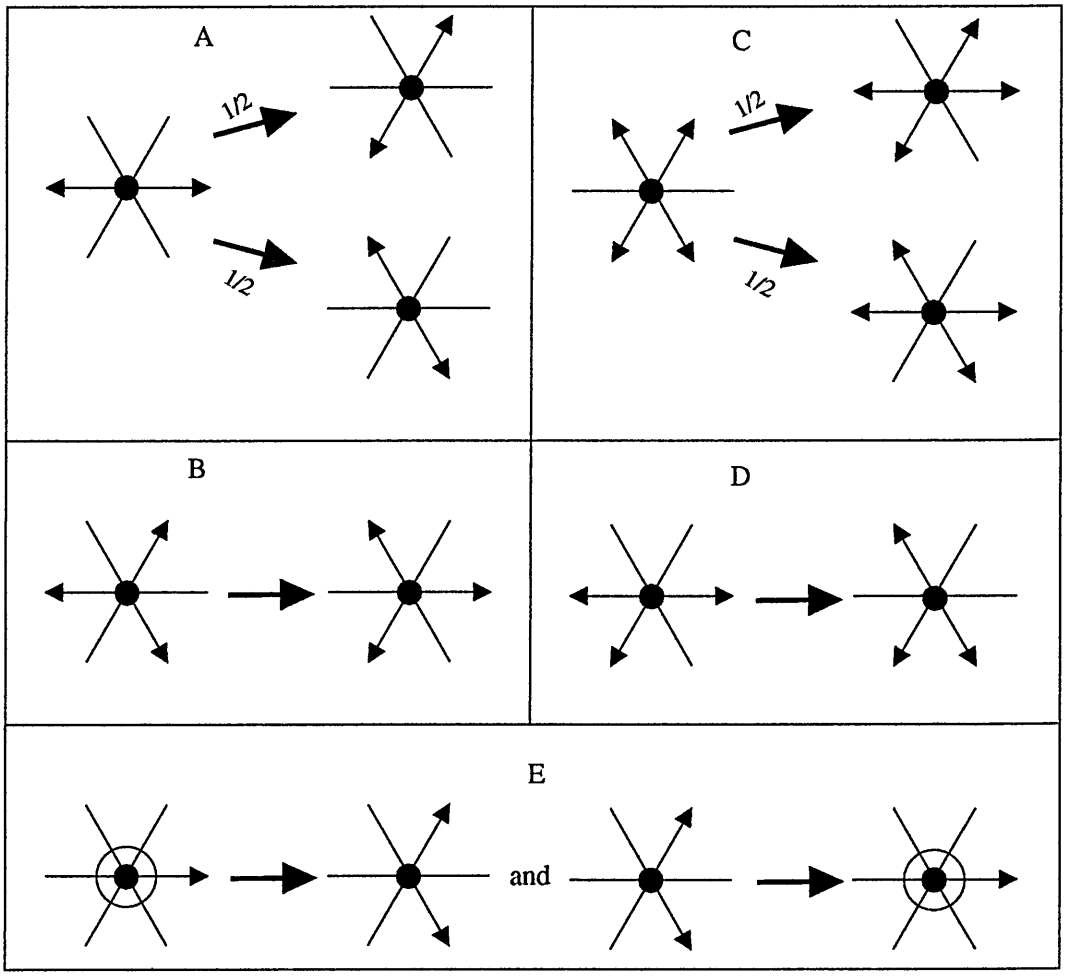

Figure 2.1: Collision rules for FHP models: (A) head–on collision with two possible output channels; (B) triple collision; (C) dual of head–on collision; (D) head–on collision with spectator; (E) collisions involving a rest particle (represented by a circle)

The simplest FHP model FHP-I may be constructed without the inclusion of rest particles. The model contains simply head-on collisions of two and three particles see Figure 2.1 (A) & (B). The more complex FHP II and FHP III models may be constructed which include rest particles and an extended collision set involving collisions with upto five particles.

2.2.3 The FCHC Model

The FHP model was extended to three dimensions by d'Humieres [15]. As there is no regular three dimensional lattice with enough symmetry to recover hydrodynamics, a face-centred-hypercubic (FCHC) four dimensional lattice is used and projected into three dimensions. This produces a multi-speed model and particles may now have a velocity of zero (rest), one, or $\sqrt{2}$. The propagation of particles is unchanged from the FHP model and collisions are again designed to conserve mass and momentum.

2.2.4 Lattice Gas dynamics

The evolution of the lattice gas model is described by the evolution equation

$$n_i(\mathbf{x}+\mathbf{c}_i, t+1) = n_i(\mathbf{x}, t) + \Delta_i(n) \tag{2.1}$$

where $n_i(\mathbf{x}+\mathbf{c}_i, t+1)$ denotes the time incremented occupancy of link i and $\Delta_i(n)$ represents the change in $n_i(\mathbf{x}, t)$ due to collisions with other particles. Two macroscopic variables may be extracted at each lattice site in order to map the lattice gas onto hydrodynamics. These are the local fluid density ρ, and momentum $\rho\mathbf{u}$.

$$\rho(\mathbf{x}, t) = \sum_i n_i(\mathbf{x}, t) \tag{2.2}$$

$$\rho(\mathbf{x}, t)\mathbf{u} = \sum_i n_i(\mathbf{x}, t)\mathbf{c}_i \tag{2.3}$$

The full derivation of the lattice gas model is presented by Frisch *et al.* [7], to which we direct the interested reader. We note however, by performing a Taylor expansion of the evolution equation Eq. (2.1) and substituting an equilibrium solution for the

mean population following statistical mechanics, the model may be proved to recover approximately the incompressible Navier- Stokes after performing asymptotic expansions and considerable algebra. The equations for lattice gas hydrodynamics are only valid for low velocity flows $\mathbf{u} \ll c_s$ the speed of sound in the model, which is assumed during the derivation. Frisch considers the lattice fluid density to be a constant ρ_0 in all terms except the pressure term.

$$\partial_\alpha u_\alpha = 0 \tag{2.4}$$

$$\partial_t u_\alpha + g(\rho_0) u_\beta \partial_\beta u_\alpha = -\frac{1}{\rho_0}\, \partial_\alpha \left[p - p_0 g(\rho_0) u^2\right] + \nu(\rho_0) \partial_{\beta\beta} u_\alpha \tag{2.5}$$

where pressure $p = \rho c_s^2$, $p_0 = \rho_0 c_s^2$ and $g(\rho_0) = \frac{1}{2}\left[\frac{b-2\rho}{b-\rho}\right]$ and b is the number of link directions.

The derived Navier Stokes equations for the lattice gas differ from the standard equation by containing a density dependent function $g(\rho_0)$ in the advective term, a fluid viscosity dependent upon fluid density and finally an additional term in the fluid pressure which is density and velocity dependent. Frisch employs a re-scaling technique to redefine the pressure and obtain the correct Navier Stokes equation where

$$t^* = g(\rho_0)\, t \tag{2.6}$$

$$\nu^*(\rho_0) = \frac{\nu(\rho_0)}{g(\rho_0)} \tag{2.7}$$

$$p^* = \frac{1}{g(\rho_0)}\left[p - p_0 g(\rho_0) \frac{u^2}{c^2}\right] \tag{2.8}$$

producing the rescaled Navier Stokes equation

$$\partial_{t^*} u_\alpha + u_\beta \partial_\beta u_\alpha = -\frac{1}{\rho_0}\, \partial_\alpha p^* + \nu^*(\rho_0) \partial_{\beta\beta} u_\alpha \tag{2.9}$$

a similar re-scaling technique has also been employed by Wolfram [16] to recover correct hydrodynamics.

Lattice gas models are a useful numerical method for the simulation of hydrodynamic flows. They allow simple inclusion of solid boundaries, by the introduction of modified collision rules on designated boundary sites. For example, non–slip boundary conditions may be introduced by forcing any particle colliding with a solid boundary to be reflected [17]. However the lattice gas possesses a number of problems which restrict their use for computing hydrodynamic flows.

Limitations of the lattice gas

The discrete nature of the lattice gas particles results in a high level of statistical noise, which requires temporal and spatial averaging in order to obtain useful statistics. More importantly the lattice gas suffers from a lack of Galilean invariance, resulting in the $g(\rho_0)$ term in the Navier Stokes equations Eq.(2.5). For a single component fluid, the lack of Galilean invariance may be overcome by using a re-scaling technique. However, for a multi-component fluid the re-scaling techniques introduce a $g(\rho_0)$ term into the diffusion equation [18], preventing the correct modelling of a two component system. Setting $g(\rho_0) = 1$ [18] produces Galilean invariance at only one density, preventing the modelling of any density variation between fluid components. We note that the necessity of the re–scaling technique limits the application of the lattice gas, as a constant density is required due to density dependence of the lattice fluid pressure and viscosity.

2.2.5 The lattice Boltzmann model

The lattice Boltzmann model [19] has evolved from the lattice gas, in order to more successfully simulate fluid behaviour and follows the Boltzmann approximation that particles are uncorrelated. In the LB model the boolean particles of the lattice gas model are replaced with an ensemble average $N_i =< n_i >$ mean particle distribution (or population) where $0 \leq N_i \leq 1$. This development overcomes the statistical noise present within the lattice gas. The LB scheme may be used in an analogous manner to the LG model, however the collision operator still depends on the input and output states of the lattice gas. In the case of the FCHC model, the collision operator is a $24^2 \times 24^2$ matrix. The size of the matrix can be considerably reduced [20, 21] by expanding the particle distribution around the equilibrium particle distribution N_i^{eq}, where

$$N_i^{eq} = N_i - N_i^{neq} \tag{2.10}$$

and N_i^{neq} is the non-equilibrium distribution and $N_i^{eq} \gg N_i^{neq}$. However two more computationally efficient lattice Boltzmann schemes exist which we now introduce, these are the enhanced collision linearised lattice Boltzmann and the lattice BGK schemes.

2.2.6 The Enhanced collision Linearised LB model

Higuera *et al.* [21] develop a collision operator Ω_{ij} which is constructed from conservation and lattice isotropy. The evolution equation of the scheme is given by

$$N_i(\mathbf{x}+\mathbf{c}_i, t+1) = N_i(\mathbf{x}, t) + \Omega_{ij} N_j^{neq}(\mathbf{x}, t) \tag{2.11}$$

The collision operator Ω_{ij} represents the change through collisions of N_i with N_j. The isotropy of the hexagonal lattice results in Ω_{ij} being solely dependent upon the angle between link i and j, the angular values being $0^0, 60^0, 120^0, 180^0$. For a model without rest particles Ω_{ij} consist of only four terms. The inclusion of rest particles introduces two new terms to Ω_{ij} to account for the interaction between rest particles Ω_{00} and the interaction between moving and rest particles Ω_{0j} where $j > 0$.

The conservation of mass and momentum by the collision process imposes constraints on the elements a_{ij}, of Ω_{ij}, where a_θ denotes the angle between link i and j giving

$$6b + c = 0 \tag{2.12}$$

$$a_0 + 2a_{60} + 2a_{120} + a_{180} = 0 \tag{2.13}$$

$$a_0 + a_{60} - a_{120} - a_{180} = 0 \tag{2.14}$$

where b is the number of lattice links and c is the link length. The non zero eigenvalues of the hexagonal lattice are

$$\lambda = 6(a_0 + a_{60}) + 2b \tag{2.15}$$

$$\sigma = -6(a_0 + 2a_{60}) - 3b \tag{2.16}$$

$$\tau = -7b \tag{2.17}$$

λ is the most important eigenvalue as it controls the fluid kinematic viscosity with the general form

$$\nu = -\frac{c^2}{D+2}\left(\frac{1}{\lambda}+\frac{1}{2}\right) \tag{2.18}$$

where $0 \geq \lambda \geq -2$ and D is the dimensionality of the lattice.

2.2.7 Lattice Boltzmann BGK model

Qian *et al.* [23] and Chen *et al.* [24] introduce the Bhatnagar Gross Krook (BGK) [22] based collision operation. By assuming that the particle distribution N_i relaxes to an equilibrium value at a constant rate the collision term is given by

$$\Omega_i = -\frac{1}{\tau}[N_i - N_i^{eq}] \tag{2.19}$$

The evolution of the BGK scheme is given by

$$N_i(\mathbf{x}+\mathbf{c}_i, t+1) = (1-\omega)N_i(\mathbf{x},t) + \omega N_i^{eq}(\mathbf{x},t) \tag{2.20}$$

where $\omega = \frac{1}{\tau}$ the reciprocal of the relaxation time. In the BGK model the equilibrium distribution N_i^{eq} has a Maxwell-Boltzmann distribution [25], as it does not employ an exclusion rule as seen in the previous lattice models where a Fermi–Dirac distribution has been used to simplify particle collisions. The BGK scheme has been shown to satisfy the Navier-Stokes equations to second order of approximation. The speed of sound c_s and kinematic viscosity ν are given by

$$c_s = \frac{1}{\sqrt{3}}, \qquad \nu = \frac{1}{6}\left[\frac{2}{\omega}-1\right] \tag{2.21}$$

Qian notes that the physical requirement of a positive viscosity gives the condition for numerical stability of $0 \leq \omega \leq 2$. The BGK scheme is shown to be algorithmically

simple and computationally efficient to implement. It is therefore chosen as our underlying fluid model with which we will examine interfacial hydrodynamics. A fuller derivation of the BGK scheme is given in Chapter 3.

2.3 Two dimensional immiscible models

Rothman and Keller [26] introduce a fundamental extension to the original work on lattice gas models by Frisch *et al.*, simulating an immiscible two component fluid by evolving red $r_i(\mathbf{x})$ and blue $b_i(\mathbf{x})$ coloured particles on a hexagonal lattice. The coloured particles are allowed to reside at the same lattice site and follow the exclusion principle. The collision of these particles aims to model the short–range intermolecular forces that exist in real fluids and which result in drop coalescence and cohesion. Neighbouring lattice sites surrounding a colour interface are used to influence the evolution of the interface.

A colour field is defined to be a direction weighted sum of differences between the number of red and blue particles at a site

$$\mathbf{f}(\mathbf{x}) = \sum_i \mathbf{c}_i \sum_j [r_j(\mathbf{x}+\mathbf{c}_i) - b_j(\mathbf{x}+\mathbf{c}_i)] \tag{2.22}$$

A local colour flux $\mathbf{q}(\mathbf{x})$ is also defined, as the local measure of net momentum difference at a site

$$\mathbf{q}[r(\mathbf{x}), b(\mathbf{x})] = \sum_i \mathbf{c}_i [r_i(\mathbf{x}) - b_i(\mathbf{x})] \tag{2.23}$$

At interfacial sites the work W performed by the colour flux against the colour field is then minimised, subject to the constraints of colour, mass and momentum

conservation. Hence like (unlike) coloured particles feel an attractive (repulsive) force.

$$W(r,b) = -\mathbf{f}.\mathbf{q}(r,b) \tag{2.24}$$

The collision process smooths colour surfaces and produces drop coalescence of like coloured particles. The evolution of a periodic lattice containing equal numbers of randomly distributed coloured particles, sees the merger of small drops to form larger drops, the final equilibrium state is reached when the two colours completely separate and produce a plane horizontal interface spanning the lattice.

Rothman uses a Laplace law bubble test to prove qualitatively that the simulation produces surface tension. The test was performed by initialising a lattice with a fluid drop of radius R and measuring the change in pressure $\Delta p = p_1 - p_2$ between the fluid drop pressure p_1 and it's surrounding fluid pressure p_2 and plotting this value against the reciprocal radius R in the range of $16 < R < 48$ where surface tension is denoted by σ.

$$\Delta p = p_1 - p_2 = \frac{\sigma}{R} \tag{2.25}$$

Adler [27] calculates theoretically the surface tension in a Rothman–Keller interface. The surface tension is calculated as a function of particle density using a Boltzmann approximation for simple planar interfaces in two dimensions. An investigation of interface fluctuations is also conducted. A Boltzmann approximation is made in order to estimate the ensemble link density at the interface, it is then compared with simulation results. A qualitative fit to the simulation data, shows that the Boltzmann approximation allows a good estimate of surface tension to be made.

The calculations are noted to be useful in determining any anisotropy in the surface tension, due to interface geometry. The equilibrium fluctuations (which are absent in LB simulations) are found to be in agreement with predictions for classical interfaces. This indicates that at equilibrium the interface behaves like a real interface, this assumption excludes of course any anisotropy measured in the surface tension due to lattice orientation.

Chen *et al.* [28] introduce a different lattice gas technique to model immiscible fluids. They employ a nearest neighbour colour density in order to model the attraction between like coloured particles. Coloured particles are collided at an interface in such a way as to move particles in the opposite direction to a local coloured hole flux. The coloured hole represents a *memory* of a particle moving in the same direction prior to a collision. A local flux $\mathbf{G}$ is calculated for the coloured particles and a local flux $\mathbf{F}$ for the holes

$$\mathbf{G} = \sum_i (2f_i - 1)N_i \mathbf{c}_i \tag{2.26}$$

$$\mathbf{F} = \sum_i (2f_i - 1)(1 - N_i)\mathbf{c}_i \tag{2.27}$$

where $f_i = 1$ (0) denotes a red (blue) colour tag and $N_i = 1$ (0) denotes a particle (hole) and collisions are chosen to maximise $Q = -\mathbf{F}.\mathbf{G}'$. $\mathbf{F}$ is calculated for the input hole state (pre-collision) and $\mathbf{G}'$ is calculated from the output particle state. Thus, coloured particles move in the direction opposite to the local colour-hole flux, extending nearest neighbour particle interaction to several lattice lengths. Local information is noted to be carried in the collision step, reducing the look–up table size in the algorithm and increasing the computational speed. The model is seen to

exhibit phase separation when evolved from an equal number of randomly initialised coloured particles, forming at steady state a stable strip configuration. In the case of the simulation of a fluid drop the induced surface tension conforms to a Laplace law test. Interestingly an examination of the pressure jump across a circular drop interface is seen to produce a broad pressure transition region centrally located around the colour interface, of width ≈ 16 lattice sites.

Gunstensen *et al.* [1, 29] introduce a lattice Boltzmann approach to the simulation of multi component flows. The model is an extension of the earlier immiscible lattice gas model introduced by Rothman and Keller [26]. A two component fluid is simulated by evolving red R_i and blue B_i particle densities on a hexagonal lattice, where the total particle density at a site is given by $N_i = R_i + B_i$.

A post collision perturbation is added to collided particle densities to produce a locally anisotropic fluid pressure near to the immiscible interface so that the Laplace formula can be approximately recovered. Like the Rothman model this happens at the interface between a designated red and blue fluid. The added perturbation has the physical effect of creating surface tension between the differing fluid components, whilst retaining adherence to the Navier-Stokes equations governing hydrodynamics in the bulk fluid. Gunstensen uses a Galilean invariant, linearised LB scheme as developed by Higuera *et al.* [20, 21], as the underlying lattice fluid model. The immiscible fluid is simulated as red and blue fluid particles and the collision rules are modified to conserve particle colour at a site as well as particle mass and momentum. The collision rules re–orientate coloured particles and send them to

neighbouring sites of the same colour. The perturbation to the densities is followed with a recolouring step to increase colour segregation and minimise diffusion at the interface.

A fluid interface is located by examining the colour field gradient

$$\mathbf{f}(\mathbf{x}) = \sum_i \mathbf{c}_i \left[M_\mathbf{c} \left[R_0(\mathbf{x}+\mathbf{c}_i) - B_0(\mathbf{x}+\mathbf{c}_i) \right] + \sum_j \left[R_j(\mathbf{x}+\mathbf{c}_i) - B_j(\mathbf{x}+\mathbf{c}_i) \right] \right] \quad (2.28)$$

where $M_\mathbf{c}$ is the number of rest particles residing at the site. The magnitude of the colour gradient $|\mathbf{f}|$ is large near to an interface and small in the bulk single fluid component. The colour field angle $\theta_f = tan^{-1}(f_y/f_x)$ gives the normal to the interface and θ_i is defined to be the angle subtended from the horizontal by the link i. At sites where $|\mathbf{f}| > \epsilon$, where ϵ is a small number determining the existence of an interface, a perturbation is added to the collided density N_i'

$$N_i'' = N_i' + A|\mathbf{f}|cos(\theta_i - \theta_f) \quad (2.29)$$

where A is a perturbation parameter. Mass moving parallel to the interface is depleted by the perturbation and preferentially relocated to perpendicular links. The perturbation is of course subject to the constraints of mass, momentum and colour conservation at that site. The re–orientation of the mass is followed by a recolouring step, which minimises the work $W = -\mathbf{f}.\mathbf{q}$ performed by the colour flux

$$\mathbf{q}(\mathbf{x}) = \sum_i (R_i''(\mathbf{x}) - B_i''(\mathbf{x}))\mathbf{c}_i \quad (2.30)$$

against the colour field direction. This forces coloured densities to move towards their own coloured species.

Gunstensen investigated the behaviour of the surface tension induced in the two component model at planar interfaces by making a discrete approximation to the mechanical definition of surface tension [30]

$$\sigma = \int_{-\infty}^{\infty} (P_N - P_T) dz \tag{2.31}$$

where P_N (P_T) is the normal (tangential) component of pressure and z is the direction perpendicular to the interface. A plane interface was simulated on a hexagonal lattice with interface orientations of angle 0^0 and 30^0. Simulation measurements of surface tension were taken and found to agree well with theoretical predictions [1]. A Laplace law bubble test was also employed to investigate a static steady state drop. The change in pressure Δp between a fluid drop and it's surrounding fluid was measured and plotted against the reciprocal radius R^{-1} of the drop. The internal and external drop pressures were calculated as an average of the pressure at $0.7R$ and $1.3R$ respectively. Good agreement with theory was found over a drop radius range of $8 < R < 64$ with correct system scaling. The Laplace law examination of a static drop fluid interface has become a benchmark test employed by all workers to test surface tension.

Grunau *et al.* [31] expands the immiscible LB model of Gunstensen by simulating fluid components with differing viscosities and molecular weights. A single time relaxation LB [24] (BGK) scheme is used as the underlying fluid model, as this method is more efficient and requires less memory than the linearised scheme previously employed. The density ratio between the fluid components is implemented through the use of different values of red m_R and blue m_B ensemble averaged rest particles.

Following [24] the equilibrium distribution N_i^{eq} is taken as

$$N_i^{eq} = \rho_k \left[\frac{1}{6+m_k} + \frac{1}{3}\,\mathbf{c}_i\mathbf{u} + \frac{2}{3}\,(\mathbf{c}_i\mathbf{u})^2 - \frac{1}{6}\mathbf{u}^2 \right] \tag{2.32}$$

$$N_0^{eq} = \rho_k \left[\frac{m_k}{6+m_k} - u^2 \right] \tag{2.33}$$

where the k subscript refers to the fluid component colour (red or blue). The scheme assumes that the interface is stable and non–separating and the density ratio γ between the fluid components is given by

$$\gamma = \frac{\rho_R}{\rho_B} = \frac{6+m_R}{6+m_B} \tag{2.34}$$

In order to create a smooth transition in the fluid viscosity across the fluid interface, the order parameter ψ is defined

$$\psi = \frac{\rho_R - \rho_B}{\rho_R + \rho_B} \tag{2.35}$$

where $\psi = 1$ ($\psi = -1$) for a pure red (blue) fluid component. Outside an interface region the relaxation time of the fluid is τ_R (τ_B) for the red (blue) component. Within a finite region surrounding the interface of width δ, the averaged (effective) relaxation is given by a combination of the two

$$< \tau >= \frac{2\tau_R\tau_B}{\tau_R + \tau_B} \tag{2.36}$$

Shan and Chen [32] introduce a new lattice Boltzmann model for simulating flows with multiple fluid components. This new model differs from previous immiscible models as it allows for the incorporation of an extension to allow for thermodynamic phase interactions. The nonlocal interactions between different fluid components are modelled by introducing a nonlinear interaction potential, of the form

$$V(\mathbf{x},\mathbf{x}') = G_{\sigma\bar{\sigma}}(\mathbf{x},\mathbf{x}')\psi^{\sigma}(\mathbf{x})\psi^{\bar{\sigma}}(\mathbf{x}') \tag{2.37}$$

where $\psi^\sigma = F^\sigma(n^\sigma)$ is an effective number density for fluid component σ. $G_{\sigma\bar{\sigma}}(\mathbf{x}, \mathbf{x}')$ is a Greens function and is analagous to the surface tension perturbation parameter A used by Gunstensen, which controls the interaction strength

$$G_{\sigma\bar{\sigma}}(\mathbf{x} - \mathbf{x}') = 0, \qquad |\mathbf{x} - \mathbf{x}'| > c \tag{2.38}$$

$$G_{\sigma\bar{\sigma}}(\mathbf{x} - \mathbf{x}') = G_{\sigma\bar{\sigma}}, \qquad |\mathbf{x} - \mathbf{x}'| = c \tag{2.39}$$

where c is the lattice constant. The potential's repulsion and attraction is controlled by its sign and the induced momentum change at each site is defined as

$$\frac{dp^\sigma}{dt}(\mathbf{x}) = -\psi^\sigma(\mathbf{x}) \sum_{\bar{\sigma}=1}^{s} G_{\sigma\bar{\sigma}} \sum_i \psi^{\bar{\sigma}}(\mathbf{x} + \mathbf{c}_i)\mathbf{c}_i \tag{2.40}$$

The momentum at each site is redefined to include the addition of the momentum change of each fluid component

$$\rho^\sigma(\mathbf{x})u^{eq}(\mathbf{x}) = \rho^\sigma(\mathbf{x})u(\mathbf{x}) + \tau_\sigma \frac{dp^\sigma}{dt}(\mathbf{x}) \tag{2.41}$$

and $u^{eq}(\mathbf{x})$ is substituted into the equilibrium distribution N_i^{eq} replacing $u(\mathbf{x})$. $\rho^\sigma(\mathbf{x}) = m^\sigma n^\sigma(\mathbf{x})$ is the mass density and m^σ is the molecular mass of the fluid component σ. Shan notes that the momentum of the system differs from earlier models [8, 1] as it is conserved globally but not locally due to the addition at each site of the momentum derivative. Numerical results are presented for a hexagonal liquid–gas model in which the fluid undergoes a first order phase transition, this phase transition occurs when $\frac{dp^\sigma}{dt}$ goes negative. When the model is used to simulate two component flow, the $G_{\sigma\bar{\sigma}}$ factor is set to a value large enough to produce negative diffusion, hence phase separation. Shan uses the standard Laplace law test to verify the models hydrodynamics.

2.3.1 Thermodynamic interface generation

Swift *et al.* [33] and Orlandini *et al.* [34, 35] introduce models for the simulation of immiscible fluid components and liquid–gas phases. The interface generation is made possible by modifying the equilibrium distribution N_i^{eq} and adding extra terms

$$N_i^{eq} = N_i^{eq} + F_\alpha c_{i\alpha} + G_{\alpha\beta} c_{i\alpha} c_{i\beta} \tag{2.42}$$

Two distributions N_i and Δ_i are evolved using the BGK scheme where

$$\rho = \rho_R + \rho_B = \sum_i N_i(\mathbf{x}, t) \tag{2.43}$$

$$\Delta\rho = \rho_R - \rho_B = \sum_i \Delta_i(\mathbf{x}, t) \tag{2.44}$$

Suitable modification of co–efficients inside the equilibrium distribution is made to ensure mass and momentum conservation from [23] and

$$\sum_i N_i^{eq} c_{i\alpha} c_{i\beta} = P_{\alpha\beta} + \rho u_\alpha u_\beta \tag{2.45}$$

$$\sum_i \Delta_i^{eq} c_{i\alpha} c_{i\beta} = \Gamma \Delta\mu \delta_{\alpha\beta} + \Delta\rho u_\alpha u_\beta \tag{2.46}$$

where the thermodynamics of the model is governed by the pressure tensor $P_{\alpha\beta}$ and chemical potential between the two components $\Delta\mu$ and Γ is the mobility. The free energy describing two ideal gases, with a repulsive interaction energy is chosen to determine the thermodynamic properties of the model, and has the general form

$$\Psi(\mathbf{r}) = \int d^2\mathbf{r} \left[\psi(T, \rho, \Delta\rho) + \frac{\kappa}{2}(\nabla\rho)^2 + \frac{\kappa}{2}(\nabla\Delta\rho)^2 \right] \tag{2.47}$$

where T is the temperature and

$$\psi(T, \rho, \Delta\rho) = \frac{\Lambda}{4}\left(1 + \frac{\Delta\rho^2}{\rho^2}\right) - T\rho + \frac{T}{2}(\rho + \Delta\rho)\, log\left(\frac{\rho + \Delta\rho}{2}\right) + \frac{T}{2}(\rho - \Delta\rho)\, log\left(\frac{\rho - \Delta\rho}{2}\right) \tag{2.48}$$

Λ is the interaction strength and κ is the interfacial energy. The chemical potential and pressure are given by [30]

$$\Delta\mu(T,\rho,\Delta\rho) = -\lambda\frac{\Delta\rho}{\rho} + Tlog\left(\frac{1+\frac{\Delta\rho}{\rho}}{1-\frac{\Delta\rho}{\rho}}\right) \tag{2.49}$$

$$P_{\alpha\beta} = p_0\delta_{\alpha\beta} + \kappa\partial_\alpha\rho\partial_\beta\rho + \kappa\partial_\alpha\Delta\rho\partial_\beta\Delta\rho \tag{2.50}$$

and

$$p_0 = \rho T - \frac{\kappa}{2}\left(\rho\nabla^2\rho + \Delta\rho\nabla^2\rho\right) - \frac{\kappa}{2}\left(|\nabla\rho|^2 + |\Delta\nabla\rho|^2\right) \tag{2.51}$$

2.4 Three dimensional immiscible models

Olson and Rothman [36] introduce a three dimensional immiscible lattice gas model for simulating binary fluids. The model uses an FCHC lattice and surface tension is activated following Rothman and Keller, through the calculation of a colour field $\mathbf{f}(\mathbf{x})$ and colour flux $\mathbf{q}(\mathbf{x})$. Olson introduces a computationally efficient *dumbbell scheme* in order to calculate the maximisation of the work done by the colour flux against the colour field. This maximisation is pre–calculated and stored in *look up* tables, making the scheme computationally efficient. The scheme generates strong surface tension with a high degree of isotropy. The model has been applied to measurements of the effective viscosity of phase–separating mixtures under going simple shear.

Martys [37] adopts the segregation rule developed by Shan and Chen *et al.* [32] and uses a single time relaxation scheme (LBGK) in D3Q19 space, as the underlying lattice fluid model. A gravity force is added to the lattice fluid, and tested by

simulating Poiseuille flow driven by a constant gravitational field. A constant body force such as gravity is introduced by modifying the fluid momentum giving

$$\rho^{\sigma}\mathbf{u}'(\mathbf{x}) = \rho^{\sigma}(\mathbf{x})[\mathbf{u}(\mathbf{x}) + \tau_{\sigma}g] \tag{2.52}$$

where g is the gravitational constant (or body force). The Poiseuille flow test produces a parabolic flow profile along the channel, when bounce-back boundary conditions are used at the channel edges, producing zero velocity at the channel walls. However, these boundary conditions must be carefully implemented to produce at solution of required accuracy [38]. Martys further studies the interaction between wetting and non-wetting fluids and solid boundaries, by studying multicomponent flow in porous media, further explanation of this application is left to the end of this chapter. The Shan and Chen model has also been used for further studies of diffusion by Shan *et al.* [39] and liquid-gas phase transitions [40].

2.5 Physical applications

Immiscible LB models have been used to simulate a wide range of complex interfaces such as domain growth in spinodal decomposition in binary fluids [31, 41] and lamellar fluids [34, 42]. We now highlight in more detail two areas of current engineering research interest centred on immiscible fluid, these are drop deformation and flow in porous media.

2.5.1 Drop deformation

Halliday and Care [43] investigated the steady state hydrodynamics of an immiscible drop deformed under simple shear flow by using the interface segregation rule developed by Gunstensen. They found at moderate shears that the drops elongated and orientate to the flow as seen by experiment, implying qualitatively realistic incompressible hydrodynamic behaviour. Drops are seen to deform under shear with the expected functional dependence upon the far field shear rate and surface tension, and obey Laplace law. They also note that the segregation method induces *microcurrents* close to the interface, the magnitude of these microcurrents is noted to be small, compared with the shear rates employed to deform the drops. It is noted that correct hydrodynamic behaviour is expected from the drops when the fluid shear is greater than flow induced by these microcurrents, thus restricting the lower limit of shear rate which may be investigated.

Wagner and Yeomans [45] use a variant of Swifts thermal LB developed by Orlandini [35], to investigate the effects of shear flow on an equilibrium droplet in a phase separated binary mixture. Drops were deformed under a simple shear flow and seen to elongate and orientate at an angle α to the flow. Under moderate shear, the drop deformation was seen to be proportional to induced shear rate. The fluid shear was implemented in two different ways to access the effect of periodic drop images upon deformation. In the first method the top and bottom of the lattice were constrained to induce the shear, whilst lattice side edges employed periodic boundary conditions. This scheme effectively produces the simulation of an infinite line of fluid

drops, allowing the transmission of a drop wake across the periodic boundary. In the second scheme all boundary edge sites were constrained to produce the shear flow by modifying the equilibrium particle distribution and explicitly setting the velocity. Close quantitative and excellent qualitative agreement was found between the two schemes.

Schelkle [46] employs the Shan and Chen model [32] to investigate droplet–droplet collisions in $3D$. Flows are characterised by a Weber number $We = \rho(2\mathbf{u})^2 d/\sigma$ where d is the drop diameter and $\mathbf{u}$ is the initial drop velocity. A dimensionless impact parameter $B = b/d$ is also used to represent the excentricity of collisions, where $B = 0$ for central collisions and $0 < B < 1$ for non–central collisions and b is a collision parameter. Central and non–central collisions between two fluid drops are investigated at low velocity $u = 0.15$ units per time step. At $B = 0.33$ drops are seen to coalesce on impact producing a torus–like single droplet with a thin surface in its centre. The surface tension of the drop is seen to collapse this configuration to a peanut–shaped structure, which is seen to oscillate and rotate around the drops centre of gravity. The drop viscosity is noted to damp this oscillation finally producing a spherical droplet. At $B = 0.47$ above a critical value $B^* = 0.4$ which is confirmed by experiment, the drop coalescence after collision is seen to neck and burst into two drops of equal size and produce a small satellite drop at the centre of gravity.

2.5.2 Flow in porous media

Gunstensen [1] reported an application of his model to two component flow in porous media. A lattice was initialised with impermeable blocks of square side length in the range 4 to 12 lattice units, creating a series of channels along the lattice. Non slip "bounce-back" boundary conditions were applied to all solid boundaries, with periodic boundary conditions used at two opposite boundaries allowing flow to be induced by creating a pressure difference across the length of the lattice. The minimum channel width was set to 6 lattice sites wide and filled with a red coloured wetting red fluid which was invaded by the introduction of a blue fluid. Pockets of trapped red fluid were produced as capillary effects prevented the invading blue fluid from entering the narrowest channels. A time evolution produces a qualitatively realistic flow and Gunstensen notes that the lattice Boltzmann scheme is ten times faster than the immiscible lattice gas, as it requires no averaging to obtain statistics. The model has also been extended to simulate three component flow in porous media [29].

Martys [37] models the fluid–wall interaction by introducing an interaction force where $s = 0$ or $s = 1$ for a pore or a solid respectively.

$$\mathbf{f}^{\sigma}(\mathbf{x}) = -\rho^{\sigma}(\mathbf{x}) \sum_{i} G_i^{\sigma} s(\mathbf{x} + \mathbf{c}_i)\mathbf{c}_i \tag{2.53}$$

Adjustment of the interaction strength G_i^{σ} to a positive value for non-wetting fluids or negative for a wetting fluid, allows the fluid–wall wetting to be controlled. The wetting angle θ of the fluid may be controlled by adjusting the interaction strength G_i^{σ}, where θ is defined as the angle made at the point of fluid–solid interface. The

porous media simulated was derived from experimental studies of a Fontainebleau sandstone. Two different types of flow were examined using the model, in the first an invading non–wetting fluid is introduced to the porous media displacing a wetting fluid. Quasi–periodic boundary conditions were implemented in the direction of the induced flow, recolouring particles as they re–enter the system as the correct invading fluid, conserving momentum and system volume. In the second case, a wetting invading fluid is used to displace a non–wetting fluid. For non-wetting invasion, the invading fluid pushes out the wetting fluid by entering pores and filling the cavity in an analagous manner to an expanding balloon. Thus the wetting fluid is pushed out of the pore except near to the solid surface. The invasion of the wetting fluid is seen to trap the non–wetting fluid preventing it's escape through smaller pores. The collected results for these simulations are consistent with experiment.

2.6 Other immiscible models

Coveney and Novik [47] investigate immiscible fluids by using Dissipative Particle Dynamics [48] (DPD) as the underlying fluid model. The DPD scheme is as an *off–lattice* meso–scale modelling technique, maintaining the discrete time–stepping element and evolution of particle densities in the same way as the lattice Boltzmann scheme. This greatly accelerates the algorithm compared with more traditional Molecular Dynamics (MD) techniques [5]. The extension of DPD to model two component flow is made in an analagous manner to the LB scheme, by introducing a *colour tag* to distinguish particles of different components. Identically coloured

particles are then modelled using the same interaction, whilst the mean and variance of the random variable Π_{ij} controlling particle interaction is increased when differently coloured particles interact. The model was found to obey Laplace law for simple two dimensional bubble experiments, confirming the existence of surface tension between fluid components.

Lafaurie *et al.* [3] model surface tension in $2D$ and $3D$ flows using a traditional computational fluid dynamics (CFD) volume of fluid method (VOF). Surface tension is introduced as a correction to the momentum stress tensor. The correction is constructed from local gradients of the volume fraction, producing an anisotropic pressure at the fluid interface between differing components, this method was inspired by the interface generating techniques developed by Gunstensen *et al.* [1]. The fluid interface is evolved by using a combination of *upwind* and *downwind* fluxing schemes, the choice of which is dependent upon the interface orientation with respect to the direction of flow. The downwind scheme is employed when the interface is perpendicular to the direction of the flow, whilst the upwind scheme is implemented when the interface is parallel to the flow. This choice is made due to the differing effects the fluxing schemes have upon the stability of the interface.

The interface is located by using a volume fraction function C where $C = 1$ (0) inside fluid 1 (inside fluid 2). The upwind scheme produces a stable but diffusive interface, whilst the downwind scheme is known to be unstable, but is good at interface tracking. The tracking schemes are chosen by the calculation of $\theta_k = acos(n_k)$, where n_k is the local approximation to the interface normal $\mathbf{n} = \frac{\nabla^h C}{|\nabla^h C|}$

and $\nabla^h C$ is a finite difference approximation to the volume fraction gradient. The upwind (downwind) scheme is implemented when $\theta_c < \theta_k$ ($\theta_c > \theta_k$), where θ_c is the critical angle between the horizontal axis and the interface normal. Simulations of droplet–droplet collisions in $2D$ and $3D$ were performed and Laplace law was verified for the model. Algorithm tests show evidence of *parasite currents* (microcurrents), which are found to scale with surface tension in the same way as [29].

Zaleski *et al.* [4] study the breakup of $2D$ liquid patches in a surrounding gas environment using a similar VOF method [3], at moderate Reynolds number $Re = 1000$. The simulations were used to examine the nonlinear relationship between the deforming drop and the induced droplet wake.

2.7 Summary

Algorithmically the simplest and most robust of the LB methods is the lattice Boltzmann BGK method, which has isotropy and Galilean invariance directly embedded into a technique benefiting from a simple collision step. The BGK scheme has successfully been shown to recover single phase hydrodynamics. For these reasons we construct a new two component immiscible lattice Boltzmann (BGK) model based upon a particular variant (D2Q9) of the BGK scheme and incorporating an extension of a simple and computationally efficient interface segregation technique developed by Gunstensen [1]. The Gunstensen interface is chosen due to it's singular nature, making it appropriate for the simulation of two component hydrodynamics. The

thermodynamic interface of Orlandini *et al.* , produces a broad non–singular interface, which is unsuited to the simulation of small radii drops. The Shan and Chen interface whilst being singular, requires the fluid components to be slightly immiscible for the scheme to be numerically stable. We note this is only a slight problem and at the time this research was started neither the Gunstensen or Shan and Chen interfaces provided any known distinct advantages over each other. The Gunstensen interface was therefore chosen as it could properly simulate completely immiscible fluid components. Immiscible lattice Boltzmann models have previously been applied to applications such as droplets under shear to demonstrate qualitatively correct steady–state interfacial hydrodynamic boundary conditions [43].

Chapter 3

Lattice BGK Scheme

3.1 Introduction

In this chapter the lattice BGK (LBGK) $D2Q9$ scheme is firstly introduced and then modified to produce our two–component immiscible LBGK model. The single–component LBGK scheme is based upon the BGK simplification of the Boltzmann equation, constrained to lie upon a discrete lattice. The LBGK scheme may be viewed as an alternative to lattice gas (LG) model [7] and a simplification of the linearised lattice Boltzmann (LLB) [20, 21] method. We follow the method of Hou *et al.* [49] to derive the macrodynamical governing equations, summarising the main results in this chapter.

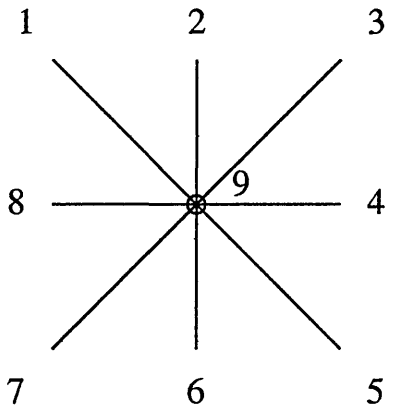

Figure 3.1: Schematic representation of the $D2Q9$ lattice

3.2 Discrete velocity LBGK $D2Q9$ scheme

The LBGK $D2Q9$ scheme employs a discrete underlying square orthogonal lattice with unit lattice spacing. Each lattice node is connected to its nearest neighbours by eight lattice link directions (velocities) $\mathbf{c}_i$ where $i = 1..9$ (where $i = 9$ is a stationary rest link) see Figure 3.1. The lattice links are populated by particle distributions which reside on the lattice nodes at integer times, and stream from node to node along the lattice links in unit time steps. The $D2Q9$ lattice contains particle distributions that move at two different speeds along the unit length links $c = 1$ and along the longer $c = \sqrt{2}$ diagonal links. The lattice also contains rest particles that reside on the lattice nodes. The particle distributions residing on the lattice may be loosely thought of as ensemble averages of the discrete boolean particles of the LG.

The occupation of the lattice links by particle distributions is represented by the particle distribution function $N_i(\mathbf{x}, t)$. The distribution function may be thought of

as the probability of finding a "particle" at position $\mathbf{x}$ at time t and link i. Two macroscopic quantities may be extracted at each node in the form of a lattice density ρ and momentum $\rho\mathbf{u}$.

$$\rho = \sum_i N_i(\mathbf{x}, t) \tag{3.1}$$

$$\rho\mathbf{u} = \sum_i N_i(\mathbf{x}, t)\mathbf{c}_i \tag{3.2}$$

3.2.1 Lattice evolution equation

The evolution of the LBGK scheme may be expressed in the Boltzmann form with a collision term replaced by a single–time relaxation towards an equilibrium population denoted by N_i^{eq}

$$\frac{\partial N_i}{\partial t} + \mathbf{c}_i.\nabla N_i = -\frac{1}{\tau}(N_i - N_i^{eq}) \tag{3.3}$$

The left hand side of Eq. (3.3) represents the propagation of the particles and the right hand side represents the collision between particles as they propagate from node to node. The discrete Boltzmann equation describes the microscopic scale flow of link densities and allows the derivation of the Navier–Stokes equations governing fluid flow at macroscopic scales. This derivation requires averaging over the discrete velocities, and the use of the Chapman-Enskog multiscale expansion.

Particle distributions are relaxed towards an equilibrium distribution by performing a *collision* process employing mass, momentum and energy conservation, mimicking an ideal particle collision. The evolution of this process is termed the lattice

evolution equation and is defined as

$$N_i(\mathbf{x} + \mathbf{c}_i, t + 1) = N_i(\mathbf{x}, t) + \Omega_i \tag{3.4}$$

where Ω_i is a collision operator representing the rate of change of the particle distribution due to collisions. According to Bhatnagar, Gross and Krook (BGK) [22] the collision operator is simplified by using the single time relaxation approximation

$$N_i(\mathbf{x} + \mathbf{c}_i, t + 1) - N_i(\mathbf{x}, t) = -\frac{1}{\tau}(N_i(\mathbf{x}, t) - N_i^{eq}(\mathbf{x}, t)) \tag{3.5}$$

where τ is the single relaxation time which controls the rate of approach to equilibrium. The BGK relaxation parameter is the simplest collision operator that can produce Navier–Stokes behaviour in the subsonic limit.

3.2.2 Chapman–Enskog expansion

The Chapman–Enskog expansion is used to derive a set of partial differential equations in terms of mass ρ and momentum $\rho\mathbf{u}$, that describe the lattice fluid in the limit of Δx and δ tending to zero, where δ is the small lattice time unit and Δx is the small lattice distance. The expansion assumes that $\Delta x/\delta = c$ is a constant, and that the ratio of V/c is small where V is the macroscopic velocity of the fluid. The expansion recovers the mass continuity equation and the Navier–Stokes equations.

Link densities N_i may be written as the sum of contributions on increasing length scales, each contribution being labelled by analogy with a power series using higher orders of δ.

$$N_i = N_i^0 + \delta N_i^1 + \delta^2 N_i^2 + ... \tag{3.6}$$

The small lattice time unit δ may be thought of as a small Knudsen number (the ratio of mean free path to the characteristic flow length). This assumes of course that the mean free path is the same order as δ. The shortest scale in the expansion is of order $\delta^0 = 1$ and is the same scale as the equilibrium distribution. In the equilibrium distribution gradients are considered negligible and significant gradients are considered to occur in lattice quantities of $O(\delta)$ and above, these gradients are relaxed towards equilibrium by the collision process.

3.2.3 Equilibrium particle distribution

The equilibrium particle distribution $N_i^{(0)}$ which will be referred to as N_i^{eq} from now on, is the link density of a uniformly translating lattice fluid. Thus no gradients of any variable are contained within the distribution. The equilibrium particle distribution is therefore only a function of velocity $\mathbf{u}$ and link direction $\mathbf{c}_i$. The general form of N_i^{eq} is therefore taken as

$$N_i^{eq}(\mathbf{x}, t) = A + B(\mathbf{c}_i.\mathbf{u}) + C(\mathbf{c}_i.\mathbf{u})^2 + D\mathbf{u}^2 \tag{3.7}$$

where A, B, C and D are coefficients yet to be determined, which are dependent upon the speed of the lattice link and node density ρ. The general form of N_i^{eq} has the appearance of a velocity expansion to $O(u^2)$.

3.2.4 Isotropy

The *D2Q9* scheme requires the symmetric tensors of even order to be known for the derivation of the macrodynamical equations. The odd order tensors are known to equal zero. The reader may satisfy themselves by considering the simplest case of an odd order tensor - the first order tensor

$$\sum_i c_{i\alpha} = 0 \tag{3.8}$$

summation of the x and y components of this tensor may be easily calculated see Appendix A Figure A.1. Calculation of the second and fourth order tensors only is required, as for the present model there is no requirement for isotropy of tensors above fourth order.

$$\sum_i c_{i\alpha} c_{i\beta} = 2c^2 \delta_{\alpha\beta} \tag{3.9}$$

$$\begin{aligned} \sum_i c_{i\alpha} c_{i\beta} c_{i\gamma} c_{i\delta} &= 2\delta_{\alpha\beta\gamma\delta} && \text{for } \sigma = 1 \\ &= 4\Delta_{\alpha\beta\gamma\delta} - 8\delta_{\alpha\beta\gamma\delta} && \text{for } \sigma = 2 \end{aligned} \tag{3.10}$$

where σ is the square modulus of the link velocity, $\delta_{\alpha\beta\gamma\delta} = 1$ for $\alpha = \beta = \gamma = \delta$, and 0 otherwise and $\Delta_{\alpha\beta\gamma\delta} = (\delta_{\alpha\beta}\delta_{\gamma\delta} + \delta_{\alpha\gamma}\delta_{\beta\delta} + \delta_{\alpha\delta}\delta_{\beta\gamma})$.

3.2.5 Conservation laws

Before establishing the macrodynamical equations for the LBGK scheme, consideration of the higher–order contributions to the link density is required. Constraints are imposed to prevent the non–equilibrium distributions (i.e. orders $n \geq 1$), con-

tributing to the macroscopic variables ρ and $\rho\mathbf{u}$.

$$\rho = \sum_i N_i^{eq}(\mathbf{x}, t) \tag{3.11}$$

$$\rho\mathbf{u} = \sum_i N_i^{eq}(\mathbf{x}, t)\mathbf{c}_i \tag{3.12}$$

for $n \geq 1$.

$$\sum_i N_i^n(\mathbf{x}, t) = 0 \tag{3.13}$$

$$\sum_i N_i^n(\mathbf{x}, t)\mathbf{c}_i = 0 \tag{3.14}$$

Thus constraints are imposed on the constants A, B, C, and D allowing the determination of relations between our unknown coefficients. For example the local density may be evaluated by the summation of $N_i^{eq}(\mathbf{x}, t)$ over i giving the relation

$$A_0 + 4A_1 + 4A_2 = \rho \tag{3.15}$$

where A_0, A_1 and A_2 are the associated values of A for the different speed links.

3.3 Macrodynamical governing equations

The macrodynamical governing equations are derived by firstly performing a Taylor expansion up to second–order $O(\delta^2)$ of the evolution equation

$$N_i(\mathbf{x} + \delta\mathbf{c}_i, t + \delta) - N_i(\mathbf{x}, t) = -\frac{1}{\tau}(N_i(\mathbf{x}, t) - N_i^{eq}(\mathbf{x}, t)) \tag{3.16}$$

where δ is the small lattice time unit, giving the form

$$\delta\left[\frac{\partial}{\partial t} + (\mathbf{c}_i.\nabla)\right]N_i + \frac{\delta^2}{2}\left[\frac{\partial}{\partial t} + (\mathbf{c}_i.\nabla)\right]^2 N_i = -\frac{1}{\tau}(N_i(\mathbf{x}, t) - N_i^{eq}(\mathbf{x}, t)) \tag{3.17}$$

Expanding the particle distribution about N_i^{eq}

$$N_i = N_i^{eq} + \delta N_i^1 + \delta^2 N_i^2 + ... \tag{3.18}$$

To examine gradients on different time scales, t_0 and t_1 are introduced as $t_0 = t$ and $t_1 = \delta t$

$$\frac{\partial}{\partial t} = \frac{\partial}{\partial t_0} + \delta \frac{\partial}{\partial t_1} + ... \tag{3.19}$$

We now consider the basic conservation equations correct to $O(\delta)$ and $O(\delta^2)$. Substituting Eqs. (3.18) and (3.19) into Eq. (3.17), and evaluating to order $O(\delta)$

$$(\partial_{t_0} + c_{i\alpha}\partial_\alpha) N_i^{eq} = -\frac{1}{\tau} N_i^{(1)} \tag{3.20}$$

Evaluating to order $O(\delta^2)$ gives

$$\partial_{t_1} N_i^{eq} + \left(1 - \frac{1}{2\tau}\right)(\partial_{t_0} + c_{i\alpha}\partial_\alpha) N_i^{(1)} = -\frac{1}{\tau} N_i^{(2)} \tag{3.21}$$

3.3.1 Mass conservation

Summing Eq. (3.20) over i we may write the continuity equation to $O(\delta)$

$$\partial_{t_0}\rho + \partial_\alpha(\rho u_\alpha) = 0 \tag{3.22}$$

Summing Eq. (3.21) over i, obtains equations correct to $O(\delta^2)$

$$\partial_{t_1}\rho = 0 \tag{3.23}$$

3.3.2 Momentum conservation

Multiplying Eq. (3.20) by $c_{i\alpha}$ and summing over i yields the following conservation of momentum equation,

$$\partial_{t_1}(\rho u_\alpha) + \partial_\alpha \Pi^{eq}_{\alpha\beta} = 0 \tag{3.24}$$

where $\Pi^{eq}_{\alpha\beta}$ is termed the *momentum flux tensor* given by

$$\Pi^{eq}_{\alpha\beta} = \sum_i N_i^{eq} c_{i\alpha} c_{i\beta} \tag{3.25}$$

The correct form of the continuity equation is recovered if we add Eq. (3.21) to $\delta\times$ Eq. (3.24) and recombine the time derivatives using Eq. (3.18), to give

$$\partial_t \rho + \partial_\alpha(\rho u_\alpha) = 0 \tag{3.26}$$

The momentum flux tensor term $\Pi^{eq}_{\alpha\beta}$, may be evaluated by substituting into its definition the general form for the equilibrium distribution Eq. (3.7) and using the isotropy relations of Eqs. (3.9,3.10) $\Pi^{eq}_{\alpha\beta}$ becomes

$$\Pi^{eq}_{\alpha\beta} = c_s^2 \rho \delta_{\alpha\beta} + \rho u_\alpha u_\beta \tag{3.27}$$

If Eq. (3.27) is substituted back into Eq. (3.22) the Euler equation is recovered to $O(\delta)$,

$$\partial_{t_0} \rho u_\alpha + \partial_\beta \rho u_\alpha u_\beta = -\partial_\alpha p \tag{3.28}$$

where the pressure $p = c_s^2 \rho$. Summing Eq. (3.21) over i, obtains equations correct to $O(\delta^2)$

$$\partial_{t_0}(\rho u_\alpha) + \partial_\alpha \left(1 - \frac{1}{2\tau}\right) \Pi^{(1)}_{\alpha\beta} = 0 \tag{3.29}$$

The non–equilibrium momentum flux term $\Pi^{(1)}_{\alpha\beta}$ must also be evaluated to enable the $O(\delta^2)$ equations to be fully derived. Substituting for $N_i^{(1)}$ in the definition of $\Pi^{(1)}_{\alpha\beta}$ and using a rearranged form of Eq. (3.19) and then a further substitution for N_i^{eq} is needed using Eq. (3.7). After considering isotropy and removing the non-isotropic term by selecting suitable values for coefficients, $\Pi^{(1)}_{\alpha\beta}$ can now be written

$$\begin{aligned}\Pi^{(1)}_{\alpha\beta} &= -\tau\left[\left(\frac{1}{3}-c_s^2\right)\partial_\gamma(\rho u_\gamma)\delta_{\alpha\beta}+\frac{1}{3}\partial_\alpha(\rho u_\beta)+\frac{1}{3}\partial_\alpha(\rho u_\beta)\right.\\ &\qquad \left.-u_\alpha\partial_\beta(c_s^2\rho)-u_\beta\partial_\alpha(c_s^2\rho)-\partial_\gamma(\rho u_\alpha u_\beta u_\gamma)\right] \qquad (3.30)\end{aligned}$$

By combining Eq. (3.28) with $\delta\times$ Eq. (3.25), substituting for $\Pi^{(1)}_{\alpha\beta}$ and selecting a speed of sound,

$$c_s^2=\frac{1}{3} \qquad (3.31)$$

gives the momentum equation

$$\begin{aligned}\partial_t(\rho u_\alpha)+\partial_\beta(\rho u_\alpha u_\beta) &= -\partial_\alpha(c_s^2\rho)+\frac{\rho\delta}{6}\left(\frac{2\tau-1}{6}\right)\partial_\beta(\partial_\alpha\rho u_\beta+\partial_\beta\rho u_\alpha)\\ &\qquad -\delta\partial_\beta\left(\tau-\frac{1}{2}\right)\partial_\gamma(\rho u_\alpha u_\beta u_\gamma)+O(\delta^2). \qquad (3.32)\end{aligned}$$

3.4 Mapping onto incompressible hydrodynamics

The adherence of the LBGK scheme to incompressible hydrodynamics may be seen by mapping Eq. (3.26) and Eq. (3.32) onto the incompressible Continuity and Navier–Stokes equations respectively. The recovery of the Navier–Stokes equations relies upon the assumption that variations in the lattice density ρ are small and thus may be neglected in all but the pressure term, where $\rho \propto p$. For an incompressible

fluid in two dimensions the Navier–Stokes equations are given by

$$\partial_\alpha u_\alpha = 0 \tag{3.33}$$

$$\partial_t(\rho u_\alpha) + \partial_\beta(\rho u_\alpha u_\beta) = -\partial_\alpha p + \nu\partial_\beta(\partial_\alpha \rho u_\beta + \partial_\beta \rho u_\alpha) \tag{3.34}$$

where u is the real measurable fluid velocity. The third term of Eq. (3.32) is a nonlinear error term which is omitted. This allows the identification the kinematic viscosity ν and the pressure p terms as

$$\nu = \delta\left[\frac{2\tau - 1}{6}\right] \tag{3.35}$$

$$p = \frac{\rho}{3}. \tag{3.36}$$

If the equations with terms in δ are written in *lattice units* the δ's disappear. The lattice continuity equation also holds for incompressible flow if $\partial_\beta \rho$ may be assumed small. Therefore simulations at low Mach numbers $M = \frac{v}{c_s^2}$ are required in order to minimise compressibility effects, where v is a characteristic flow velocity.

3.4.1 Reynolds Number *Re*

A particular flow may be characterised by a dimensionless quantity called the Reynolds number

$$Re = \frac{Ul}{\nu} \tag{3.37}$$

where the fluid viscosity is given by ν and U and l are characteristic velocity and length scales of the flow respectively. The choice of U and l is dependent upon the system under study, in a single component channel flow U is often taken as the

average system velocity and l is taken as the channel width. In two component flow l is often taken as a fluid drop diameter.

3.5 Summary of the LBGK $D2Q9$ scheme

The LBGK evolution equation may be written following Qian *et al.* [23] where the collision term is replaced by a relaxation process in the form

$$N_i(\mathbf{x}+\mathbf{c}_i, t+1) = (1-\omega)N_i(\mathbf{x},t) + \omega N_i^{eq}(\mathbf{x},t) \tag{3.38}$$

where $\omega = \frac{1}{\tau}$. The general form of the equilibrium distribution N_i^{eq} is given by

$$N_i^{eq}(\mathbf{x},t) = t_p\rho\left[1 + \frac{\mathbf{c}_{i\alpha}u_\alpha}{c_s^2} + \frac{u_\alpha u_\beta}{2c_s^2}\left(\frac{\mathbf{c}_{i\alpha}\mathbf{c}_{i\beta}}{c_s^2} - \delta_{\alpha\beta}\right)\right] \tag{3.39}$$

where c_s^2 is the speed of sound and α and β represent the Cartesian coordinates of the underlying lattice. The equilibrium distribution N_i^{eq} for the $D2Q9$ scheme is given by

$$N_i^{eq}(\mathbf{x},t) = t_\sigma\rho\left[1 + 3\mathbf{u}\mathbf{c}_i + \frac{9}{2}(\mathbf{u}\mathbf{c}_i)^2 - \frac{3}{2}\mathbf{u}^2\right] \tag{3.40}$$

the index σ is the square modulus of the particle's velocity and the t_σ values are given by (see Figure 3.1 for i indexing)

$$\begin{aligned} t_0 &= \frac{4}{9} \quad \text{for } i\text{=9} \\ t_1 &= \frac{1}{9} \quad \text{for } i\text{=2,4,6,8} \\ t_2 &= \frac{1}{36} \quad \text{for } i\text{=1,3,5,7} \end{aligned} \tag{3.41}$$

The shear viscosity of the fluid is given by

$$\nu = \frac{1}{6}\left[\frac{2}{\omega} - 1\right] \tag{3.42}$$

The value of the relaxation parameter ω is chosen to lie in the range $0 \leq \omega \leq 2$, from the stability properties used in computational fluid dynamics (CFD) and the requirement for a positive viscosity. The LBGK schemes may be derived for other two and three dimensional geometries such as the hexagonal FHP (D2Q7) 7-speed model. All of the LBGK models share the same evolution equation and the general form of the equilibrium distribution N_i^{eq}. However the t_σ values differ for each model and in the case of the D2Q7 LBGK scheme the speed of sound is given by $c_s^2 = \frac{1}{4}$.

3.6 Two component LBGK model

In the two component LBGK model [1] densities which populate the lattice are designated either red or blue, $R_i(\mathbf{x}, t)$ ($B_i(\mathbf{x}, t)$) denoting the red (blue) density at position $\mathbf{x}$, time t moving in direction i. Multi-component fluid behaviour arises when segregation is imposed upon such densities by a generalisation of the BGK collision to three steps.

Firstly the usual BGK collision step re-distributes achromatic density

$$N_i(\mathbf{x}, t) \equiv R_i(\mathbf{x}, t) + B_i(\mathbf{x}, t) \tag{3.43}$$

to links using the scalar collision operator ω, which controls fluid shear viscosity through [23]

$$\nu = \frac{1}{6}\left[\frac{2}{\omega} - 1\right] \tag{3.44}$$

in the case of different fluid viscosities between red and blue fluid components an

effective viscosity ν_{eff} is calculated at interfacial sites

$$\nu_{eff} = \frac{\rho_R}{\rho}\,\nu_R + \frac{\rho_B}{\rho}\,\nu_B \tag{3.45}$$

where ρ_R (ρ_B) denotes the red (blue) density at a site. In the second collision step the local lattice fluid pressure tensor $P_{\alpha\beta}(\mathbf{x},t)$, is approximated [1] by

$$P_{\alpha\beta}(\mathbf{x},t) = \sum_i N_i(\mathbf{x},t) c_{i\alpha} c_{i\beta} \tag{3.46}$$

and is rendered anisotropic at interfacial sites by accumulating (denuding) density on links perpendicular (parallel) to an interface tangent. (The interfacial sites are those which include non-zero densities of both colours.) The motivation for this step is found by reference to the parent lattice gas techniques [26] and is a process not without foundation in hydrodynamics [30]. To achieve this redistribution we follow Gunstensen *et al* [1], and adjust $N_i(\mathbf{x},t)$ at mixed nodes by applying a density and momentum conserving perturbation of the form

$$\Delta N_i(\mathbf{x},t) = \sigma C(\mathbf{x},t) cos(2(\theta_f(\mathbf{x}) - \theta_i)) \tag{3.47}$$

where σ is a *surface tension parameter* controlling the amplitude of perturbations, angle θ_i is the angular orientation of link i and $\theta_f(\mathbf{x},t)$ is the direction of a *colour field* $\mathbf{f}(\mathbf{x},t)$, defined by:-

$$\mathbf{f}(\mathbf{x},t) = \sum_{ij} (R_j(\mathbf{x}+\mathbf{c}_i,t) - B_j(\mathbf{x}+\mathbf{c}_i,t))\mathbf{c}_i \tag{3.48}$$

We have also introduced into Eq. (3.47) a *concentration factor* $C(\mathbf{x},t)$

$$C(\mathbf{x},t) = 1 - \left| \frac{\rho_R(\mathbf{x},t) - \rho_B(\mathbf{x},t)}{\rho_R(\mathbf{x},t) + \rho_B(\mathbf{x},t)} \right| \tag{3.49}$$

where $\rho_R(\mathbf{x},t)$ ($\rho_B(\mathbf{x},t)$) denote the total of the red (blue) densities at the site. The incorporation of concentration factor Eq. (3.49) into the perturbation makes evolution outside the interfacial region exactly the same as in the single component fluid and removes the possibility of surface tension being activated by *one-colour* density gradients, which may occur close to an interface.

In a third and final step, nodal colour $\rho_B(\mathbf{x},t)$, $\rho_R(\mathbf{x},t)$, is allocated to link densities in that distribution which maximises the work done by *colour flux* $\mathbf{q}(\mathbf{x},t)$

$$\mathbf{q}(\mathbf{x},t) = \sum_i (R_i(\mathbf{x},t) - B_i(\mathbf{x},t))\mathbf{c}_i \tag{3.50}$$

against the colour field direction of $\mathbf{f}(\mathbf{x},t)$ [1]. Clearly to achieve maximum segregation as much red (blue) as possible should colour the density on the link $\mathbf{c}_j$ of largest (smallest) projection onto the direction of $\mathbf{f}(\mathbf{x},t)$. As the multi-speed nature of our lattice affects any prioritisation of links for colour allocation, an unambiguous hierarchy for red population of links $i = 1..9$ requires that $\mathbf{f}(\mathbf{x},t)$ be resolved into the 16 angular intervals identified in Figure 3.2. Rothman and Keller [26] employed a finer discretisation for the hexagonal lattice of 36 intervals, however, we employ a more simplistic discretisation which takes account of the difference in equilibrium density capacity and length of neighbouring links. Biasing allocation towards the lower capacity links, we may produce a computationally efficient reallocation table with a minimum number of members. Our scheme although coarse at the initial stages of interface evolution, biases allocation in such a way to increase the speed of approach to equilibrium by aligning the colour field more closely to the colour flux and preventing the colour field oscillating around the colour flux.

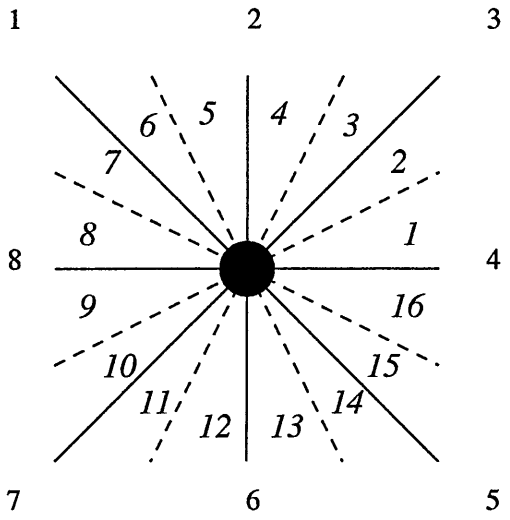

Figure 3.2: Index of the angular colour segment intervals at each interfacial site.

If $\mathbf{f}(\mathbf{x}, t)$ is found to lie in angular interval $Segment = 1$, the priority of allocation of red density in descending order is $i = 3, 4, 5, 2, 9, 6, 1, 8, 7$. The need to resolve $\mathbf{f}(\mathbf{x}, t)$ into 16 intervals emerges as one attempts to determine which of links $i = 2$ or $i = 5$ is *third* most favourable for red occupation, for such prioritisation can be made only after determining the direction onto which short link 2 and long link 5 have equal projection. The latter is specified by angle $\beta = 26.56^0$. Symmetry then requires that the positive quadrant is resolved into the four angular intervals shown (Figure 3.2).

Note that link $i = 9$ (rest) will always have priority 5. The propagate step in which all densities are translated by the appropriate velocity vector is carried-out in the usual way on each red and blue density.

3.6.1 Computational efficiency

As the LBGK is an iterative scheme we may improve the computational efficiency by careful consideration of the program algorithm and the use of pre–calculation and *look up tables.* At each iteration, particles are propagated along the lattice and this streaming may be pre–computed to store the iterated position of each particle as $N_i(\mathbf{x}, t) \rightarrow N_i(\mathbf{x}+\mathbf{c}_i, t+1)$. This may be achieved by storing in a two dimensional *integer* array, the new position of all particles in the system with respect to their present position and velocity. In the same way, a colour heirachy table is calculated and stored to reallocate colour and reduce diffusion, after the interface perturbation has been induced at interfacial sites see Appendix A. Figure A.2.

The calculation of the colour field and the colour flux both rely on the calculation of the difference between red and blue coloured densities at interfacial sites. By storing the coloured densities at each site in two separate memory arrays, the first we denote $\mathbf{N} = R_i + B_i$ stores the total mass on a link and the second **RBDiff**$= R_i - B_i$ the difference between red and blue density on a link, we may also improve the speed the algorithm calculates the colour field and colour flux.

3.6.2 Algorithm Summary

After the system has been initialised to the required initial colour configuration required to perform a particular simulation (*e.g.* a red drop in a supporting blue fluid to allow the deformation of the drop with respect to an external far field shear),

the following steps are iterated at each discrete time step to evolve and perform the simulation.

- Calculate $N_i(\mathbf{x}, t) = R_i(\mathbf{x}, t) + B_i(\mathbf{x}, t)$
- Calculate ρ and $\mathbf{u}$
- Colour Blind Collide
- Calculate colour field $\mathbf{f}(\mathbf{x}, t)$
- Calculate concentration factor $C(\mathbf{x}, t)$
- Perturb interface $\Delta N_i(\mathbf{x}, t) = \sigma C(\mathbf{x}, t) cos(2(\theta_f(\mathbf{x}) - \theta_i))$
- Calculate colour flux $\mathbf{q}(\mathbf{x}, t)$
- Recolour densities to minimise diffusion
- Induce required external flow
- Propagate particles

Chapter 4

Calculation of macroscopic surface tension

4.1 Introduction

In this chapter analysis of our interface generating algorithm is introduced and we examine the effect of the inclusion of a colour concentration factor into our interface perturbation scheme. Expressions for the macroscopic surface tension Σ and interfacial colour distributions are derived for *steady–state* static plane interfaces using lattice symmetry arguments and the mechanical definition of surface tension. This analysis is then extended to incorporate curved interfaces by including contributions from the interfacial microcurrent. Comparison is then made with simulation, by performing Laplace law simulations and investigating the microcurrent stream

function.

4.2 Effect of the enhanced interface perturbation

We employ a modified version of the perturbation scheme used by Gunstensen *et al.* to segregate two fluid components, by incorporating a newly introduced concentration factor $C(\mathbf{x}, t)$ given by

$$C(\mathbf{x}, t) = 1 - \left| \frac{\rho_R(\mathbf{x}, t) - \rho_B(\mathbf{x}, t)}{\rho_R(\mathbf{x}, t) + \rho_B(\mathbf{x}, t)} \right| \tag{4.1}$$

where ρ_R (ρ_B) is the red (blue) density at a site, giving the interfacial perturbation the form

$$\Delta N_i(\mathbf{x}, t) = \sigma C(\mathbf{x}, t) cos(2(\theta_f(\mathbf{x}) - \theta_i)) \tag{4.2}$$

where ΔN_i is the collided link distribution, σ is the surface tension parameter, θ_f is the colour field angle and θ_i is the angle subtended to the horizontal by link i. The introduction of the concentration factor Eq. (4.1) has the effect of making the evolution of the lattice fluid outside the interfacial (mixed–colour) region exactly the same as that of a single component LBGK fluid. Thus *surface tension* may not be activated by local one colour density gradients that are known to surround curved interfaces, as $C(\mathbf{x}, t) = 0$ for all pure sites. This is an improvement to the original scheme introduced by Gunstensen *et al.* where the interfacial perturbation was activated on all sites when $\mathbf{f} > \epsilon$, where the value of ϵ denoted the presence of an interface and had to be manually set. The concentration factor scales the strength of the interface perturbation with respect to the ratio of colour mixing at an interfacial

site. The maximum perturbation is induced when $pR = pB$ at a 50 : 50 red:blue mixed site and the minimum perturbation is induced when $pR \quad pB$ and $pB > 0$ or $Pb \quad Pr$ and $pR > 0$. Therefore our new perturbation scheme reduces interfacial effects in the bulk pure fluid components and narrows the interface width.

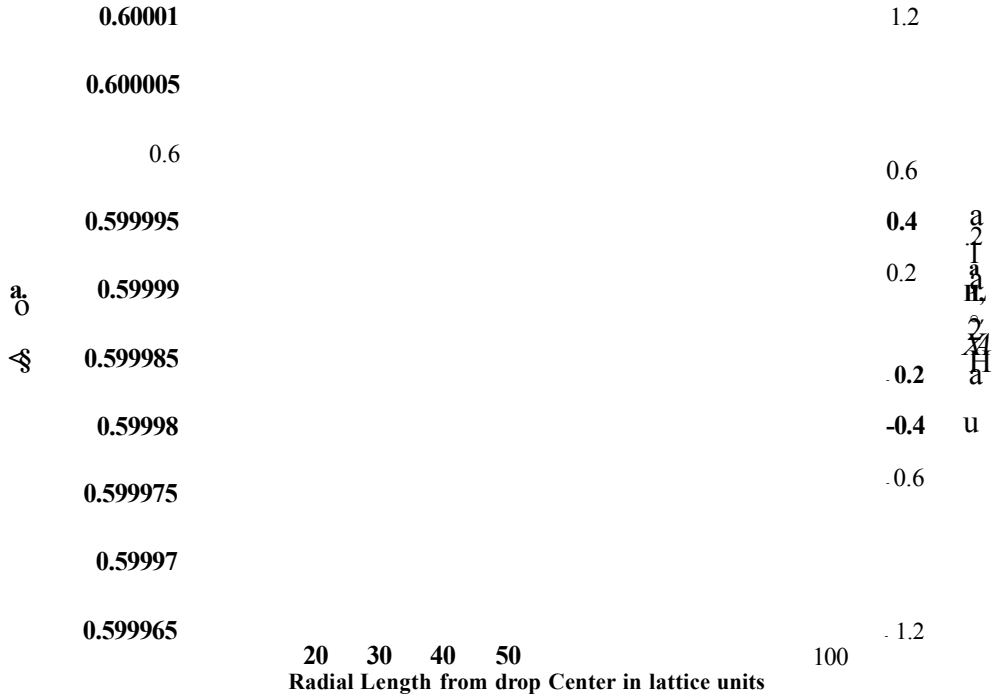

Figure 4.1: Radial pressure (green points denoted P) and colour transition (blue line denoted C) examination of the Gunstensen drop interface.

A study of the effect of the concentration factor on the interface width may be easily performed through an examination of the static pressure radial variation from the centre of a steady state fluid drop. Examination of the pressure change from the drop centre across the interface and into the supporting fluid is shown in Figure 4.1. This data was collected on a 150 x 150 lattice with a drop of initial radius R — 40 centrally located on the lattice and with drop simulation parameters a — 0.0075 and u = 1.5. The static pressure (green points) are calculated at each site directly

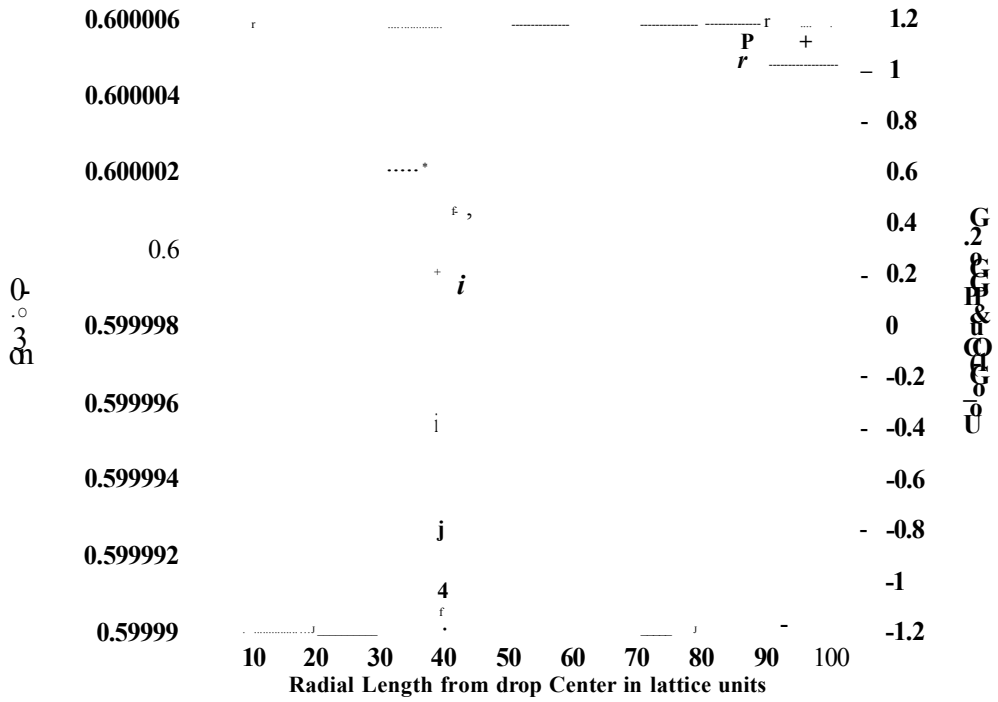

Figure 4.2: Radial pressure (green points) and colour transition (blue line) examination across the modified interface, which includes the colour concentration factor C(x,i).

from the local site density where $p = \rho/3$. A pressure jump is observed as we cross the drop interface and leave the higher pressure drop and enter the lower pressure surrounding fluid, as predicted by Laplace law. Accompanying the pressure jump is a pressure instability region centrally located around a *step function* colour transition (the colour interface) between the two fluid components (blue line), where the step function has the value 1 in the drop and -1 in the supporting fluid.

The interface perturbation of Gunstensen is seen to produce a pressure instability which extends approximately 15 lattice units into the pure red fluid drop (see Figure 4.1) before the pressure settles to an equilibrium value. The width of the pressure instability region may be measured by introducing an instability factor

$$H_T = \frac{R}{|\underline{r}|_{stable}} \tag{4.3}$$

where $|\underline{r}|_{stable}$ is the maximum radial distance from the drop centre where the drop pressure remains constant, therefore for the Gunstensen interface $H_T \approx 1.6$.

Inclusion of the concentration factor $C(\mathbf{x}, t)$ in our enhanced interface perturbation is seen to reduce the width of this pressure instability to approximately 5 lattice units into the fluid drop. A substantial reduction in the instability within the supporting fluid see Figure 4.2 is also seen, reducing $H_T \approx 1.14$. This value is considerably closer to the ideal and unrealisable value of $H_T = 1$ (indicating no pressure instability). The physical width (in lattice units) of the pressure instability region is of particular importance when considering applications of the model to real physical systems such as drop coalescence and breakup. A reduction in the instability will result in closer adherence to continuum hydrodynamics.

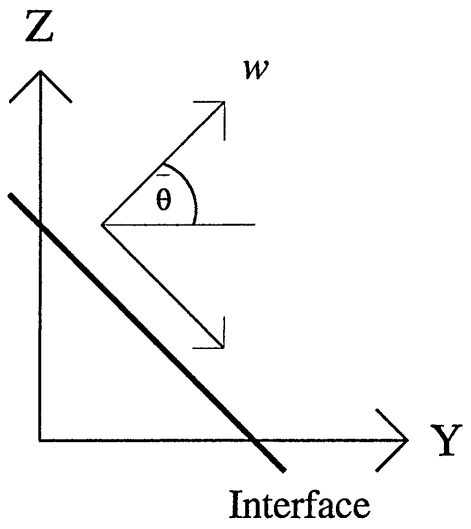

Figure 4.3: Co-ordinate system used in the region of a planar interface.

4.3 Analysis of the model

Throughout this analysis it is assumed that the interface is sufficiently flat for the mechanical definition of surface tension Σ [30], to be given by

$$\Sigma = \int_{-\infty}^{\infty} (P_N(w) - P_T(w))dw \tag{4.4}$$

where w measures the distance perpendicular to the plane of the interface see Figure 4.3 *i.e.* assuming that $P_N(w) \to P_T(w)$ quickly, as w increases. We make the assumption, that the principal modification that is required to account for interfacial curvature, is the inclusion of the microcurrent. The structure of the *steady-state* interface is considered and therefore the omission of time t from all variables throughout the analysis is made.

Consider a *steady-state* planar interface parallel with a lattice link direction $\mathbf{c}_i$. The interface has sufficient transitional symmetry (parallel to the interface) to produce

a constant colour gradient $\mathbf{f}(\mathbf{x},t)$ between adjacent interfacial sites. The calculation of $\mathbf{f}(\mathbf{x},t)$ provides the interfacial normal and the direction of the integration in Eq. (4.4). This direction is denoted by constant angle $\bar{\theta}$ subtended at the horizontal y-axis see Figure 4.3. These assumptions are justified by such a situation being readily realisable in appropriately initialised LB simulations. It is noted that interfacial *fluctuations* are present in immiscible lattice gas (ILG) interfaces [27]. However, calculations founded on similar assumptions performed using the Boltzmann approximation [7] to the ILG, may be employed to calculate surface tension from a prediction of the structure of the ensemble-average interface at steady-state [27].

The local lattice fluid pressure tensor $P_{\alpha\beta}(\mathbf{x},t)$, is approximated by

$$P_{\alpha\beta}(\mathbf{x},t) = \sum_i N_i(\mathbf{x},t) c_{i\alpha} c_{i\beta} \tag{4.5}$$

Pressure tensor contractions, analogous to those in Eq. (4.4), are obtained using Eq. (4.5) as

$$P_N(\mathbf{x}) = \sum_i N_i c_{iN}^2 \tag{4.6}$$

$$P_T(\mathbf{x}) = \sum_i N_i c_{iT}^2 \tag{4.7}$$

where c_{iT} (c_{iN}) denotes the component of $\mathbf{c}_i$ tangential (normal) to the interface

$$c_{iN}(\mathbf{x}) = |\mathbf{c}_i| cos(\theta_i - \bar{\theta}) \qquad c_{iT}(\mathbf{x}) = |\mathbf{c}_i| sin(\theta_i - \bar{\theta}) \tag{4.8}$$

Following reference [1] Eq. (4.4) is considered as an average over M_0 adjacent long integration lines, then cast as a discrete summation over lattice nodes in the *area* A of the interface

$$\Sigma = \int_{w=-\infty}^{\infty} (P_N(w) - P_T(w)) dw \rightarrow \frac{cos(\bar{\theta})}{M_0} \sum_{\mathbf{x}\in A} \sum_i N_i(\mathbf{x}) U_i(\mathbf{x}) \tag{4.9}$$

in which the summation on lattice site $\mathbf{x}$ is over all $\mathbf{x} \in A$ and we have introduced following Eq. (4.8), and the notation of reference [1]

$$U_i(\mathbf{x}) \equiv (c_{iN}^2 - c_{iT}^2) = c_i^2 cos(2(\theta_i - \bar{\theta})) \tag{4.10}$$

Note that whilst the factor $cos(\bar{\theta})/M_0$ in Eq. (4.9) is independent of $\bar{\theta}$ (Section 4.5), it is retained for the sake of compatibility with [1]. $N_i(\mathbf{x})$ separates, for D2Q9, into *equilibrium* and *non-equilibrium* components [23]

$$N_i^{neq}(\mathbf{x}) \equiv N_i(\mathbf{x}) - N_i^{eq}(\mathbf{x}) \tag{4.11}$$

$$N_i^{eq}(\mathbf{u}) = t_i \left(1 + 3u_\alpha c_{i\alpha} - \frac{3}{2}u_\alpha u_\alpha + \frac{9}{2}u_\alpha u_\beta c_{i\alpha} c_{i\beta}\right) \tag{4.12}$$

$$\begin{aligned} t_i = &\quad (1/36)\rho \quad i = 1,3,5,7 \\ t_i = &\quad (1/9)\rho \quad i = 2,4,6,8 \\ t_i = &\quad (4/9)\rho \quad i = 9 \end{aligned} \tag{4.13}$$

We note that the $\mathbf{x}$ dependence of $N_i^{eq}(\mathbf{u})$ arises only through the $\mathbf{x}$ dependence of the velocity field, whilst N_i^{neq} depends on $\mathbf{x}$ through both the velocity and its gradients. Using Eq. (4.11), we may write Eq. (4.9) as

$$\Sigma = \frac{cos(\bar{\theta})}{M_0} \sum_{\mathbf{x}} \sum_i N_i^{eq}(\mathbf{u}) U_i(\mathbf{x}) + \frac{cos(\bar{\theta})}{M_0} \sum_{\mathbf{x}} \sum_i N_i^{neq}(\mathbf{x}) U_i(\mathbf{x}) \tag{4.14}$$

these two contributions we proceed to treat separately, using Eqs. (4.10, 4.12, 4.13). Considering firstly the summation of the expanded *equilibrium* component

$$\begin{aligned} \sum_{\mathbf{x}} \sum_i N_i^{eq}(\mathbf{u}) U_i(\mathbf{x}) \;=\; & \left[1 - \frac{3}{2}u_\alpha u_\alpha\right] \sum_{\mathbf{x}} \sum_i t_i U_i(\mathbf{x}) \\ & + 3u_\alpha \sum_{\mathbf{x}} \sum_i t_i U_i(\mathbf{x}) c_{i\alpha} + \frac{9}{2}u_\alpha u_\beta \sum_{\mathbf{x}} \sum_i t_i U_i(\mathbf{x}) c_{i\alpha} c_{i\beta} \end{aligned} \tag{4.15}$$

The summation may be further simplified by considering links with odd and even link index i separately in the form

$$\sum_{\mathbf{x}}\sum_{i} t_i U_i(\mathbf{x}) c_{i\alpha} = \sum_{\mathbf{x}} \frac{\rho}{36} \sum_{i=odd} U_i(\mathbf{x}) c_{i\alpha} + \sum_{\mathbf{x}} \frac{\rho}{9} \sum_{i=even} U_i(\mathbf{x}) c_{i\alpha} \tag{4.16}$$

For any colour–field direction

$$\sum_{\mathbf{x}}\sum_{i} t_i U_i(\mathbf{x}) = 0 \tag{4.17}$$

therefore we may eliminate the first term in Eq. (4.15) and using the components of $\mathbf{c}_i$ in Appendix A Figure A.1 it may be easily proved that

$$\sum_{\mathbf{x}}\sum_{i} t_i U_i(\mathbf{x}) c_{i\alpha} = 0 \tag{4.18}$$

Thus only consideration of the contribution from the third term on the *rhs* of Eq. (4.15) is required in order to close the expression for the *equilibrium* term. Proceeding in an analagous manner resolves terms of the form

$$\sum_{\mathbf{x}}\sum_{i} t_i U_i(\mathbf{x}) c_{ix} c_{ix} = \frac{2}{9}\rho cos(2\bar{\theta}) \tag{4.19}$$

$$\sum_{\mathbf{x}}\sum_{i} t_i U_i(\mathbf{x}) c_{iy} c_{iy} = -\frac{2}{9}\rho cos(2\bar{\theta}) \tag{4.20}$$

$$\sum_{\mathbf{x}}\sum_{i} t_i U_i(\mathbf{x}) c_{ix} c_{iy} = \sum_{\mathbf{x}}\sum_{i} t_i U_i(\mathbf{x}) c_{iy} c_{ix} = \frac{2}{9}\rho sin(2\bar{\theta}) \tag{4.21}$$

Combining terms

$$\sum_{\mathbf{x}}\sum_{i} N_i^{eq}(\mathbf{u}) U_i(\mathbf{x}) = \left(u_x^2 - u_y^2\right) \rho cos(2\bar{\theta}) + u_x u_y 2\rho sin(2\bar{\theta}) \tag{4.22}$$

and introducing $\theta_u(\mathbf{x})$ such that

$$u_x = u cos(\theta_u(\mathbf{x})) \qquad u_y = u sin(\theta_u(\mathbf{x})) \tag{4.23}$$

the summation simplifies to

$$\sum_{\mathbf{x}}\sum_{i} N_i^{eq}(\mathbf{u})U_i(\mathbf{x}) = \sum_{\mathbf{x}} \rho u^2 cos(2(\theta_u(\mathbf{x}) - \bar{\theta})) \tag{4.24}$$

To deal with the second (*non-equilibrium*) term on the right hand side of Eq. (4.14) we follow Gunstensen *et al.* and appeal to the lattice Boltzmann equation for the BGK algorithm, appropriately modified to account for the presence of interfacial achromatic density perturbations and adapted to the steady state [1]

$$N_i(\mathbf{x} + \mathbf{c}_i) = N_i(\mathbf{x}) - \omega N_i^{neq}(\mathbf{x}) + \Delta N_i(\mathbf{x}) \tag{4.25}$$

Noting, for a closed lattice employing suitable boundary conditions $\sum_{\mathbf{x}} N_i(\mathbf{x}+\mathbf{c}_i) = \sum_{\mathbf{x}} N_i(\mathbf{x})$, and using our interfacial perturbation $\Delta N_i(\mathbf{x},t) = \sigma C(\mathbf{x},t) cos(2(\theta_f(\mathbf{x}) - \theta_i))$ after some algebra we may write the non-equilibrium term as

$$\begin{aligned} \sum_{\mathbf{x}}\sum_{i} N_i^{neq}(\mathbf{x})U_i(\mathbf{x}) &= \frac{\sigma}{\omega}\sum_{\mathbf{x}} C(\mathbf{x}) \sum_{i} cos(2(\theta_i - \bar{\theta}))U_i(\mathbf{x}) \\ &= \frac{\sigma}{\omega}(6 - 2cos(4\bar{\theta})) \sum_{\mathbf{x}} C(\mathbf{x}) \end{aligned} \tag{4.26}$$

which we note has the expected four-fold rotational symmetry. All of our calculations were checked using the computer algebra package *Mathematica.* Combining Eqs. (4.24, 4.26) into Eq. (4.14) yields an expression for macroscopic surface tension

$$\Sigma(\sigma,\omega) = \frac{cos(\bar{\theta})}{M_0} \sum_{\mathbf{x}} \rho \mathbf{u}^2 cos(2(\theta_u(\mathbf{x}) - \bar{\theta})) + \frac{\sigma cos(\bar{\theta})}{M_0 \omega}(6 - 2cos(4\bar{\theta})) \sum_{\mathbf{x}} C(\mathbf{x}) \tag{4.27}$$

Reminding the reader that $cos(\bar{\theta})/M_0$ term is independent of $\bar{\theta}$ we remark that Eq. (4.27) for $\Sigma(\sigma,\omega)$ is correct to all orders of fluid velocity. The second term on the *rhs* is straightforward to evaluate if we remember that $C(\mathbf{x}) = 0$ at pure, non-interfacial sites. No simplification, is however evident in the first term of Eq. (4.27)

and the positional summation must be evaluated over all interfacial sites where $\mathbf{x} \in A$. This leading order term in $\mathbf{u}$ makes only a small contribution to $\Sigma(\sigma, \omega)$ at practical values of σ (see Section 4.7). In this regime $\Sigma(\sigma, \omega) \sim \sigma/\omega$ where the relaxation parameter ω determines the lattice fluid kinematic viscosity ν through Eq. (4.28).

$$\nu = \frac{1}{6}\left[\frac{2}{\omega} - 1\right] \tag{4.28}$$

To the same order of approximation, Gunstensen *et al.* reported analogous dependence of their Σ upon the their LBILG collision parameter λ^{-1} , where λ is the eigenvalue of the LBILG collision matrix which determines the simulated fluid kinematic viscosity.

4.4 Surface tension in plane interfaces

Throughout the following analysis, we consider the microcurrent to be an interfacial effect resulting in mass flux across a line parallel to a static interface. We do not consider further microcurrents[1] defined in alternative terms, which produce no mass flux on mesoscopic length scales and have no physical influence on surface tension.

[1]We note there are two other possible definitions of microcurrents. Firstly the velocity at a site may be non-zero, but the flux along any link is zero. Secondly the flux along links may be non-zero, but the mass flux across a line parallel to the interface at the mesoscopic level is zero. Both these *other* microcurrents may be measured, but have no physical influence on surface tension, however they do occur at the flat interface.

4.4.1 Plane interface parallel to z-axis

Consider a steady-state planar interface parallel to the short lattice links along the z-axis direction in which colour is symmetrically separated (Figure 4.4), thus $cos(\bar{\theta}) = 1$. Translational symmetry along the z-axis implies an absence of any microcurrent and a colour gradient $\hat{\mathbf{f}}(\mathbf{x}) = f(y)\hat{\mathbf{y}}$. The stability of the LB method in principle produces a steady state interface which is free from fluctuations in the colour field. The direction of the colour field was measured from simulation and showed no measurable departure from this assumption.

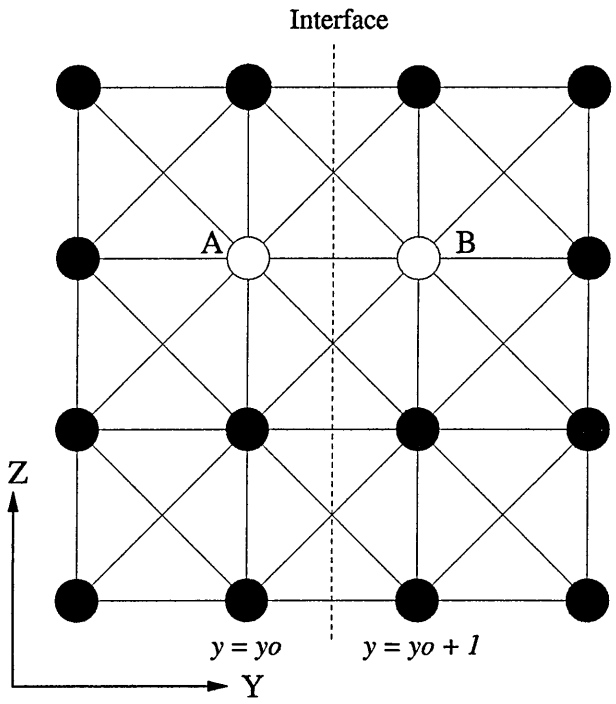

Figure 4.4: Symmetry of populations in a vertical interface. This figure shows a lattice excerpt containing several mixed nodes of which two have been highlighted (open circles) in an interface centred on the dashed line. Nodes to the left are predominantly red ($\rho_R \gg \rho_B$) whilst, in the stable interface, those to the right are predominantly blue ($\rho_B \gg \rho_R$). Note that colour populations in nodes A and B are equivalent under colour reversal and rotation through 180^0.

Consider a stable two site thick interface parallel to the z–axis and located centrally

between two adjacent sites, say $y = y_0$, $y = y_0 + 1$, and a colour distribution symmetrical under colour reversal, corresponding to a concentration given by

$$C(\mathbf{x}) = C(\delta(y - y_0) + \delta(y - y_0 - 1)) \tag{4.29}$$

where $C(\mathbf{x})$ is a colour concentration constant see Figure 4.4. If there are no microcurrents, $\mathbf{u} = 0$ everywhere and the expression for the surface tension reduces to

$$\Sigma(\sigma, \omega) = \frac{4\sigma C(\mathbf{x})}{M_0 \omega} \sum_{z=1..M_0, \forall y} (\delta(y - y_0) + \delta(y - y_0 - 1)) = \frac{8\sigma C(\mathbf{x})}{\omega} \tag{4.30}$$

At steady–state, the colour content of each node is constant between successive steps, and links connecting two mixed sites should contain at each end, counter–propagating equal densities of each colour. It is further assumed that achromatic link densities depart only negligibly from their *rest* equilibrium values t_i, allowing the value of the $C(\mathbf{x})$ in Eq. (4.29) to be calculated.

Each interfacial site (open circles) connects to three other mixed nodes and three monochromatic sites (filled circles) in the y direction and with two equivalent sites in the z direction (Figure 4.4). Making the assumption that sites are pure red for $y < y_0$ and pure blue for $y > y_0 + 1$. For diagonal, "speed 2", links $i = 3, 5$ in $y = y_0$ interacting with links $i = 7, 1$ in $y = y_0 + 1$

$$R_3(y_0, z) = B_3(y_0, z) = R_5(y_0, z) = B_5(y_0, z) = \frac{1}{2} t_1 = \frac{1}{72} \rho_0$$

$$R_1(y_0 + 1, z) = B_1(y_0 + 1, z) = R_7(y_0 + 1, z) = B_7(y_0 + 1, z) = \frac{1}{2} t_1 = \frac{1}{72} \rho_0$$

and similarly for speed 1 link $i = 4$ in $y = y_0$ interacting with link $i = 8$ in $y = y_0 + 1$

$$R_4(y_0, z) = B_4(y_0, z) = \frac{1}{2} t_2 = \frac{1}{18} \rho_0$$

$$R_8(y_0+1,z) = B_8(y_0+1,z) = \frac{1}{18}\rho_0$$

where ρ_0 is the achromatic density of the interfacial lattice site and we have used identities Eq. (4.13). Using this information the colour density of the nodes in $y = y_0$ may be calculated

$$\begin{aligned}
\rho_B(y_0,z) &= B_3(y_0,z) + B_4(y_0,z) + B_5(y_0,z) \\
&= \left(\frac{1}{72} + \frac{1}{18} + \frac{1}{72}\right)\rho_0 = \frac{1}{12}\rho_0 \\
\rho_R(y_0,z) &= \rho_0 - \frac{1}{12}\rho_0 = \frac{11}{12}\rho_0
\end{aligned}$$

from Eq. (4.31), $C(\mathbf{x}) = \frac{1}{6}$.

$$C(\mathbf{x}) = 1 - \left|\frac{\rho_R(\mathbf{x}) - \rho_B(\mathbf{x})}{\rho_R(\mathbf{x}) + \rho_B(\mathbf{x})}\right| \tag{4.31}$$

The value of $C(\mathbf{x}) = \frac{1}{6}$, on insertion into Eq. (4.30), gives, a macroscopic surface tension Σ for a horizontal interface parallel to the short D2Q9 lattice link of

$$\Sigma(\sigma,\omega) = \frac{4\sigma}{3\omega} \tag{4.32}$$

4.4.2 Plane diagonal interface

For a steady–state two site thick *diagonal* plane interface separated in a line parallel to the longer lattice links Figure 4.5, two different (but simply related) cross–interface density profiles occur. The macroscopic surface tension can be calculated with a small modification which arises as a result of the loss of full translational symmetry along the interfacial line. In the simplest case of an interface constituted by mixed sites A, B (open circles) in adjacent sections aa', bb' (Figure 4.5

defined by the lightly dotted sections) densities at A, $\{R_i(A), B_i(A)\}$, and those at B, $\{R_i(B), B_i(B)\}$, are equivalent under combined colour reversal and a 2-fold rotation.

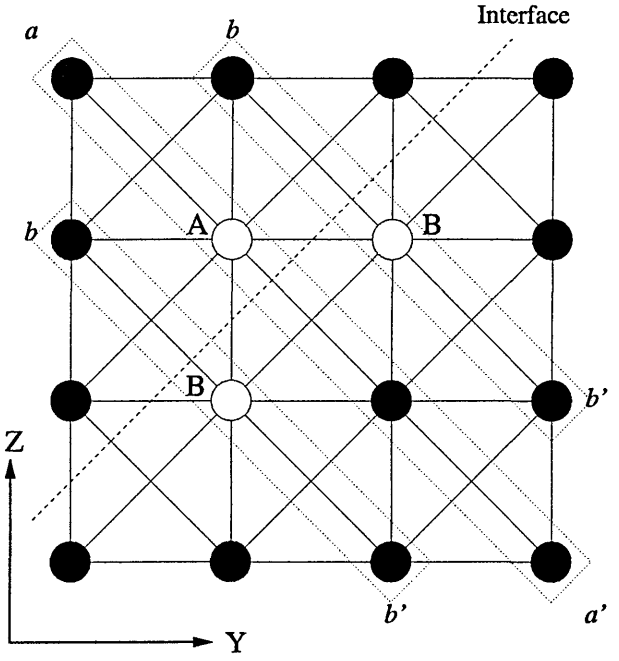

Figure 4.5: Populations in a diagonal interface. This figure shows a lattice excerpt containing several mixed nodes of which three have been highlighted (open circles) in the interface centred on the dashed line. Nodes above the dashed line are predominantly red ($\rho_R \gg \rho_B$) whilst, in the stable interface, those below are predominantly blue ($\rho_B \gg \rho_R$). Populations in nodes A and B are again equivalent under colour reversal and rotation through 180^0.

If the achromatic densities are again assumed to depart negligibly from their rest equilibrium values t_i, the simplest distribution of colour through the interface may be deduced. For links in the only (mainly red) mixed node in section aa', connecting to the mixed mainly blue node in two bb' sections, post-collision densities are

$$R_4(A) = B_4(A) = R_6(A) = B_6(A) = \frac{1}{2}t_2 = \frac{1}{18}\rho_0 \tag{4.33}$$

whilst, for link $i = 5$ in section aa' connecting to a pure blue node

$$R_5(A) = 0 \qquad B_5(A) = t_1 = \frac{1}{36}\rho_0 \tag{4.34}$$

where we have again used identities Eq. (4.13). Densities for the mixed B node are easily obtained from the symmetry arguments already rehearsed. The colour density of the mixed nodes in the diagonal interface is therefore

$$\rho_B(A) = B_5(A) + B_4(A) + B_6(A) = \left(\frac{1}{36} + \frac{1}{18} + \frac{1}{18}\right)\rho_0 = \frac{5}{36}\rho_0 \tag{4.35}$$

$$\rho_R(A) = \rho_0 - \frac{5}{36}\rho_0 = \frac{31}{36}\rho_0 \tag{4.36}$$

from Eq. (4.31) $C(\mathbf{x}) = \frac{5}{18}$ for both the A and B mixed sites. Setting $\bar{\theta} = 45^0$, and noting that there is an A *and a* B mixed site on any horizontal line crossing a diagonal interface, it follows from Eq. (4.27) that the macroscopic surface tension is

$$\Sigma(\sigma, \omega) = \frac{40\sigma}{9\sqrt{2}\omega} \tag{4.37}$$

4.4.3 Single site interface

A simple single site plane interface which intersects a lattice node parallel to lattice link directions may take two basic configurations. In the first the interface is parallel to the z–axis and in the second the interface is parallel with a diagonal link see Figure 4.6. Considering firstly a simple plane interface parallel to the z–axis. Nodes to the left of the dashed line are considered to be predominantly red ($\rho_R \gg \rho_B$) whilst, in the stable interface, those to the right are predominantly blue ($\rho_B \gg \rho_R$) along with the links parallel to the interface and the rest link. Considering the total

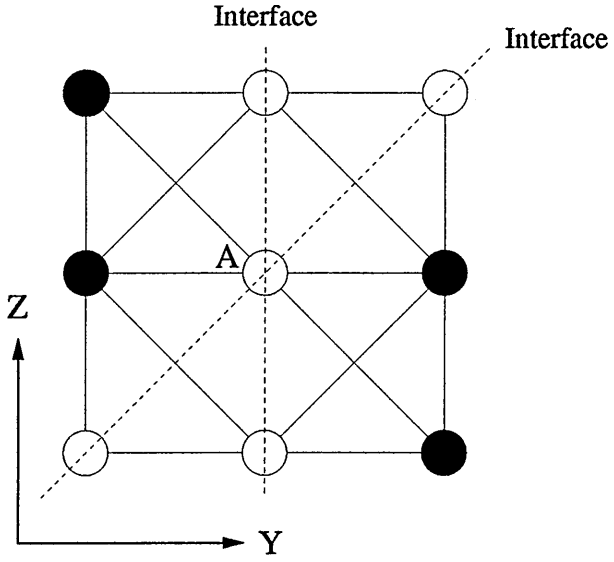

Figure 4.6: Populations in a single site interface. This figure shows a lattice excerpt of a single site interface (open circles), the interface (dashed line) is parallel but not centred on the link directions. In each case links parallel to the interface and stationary links are considered to contain blue density.

red density at node A for this geometry

$$\rho_R(A) = R_7(A) + R_8(A) + R_1(A) = \left(\frac{1}{36} + \frac{1}{9} + \frac{1}{36}\right)\rho_0 = \frac{1}{6}\rho_0 \tag{4.38}$$

$$\rho_B(A) = \rho_0 - \frac{1}{6}\rho_0 = \frac{5}{6}\rho_0 \tag{4.39}$$

from Eq. (4.31), $C(\mathbf{x}) = \frac{1}{3}$ giving a macroscopic surface tension

$$\Sigma(\sigma, \omega) = \frac{4\sigma}{3\omega} \tag{4.40}$$

Following similar analysis once more for an interface diagonally intersecting a lattice node, by considering sites above the interface to be coloured predominantly red and below the interface to be blue. The colour concentration $C(\mathbf{x}) = \frac{1}{2}$ may be calculated, this assumes of course that links parallel to the interface are again coloured blue, and we note that $\bar{\theta} = 45^0$. The macroscopic surface tension of the interface

may then be calculated as

$$\Sigma(\sigma,\omega) = \frac{4\sigma}{\sqrt{2}\omega} \tag{4.41}$$

The preceding analysis of flat interfaces between static fluids neglects perturbation–induced departures from equilibrium rest density, the validity of which assumption increases with decreasing perturbation amplitude σ, and is supported from the results of the next section. It should be noted that this assumption implicitly restricts the principal analytical results of this section (Eqs. (4.32, 4.37, 4.40, 4.41)) to apply when the induced macroscopic surface tension is small. Note also that due to the absence of local curvature in the interface no density (pressure) change between the bulk fluids separated by the interface is to be expected. We now consider the effect of microcurrents which are precluded by symmetry in planar interfaces.

4.5 Surface tension in Curved Interfaces

Microcurrents are induced close to an interface, by the segregating effect of the surface tension rule [29, 43]; only in the presence of suitable symmetry, such as the cases considered in Section 4.4, will the microcurrents be absent. The presence of interfacial curvature and a gradient in the colour field, make it impossible to argue on general grounds that an interfacial microcurrent should be absent from the rest interface. The influence of the microcurrent is felt principally through the first term in Eq. (4.27), the only term containing a velocity component. The magnitude of the microcurrent velocity close to the interface has been observed to scale with increased

σ [29, 43] and to be of the form

$$\mathbf{u} = \mathbf{u}(\mathbf{x})\sigma \tag{4.42}$$

For circular interfaces in two dimensional simulations of static steady–state red fluid drops, the interfacial microcurrent pattern must conform with the rotational symmetry of the underlying lattice and two complementary, counter-rotating microcurrent *cells* must occupy any lattice quadrant Figure 4.7, the maximum velocity in each occurring close to the generating interface Figure 4.9. In fact the maximum value of the surface tension inducing perturbation occurs for the maximum value of $U_i(\mathbf{x})$ in Eq. (4.10) at $\bar{\theta} = 45^0$, accounting for the fact that the microcurrent circulation close to the interface is radial along the diagonal bisectors of each quadrant (Figure 4.8). Moreover, on grounds of lattice symmetry and hydrodynamics which govern the microcurrent, the extent of a microcurrent cell is determined by lattice extremities and drop radius R. The microcurrent flow outside the interface is approximated by a uniform rotation such that the outermost streamline touches the interface and has a velocity determined principally by the interface perturbation parameter σ Eq. (4.42). We then write the microcurrent velocity field, $\mathbf{u}(\mathbf{x}) = \mathbf{u}(\hat{\mathbf{r}}, |\mathbf{r}|/R)$ in Eq. (4.27) and note that $\mathbf{u}(\hat{\mathbf{r}}, |\mathbf{r}|/R)$ must have the four fold rotational symmetry of the lattice. Hence Eq. (4.27) becomes

$$\begin{aligned}\Sigma \;=\; & \frac{\sigma^2 cos(\bar{\theta})}{M_0} \sum_{\mathbf{x}} \mathbf{u}\left(\hat{\mathbf{r}}, \frac{|\mathbf{r}|}{R}\right)^2 \rho cos(2(\theta_u(\mathbf{x}) - \bar{\theta})) \\ & + \frac{\sigma cos(\bar{\theta})}{M_0 \omega}(6 - 2cos(4\bar{\theta})) \sum_{\mathbf{x}} C(\mathbf{x})\end{aligned} \tag{4.43}$$

This result of course, applies only to the D2Q9 BGK model through the assumed form of the equilibrium distribution function defined in Eqs. (4.12, 4.13). The extent

Figure 4.7: Stream function for steady circulation pattern developed by drop of radius R = 13 lattice units placed centrally on a square 150 x 150 lattice. The flow pattern is observed to be stable after approximately 4000 time steps. The results were obtained for the same simulation parameters as Figure 4.12.

Figure 4.8: Magnification of the stream function in the right hand upper quadrant of the lattice.

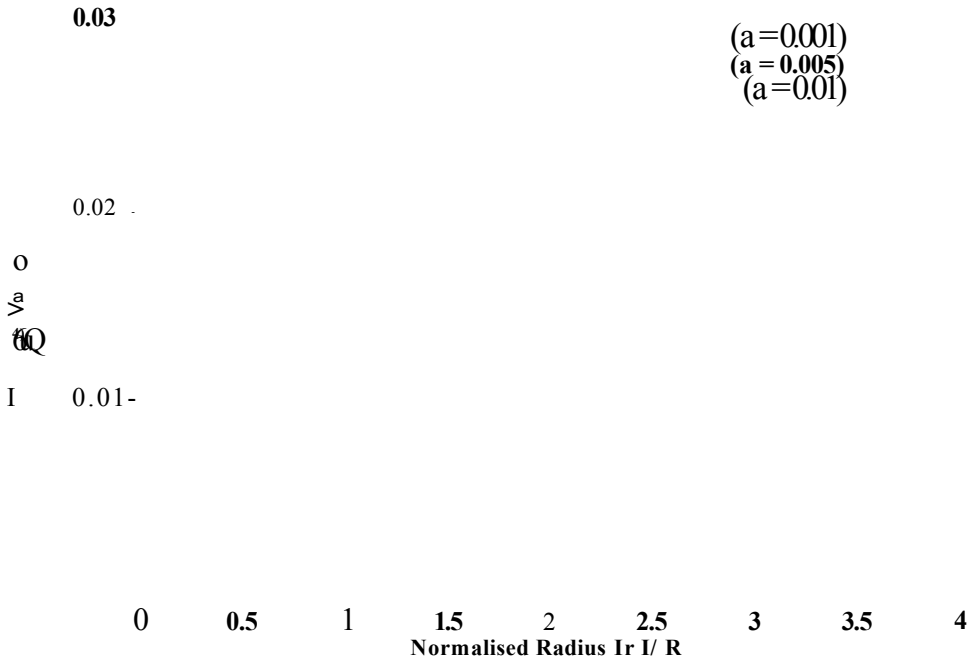

Figure 4.9: Variation of **|u|,** microcurrent flow speed measured in units of lattice spacing per time step, against normalised distance from the drop centre, $\backslash r \backslash / R$ for several values of parameter a (see key) and w = 1.5. Note the approximately linear trend in peak flow activity with σ, which occurs close to the interface (this trend is confirmed when compared microcurrent data with higher values of σ, these values are not shown as they are not practical values of σ).

of the anisotropy of the second term (Eq. (4.43)) and its influence on the surface tension may be determined only after the concentration factor $C(\mathbf{x})$ is calculated. To interpret Eq. (4.43) in the presence of curvature, we consider an interfacial element of length $R\Delta\theta$ from a large circular drop of radius R, subtending a small angle $\Delta\theta$ at the drop centre. This element we assume to be locally flat and contained within an area defined by M_0 long horizontal lattice lines where $z = \text{const}$. Then $M_0 = R\Delta\theta cos(\bar{\theta})$, implying $cos(\bar{\theta})/M_0 = 1/R\Delta\theta$. The magnitude of the positional summation in the second term of Eq. (4.43) is proportional to $R\Delta\theta$, and a form $\sigma k_2/\omega$ is assumed. Considering the first term, we take the microcurrent activity to decay rapidly away from the interface, this assumption is supported by simulation see Figure 4.9 and this will yield finite contributions to the first summation only from a number of sites proportional in number to the $R\Delta\theta$ and the velocity at all of these sites we take to be determined principally by σ from Eq. (4.42). The positional summation in the first term in Eq. (4.43) will therefore also be proportional to $R\Delta\theta$ and we assume a form $\sigma^2 k_1$ for this term. This allows us to predict the general form for the interfacial tension of a drop to be

$$\Sigma(\sigma,\omega) = \sigma^2 k_1 + \frac{\sigma}{\omega} k_2 \tag{4.44}$$

for small values of the interfacial perturbation parameter σ, the dominant contribution is obviously from the second term component

$$\Sigma(\sigma,\omega) \cong \frac{\sigma}{\omega} k_2 \tag{4.45}$$

4.6 Simulation

Plane symmetric two-site thick interfaces were simulated employing periodic boundary conditions (retained for all simulations) to all edge sites on a square lattice, effectively producing an interface of infinite length. A suitable simulation box size and equilibration time were determined on the basis of stability. For all simulations, sites were initialised to achromatic local density of $\rho_0 = 1.8$, resulting in rest equilibrium link densities of 0.8, 0.18 and 0.045 for speed 0, 1 and 2 links respectively, initial colour being allocated so as to produce a particular interface geometry.

Results were obtained for plane, y = constant, interfaces on a 120×120 lattice containing a red vertical layer sandwiched between two blue fluids of equal viscosity. The initial interface lying between consecutive y-planes of nodes and the red layer defined by $\rho_R(\mathbf{x}) = 1.8$, $\rho_B(\mathbf{x}) = 0$, $39 < y < 81$. The diagonal interface was constructed by initialising as red those nodes with y co-ordinates such that $z - 26 \leq y \leq z + 26$, *with the periodic images of this red layer incorporated in the lattice corners* Figure 4.10. An equilibration time of 15,000 iterations was allowed for both plane interface orientations and the steady-state density distribution was measured through the interfacial region. Also measured through the interface was the quantity $(P_N - P_T)$, using Eqs. (4.6, 4.7). These measurements in conjunction with a simple discrete approximation to the mechanical definition Eq. (4.4) allowed the planar interfacial tension to be evaluated.

Links within a circular, central portion of radius R defined from the centre of the

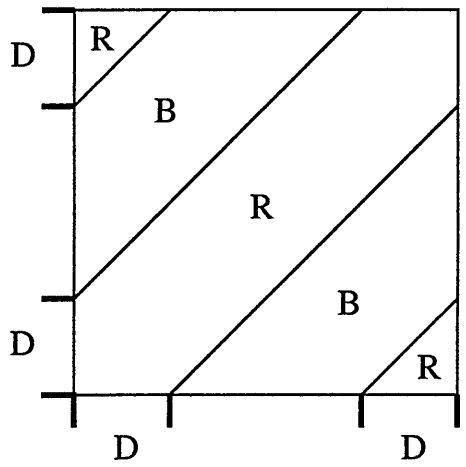

Figure 4.10: Initial distribution of colour for the simulation of a diagonal interface on the square D2Q9 lattice showing the periodic images of the red diagonal layer in the box corners. Regions marked R (B) correspond to red (blue) mass.

lattice of an otherwise blue 150×150 lattice, were initialised red to form a circular drop. Different combinations of surface tension perturbation parameter σ and BGK collision parameter ω were chosen to generate stable drops with the values of ω now being chosen so as best to recover classical hydrodynamic behaviour [44]. Laplace law measurements were made on these drops to obtain surface tensions $\Sigma(\sigma, \omega)$ from the gradient of pressure difference $\Delta p = \Delta\rho/3$ [23] as a function of $1/R$ for drops with a radius in the range $15 < R < 40$. The steady-state value of R was obtained from the drop inertia tensor [43].

In order to observe the influence of microcurrent activity from circular interfaces the stream function

$$\psi(y, z) = \int_{z'=0}^{z'=z} u_y(y, z')dz' \tag{4.46}$$

was calculated from the velocity field along with the corresponding pressure (lattice density) field. The variation with normalised distance from the drop centre $\bar{r} \equiv r/R$, of velocity modulus averaged over an annular lattice sample concentric with the drop

centre, radius $\bar{r}$, yields a quantitative measure of microcurrent activity and a test of the assumptions made in deriving Eq. (4.44).

4.7 Results

The measured values of surface tension were obtained directly from a trapezium rule approximation to Eq. (4.4)

$$\Sigma(\sigma,\omega) = \frac{|\mathbf{c}_i|}{2}\left[\sum_{\mathbf{l}}(P_N(\mathbf{l}) - P_T(\mathbf{l}) + P_N(\mathbf{l}+\mathbf{c}_i) - P_T(\mathbf{l}+\mathbf{c}_i))\right] \tag{4.47}$$

where $\mathbf{l}$ denotes the position on a lattice line perpendicular to the interface and we use Eqs. (4.6, 4.7) to obtain $P_N(\mathbf{l}), P_T(\mathbf{l})$. The table in Figure 4.11 shows the close agreement between calculated and measured interfacial quantities for both orientations of the two sites thick planar interface considered.

Interface Orientation	Calculated $\Sigma(\sigma,\omega)$	Measured $\Sigma(\sigma,\omega)$	Calculated $C(\mathbf{x})$	Measured $C(\mathbf{x})$
Horizontal	7.33×10^{-3}	7.37×10^{-3}	0.166	0.15
Diagonal	1.73×10^{-3}	1.73×10^{-3}	0.28	0.28

Figure 4.11: Calculated and measured values of mechanical surface tension for the two-site thick interface. Calculated values derived from Eqs. (4.32, 4.37). For the planar horizontal interface $(\sigma,\omega) = (5 \times 10^{-3}, 0.91)$, whilst for the planar diagonal interfaces simulated $(\sigma,\omega) = (5 \times 10^{-4}, 0.91)$.

Figure 4.12 shows on the same axes, normalised variation of colour and pressure tensor contraction $(P_N(\mathbf{l}) - P_T(\mathbf{l}))$ through the vertical interface described in Section 4.3 with S measured in lattice units. For the corresponding case of a diagonal interface (Figure 4.13 and Figure 4.14) colour is not, as expected, symmetrically dis-

Figure 4.12: Normalised variations across a vertical interface. The dotted (dashed) line connects calculated blue (red) densities and symbols mark corresponding measured values. The solid line corresponds to the value of *(PN —PT).*

tributed about the maximum value of *(PN {1) —FT(l))]* Figure 4.13 and Figure 4.14 represent sections of the interface along adjacent diagonals (Figure 4.5) which are inter-related by a rotation of *n* radians and a colour reversal. Parameter *S* is related to co-ordinate y through *S = y/2y.* For the results of Figure 4.12, Figure 4.13, Figure 4.14 the BGK collision parameter *u* — 0.91 was used in conjunction with surface tension perturbations *a* = 0.005 (Figure 4.12) and cr = 0.0005 (Figure 4.13 and Figure 4.14).

Figure 4.7 shows the microcurrent structure generated at the surface of a red fluid drop through the stream function *z)* calculated by a process of numerical integration after Eq. (4.46). The microcurrents are seen to be consistent with the

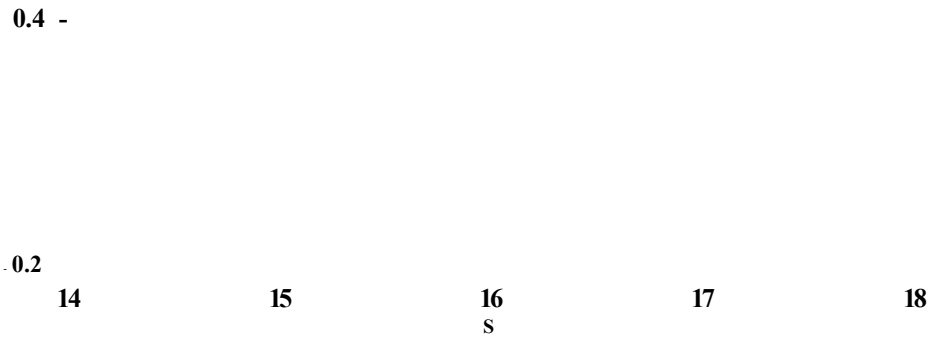

Figure 4.13: Normalised variations across a diagonal interface sampled along aa' (Figure 4.5), lines connect calculated points, whilst symbols show results obtained from simulation. The solid line corresponds to the value of $(P^{\wedge} - Pr)$.

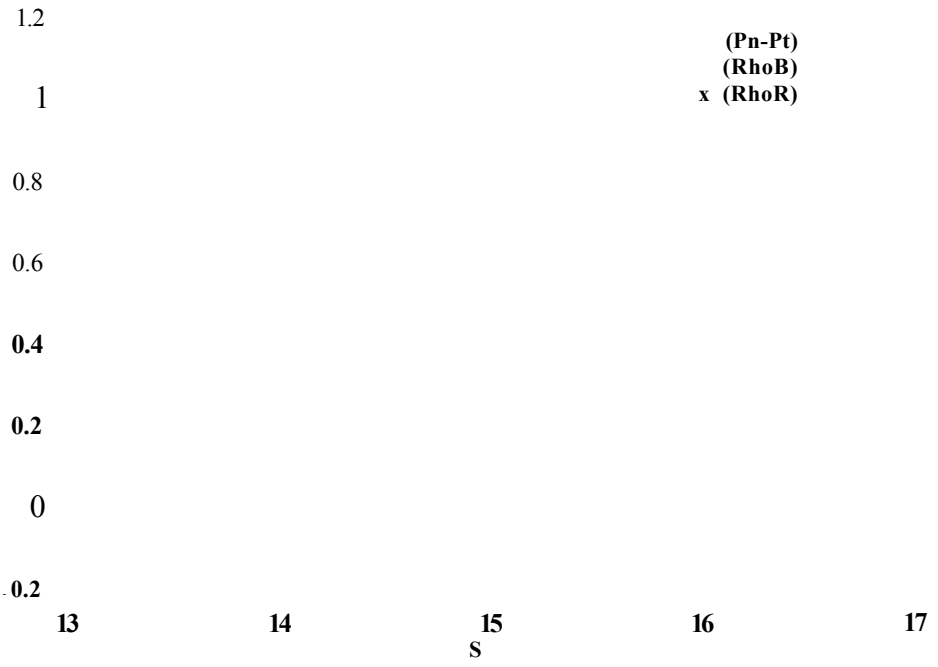

Figure 4.14: Normalised variations across a diagonal interface, sampled along bb' (Figure 4.5). The solid line corresponds to the value of $(P_M - P_T)$.

symmetry of the underlying lattice and the maximum perturbation.

The range of influence of the microcurrent for a periodically bounded drop on a 150 x 150 lattice is shown in Figure 4.9 which charts the variation of the flow speed $|\mathbf{u}|$, against normalised distance from the drop centre, $|r|/R$ for several values of ϖ. As a quantitative assessment we note that Eq. (4.44) predicts that a graph of $E(a,co)/cr$ against $1/co$ will have an ordinal intercept (gradient) from which constant $k|^{(2)}$ may be inferred. Accordingly (Figure 4.15) $E(g,uo)/(j$ was obtained from Laplace Law, (see Section 4.6) applied to drops with $0.5 < \varpi < 2.0$ and $a = 0.025$. With the latter value of perturbation parameter the number of data points necessary reliably to apply linear regression entails significant processing but yields values of $hi = 30.551 \pm 0.024$ and $\&2 = 1.259 \pm 0.031$. Hence, for $a = 0.025$, the microcurrent

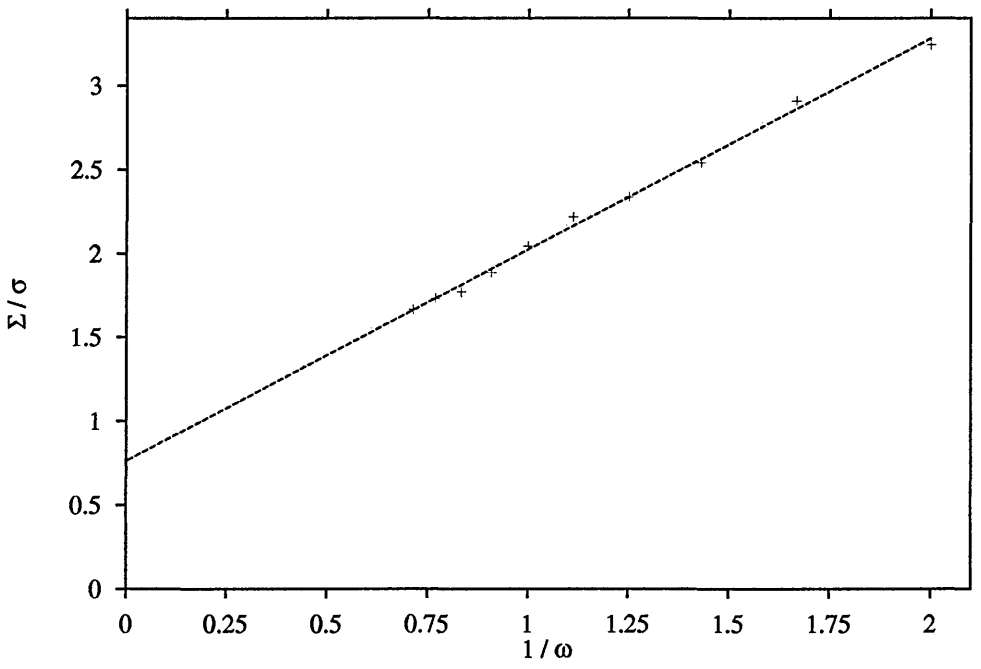

Figure 4.15: Plot of $\Sigma(\sigma,\omega)/\sigma$ (measured in lattice units) against (dimensionless) $1/\omega$ for $0.5 \leq \omega \leq 2.0$. The former were obtained from Laplace's Law applied to drops with $\sigma = 0.025$ and $15 \leq R \leq 40$ on a 150x150 lattice. The ordinal intercept and gradient, obtained from linear regression, were found to be $\sigma k_1 = 0.764 \pm 0.031$ and $k_2 = 1.259 \pm 0.024$ respectively.

contribution to the macroscopic surface tension in our model is seen to approximate to that arising from the second term in Eq. (4.44) and we infer an estimated upper limit for σ of $\sigma \approx 0.025$ to minimise the effect of the microcurrent. For the present model under study ($\omega = 1.5$), the influence of a microcurrent upon the macroscopic surface tension is of decreasing importance at perturbation parameter $\sigma \leq 0.025$.

Figure 4.16 is plotted from values in the range $0.001 \leq \sigma \leq 0.0125$, well below the upper σ limit and shows results for surface tension $\Sigma(\sigma,\omega)$ for $1.5 \leq \omega \leq 1.9$ against σ/ω. The surface tension results are derived from Laplace law measurements described earlier. The continuous line represents a linear regression fit to this data

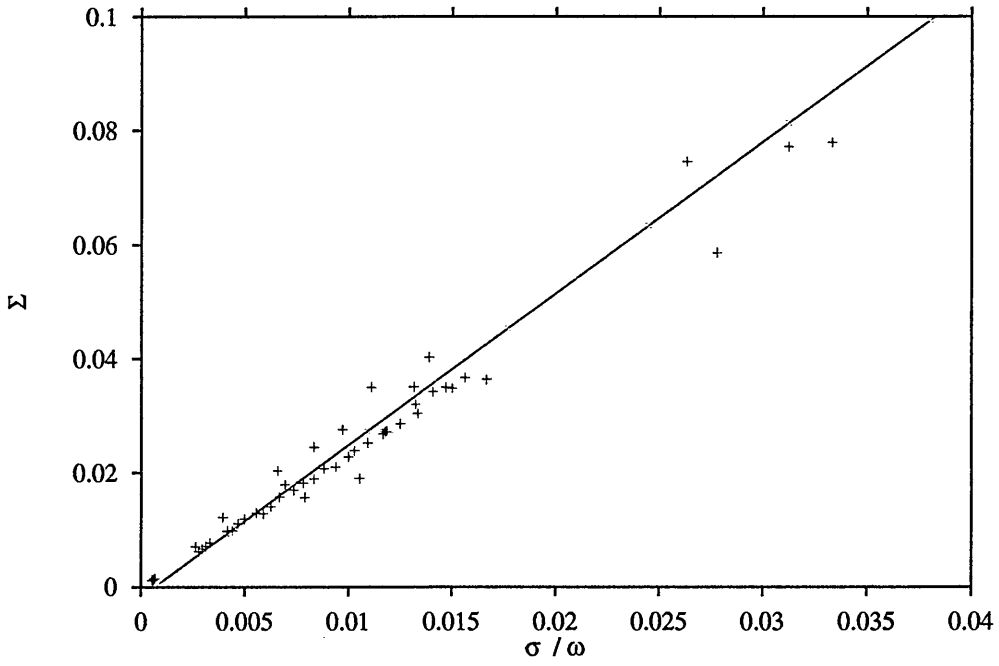

Figure 4.16: Simulational measurements of Laplace law surface tension $\Sigma(\sigma, \omega)$ (measured in lattice units) for $0.001 \leq \sigma \leq 0.0125$, $1.5 \leq \omega \leq 1.9$ as a function of quotient $\frac{\sigma}{\omega}$ (where σ and ω are dimensionless). The continuous line is a linear regression fit to the data.

and although *unconstrained* to pass though the origin, the fit generates an intercept which lies well within one standard deviation of zero and a gradient which may be used with a set σ to confirm k_2, Eq. (4.45).

Obtained from Eq. (4.27), Eq. (4.32) is valid for a flat horizontal interface at rest. Based as it is on the mechanical definition of surface tension [30], Eq. (4.27) we interpret only with respect to equilibrium (rest) fluids and the velocity dependence entailed in its first term, should be regarded as arising only from the microcurrent activity. Nevertheless a useful check on Eq. (4.27) may be performed by applying a uniform shear of increasing rate parallel to the flat vertical layer $-10 \leq y \leq 10$ on a 60×60 lattice (see discussion above and Figure 4.4), the shears being generated in the usual manner [43]. Setting $\bar{\theta} = 0$, $\theta_u(\mathbf{x}) = \pi/2$, for small σ we may omit the second term from Eq. (4.27) and

$$\Sigma(\sigma,\omega) \approx -\frac{\rho}{M_0}\sum_{\mathbf{x}}\mathbf{u}^2 = -\rho\sum_{y=-10}^{y=20}\mathbf{u}(y)^2 \tag{4.48}$$

Figure 4.17 shows the results of plotting $\Sigma(\sigma,\omega)$, obtained from Eq. (4.47), as ordinate against summation $S_0 \equiv \sum_{y=-10}^{y=20}\mathbf{u}(y)^2$, obtained for a small range of shear rates, as abscissa, with the expected linear trend emerging. At small shear rates the first term in Eq. (4.27) becomes positive and contributes to the magnitude of $\Sigma(\sigma,\omega)$. We do not claim Figure 4.17 represents more than a interesting property of Eq. (4.27) and Eq. (4.43) resting on definitions in which a static interface is implicit [30].

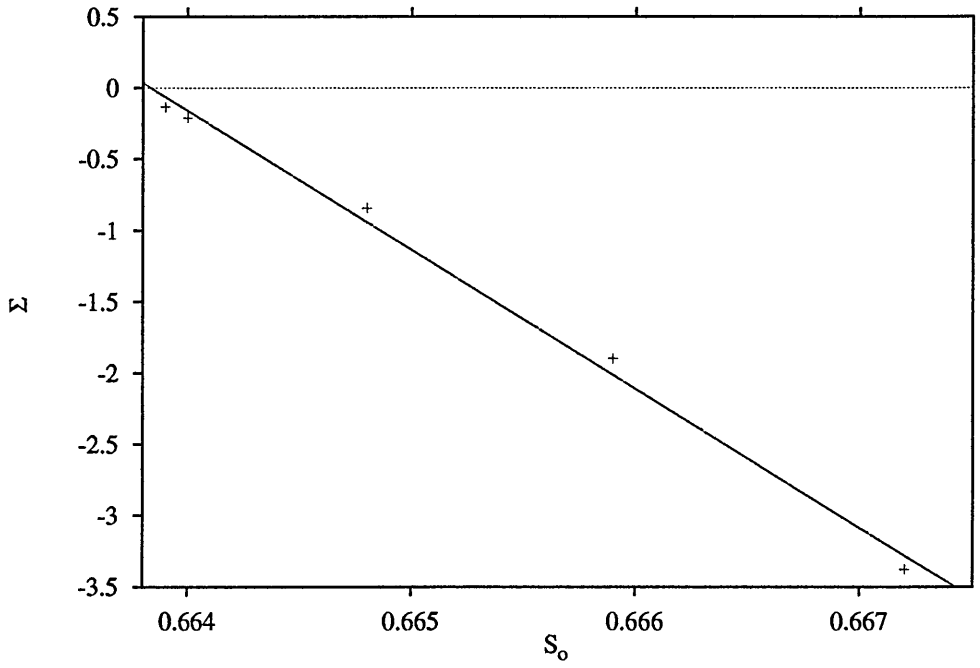

Figure 4.17: $\Sigma(\sigma, \omega)$ (measured in lattice units obtained from Eq. (4.47)) as ordinate against summation $S_0 \equiv \sum_{y=-10}^{y=20} \mathbf{u}(y)^2$ (dimensions of lattice units squared) for a vertical interface exposed to a uniform shears parallel to the vertical interface $-10 \leq y \leq 10$ placed on a 60×60 lattice.

4.8 Conclusions

In this chapter our two component fluid model based upon a D2Q9 lattice BGK scheme has been introduced and investigated. Simulation measurements of surface tension and cross–interfacial colour distributions for this model are in good agreement with those values calculated from analysis of the algorithm Figure 4.11, for both two site thick plane horizontal and diagonal, microcurrent-free interfacial orientations. The difference between the two expressions suggests an orientational dependent anisotropy in the model's surface tension, which is investigated in detail in the next chapter. The structure of interfacial microcurrent circulation generated by circular drops has been deduced and compared with simulation. These measurements demonstrate that developed theory successfully accounts for the broad structure of the microcurrent flow field. The analysis has allowed the development of an expression for the surface tension of a drop, demonstrating that the microcurrent velocity field might be expected directly to influence the model's surface tension. For small values of parameter σ the corrections are only found to be second order in σ and this is substantiated by simulation.

Any attempt quantitatively to assess the approximate theory of microcurrent contribution will require substantial quantities of data, and should be undertaken only after a more rigourous analysis of the contribution of the first term in Eq. (4.44). The undertaking would be facilitated by a calculation of the steady microcurrent flow field as an approximate or numerical solution of the equations of creeping flow, which should fully account for the microcurrent structure. Although our general

arguments yield a qualitative insight into the origin of the microcurrent, such a calculation would provide the most useful check on our understanding of this parasitic phenomenon.

Chapter 5

Hydrodynamic stress transmission

5.1 Introduction

The aim of this chapter is to examine more fully than previous researchers, the extent to which the tangential and normal boundary conditions are upheld in the immiscible LBGK interface. We then introduce modifications to the interface perturbation, which we will show improve the hydrodynamic behaviour of the interface.

Previously researchers have qualitatively examined interfacial behaviour only through static Laplace law calculations, or through the integration of the pressure tensor [1]. This has left the macroscopic hydrodynamics of the interface un-addressed until now. In continuum hydrodynamics the interface between two immiscible fluids is governed by the hydrodynamic boundary conditions for tangential stress transmission

$$\sigma'^{R}_{\alpha\beta} t_\beta - \sigma'^{B}_{\alpha\beta} t_\beta = 0 \tag{5.1}$$

and normal stress transmission

$$\sigma^R_{\alpha\beta} n_\beta - \sigma^B_{\alpha\beta} n_\beta = \Sigma \left(\frac{1}{R_1} + \frac{1}{R_2} \right) n_\alpha \tag{5.2}$$

where Σ is the macroscopic surface tension, $\sigma_{\alpha\beta}$ is the stress tensor and $\sigma'_{\alpha\beta}$ is the viscous stress tensor. The normal and tangent to the interface are given by $\hat{\mathbf{n}}$ and $\hat{\mathbf{t}}$ respectively, where R_1 and R_2 are the interface's two principle radii of curvature [14]. We note that the two dimensional static Laplace law $\Sigma = \frac{\Delta p}{R}$ which has been used as a benchmark surface tension test, is a simplified case of Eq. (5.2) and that the full tangential relation Eq. (5.1) has not yet been directly assessed for the LBGK interface.

In this chapter we firstly examine the tangential boundary condition in section 5.2 and having established that the interface exhibits appropriate hydrodynamic behaviour we proceed to assess the normal stress behaviour in section 5.3. To facilitate the latter it will be necessary to develop accurate means by which the local radius of curvature may be assessed. Results from these investigations motivate further algorithmic extensions designed to improve the hydrodynamics and isotropy of the immiscible interface. It is appropriate to point–out that the investigative methods employed to examine the interface in sections 5.2 and 5.3 are relevant to other interface generating techniques [32, 45].

5.2 Tangential stress examination

In this section the tangential stress condition Eq. (5.1) is assessed as it applies to our interface separating a blue–red–blue planar sandwich layer system see Figure 5.1. This system is sheared in a direction parallel to the coloured layers at the top and bottom of the lattice in the the y-direction. For this system hydrodynamic theory predicts a linear relation between shear stress and velocity gradient in the bulk fluids of

$$\frac{\partial u_y}{\partial z} = \dot{\gamma} \tag{5.3}$$

where ν is the fluid shear viscosity and $\dot{\gamma}$ is the fluid shear rate. For blue and red fluid layers with different viscosities Eq. (5.4) also holds

$$\dot{\gamma}_R \nu_R = \dot{\gamma}_B \nu_B \tag{5.4}$$

where the subscripts refer to the fluid colour. Finally of course, the velocities of the separated components should match at the interface.

The transmission of tangential stress by the interface was assessed through Eq. (5.4), by examining the measured ratio between the separated fluids' different shear rates and comparing this with their set viscosities. With periodic boundary conditions implemented on the vertical walls, horizontal shear was induced on the system of Figure 5.1 by adding a positive y–direction (negative y–direction) velocity component to the top (bottom) horizontal layer of lattice sites at each lattice update, using a link density *force increment* [43] (Note, that care should be exercised to apply this pertubative step directly before the lattice is propagated and that the caption of

Figure 5.1 gives more detail). This lattice–edge closure process produces a lattice fluid shear rate proportional in size to the forcing increment [43].

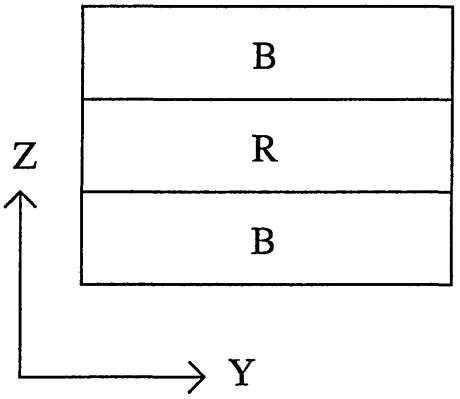

Figure 5.1: Schematic lattice configuration for tangential stress examination. Periodic conditions were used to close all lattice boundaries, with horizontal forcing applied along sites in the lines z = 2, 58

The red / blue layers were set to a different viscosity through the BGK relaxation parameter ω in the obvious manner, with the mixed sites occuring at the singular dividing interfaces controlled through an effective average relaxation parameter

$$\omega_{eff} = \frac{\omega_R \rho_R + \omega_B \rho_B}{\rho_R + \rho_B} \tag{5.5}$$

The system of Figure 5.1 was evolved on a 90×60 lattice, with a lower blue layer of height $1 \leq z \leq 20$ a red layer of height $21 \leq z \leq 40$ and an upper blue layer of $41 \leq z \leq 60$. Initialised with a range of viscosity ratios red : blue of 1.5 : 1, 2.5 : 1 and 3.5 : 1, the mean (y–averaged) shear was measured in each horizontal fluid layer (in lattice units) . With the two colours set to a different viscosity the *sandwich* of Figure 5.1 was sheared.

As we would expect a typical variation of the y–averaged velocity with distance z across the differing layers, shown in Figure 5.2 displays the expected trend and the

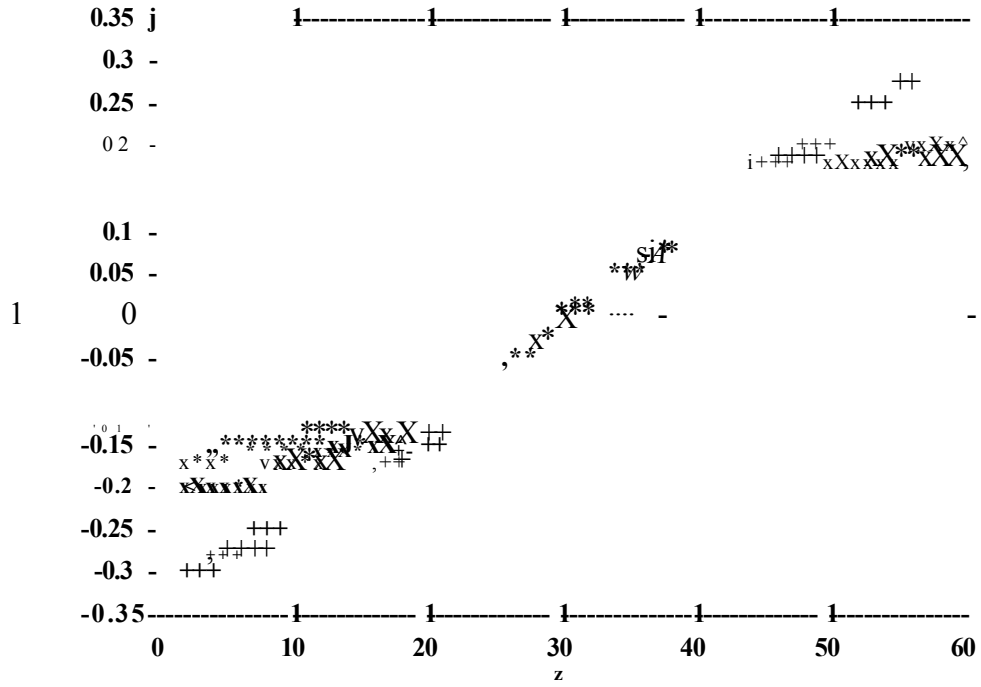

Figure 5.2: Variation in mean flow velocity |u| against z for viscosity ratios of 1.5 : 1, 2.5 : 1 and 3.5 : 1

(fully) tangential velocity is clearly continuous across the interface. For the data of Figure 5.2, the 1.5 : 1 viscosity ratio is represented by the green points and the 2.5 : 1 and 3.5 : 1 viscosity ratio data by the blue and red points respectively. Separate fits to data from the red / blue layers (with sites within two lattice spacings of a red-blue interface excluded from the regression) established the corresponding red / blue fluid shear rates. The ratio of the shear rates was determined and is presented in the table in Figure 5.3 correlating very well with the red / blue fluid viscosity ratio. Figure 5.4 plots these two ratios, and regression to this data was found to give a clear linear relationship, the fit giving a gradient of $m = 0.991 \pm 0.021$ and an ordinal-intercept of $c — 0.001 \pm 0.064$, in excellent agreement with the theoretical

Viscosity ratio	Velocity gradient ratio
1 : 1.5	1 : 1.505 ± 0.0005
1 : 2.5	1 : 2.513 ± 0.0005
1 : 3.5	1 : 3.522 ± 0.0005

Figure 5.3: Comparison of viscosity ratios with measured velocity gradient ratios

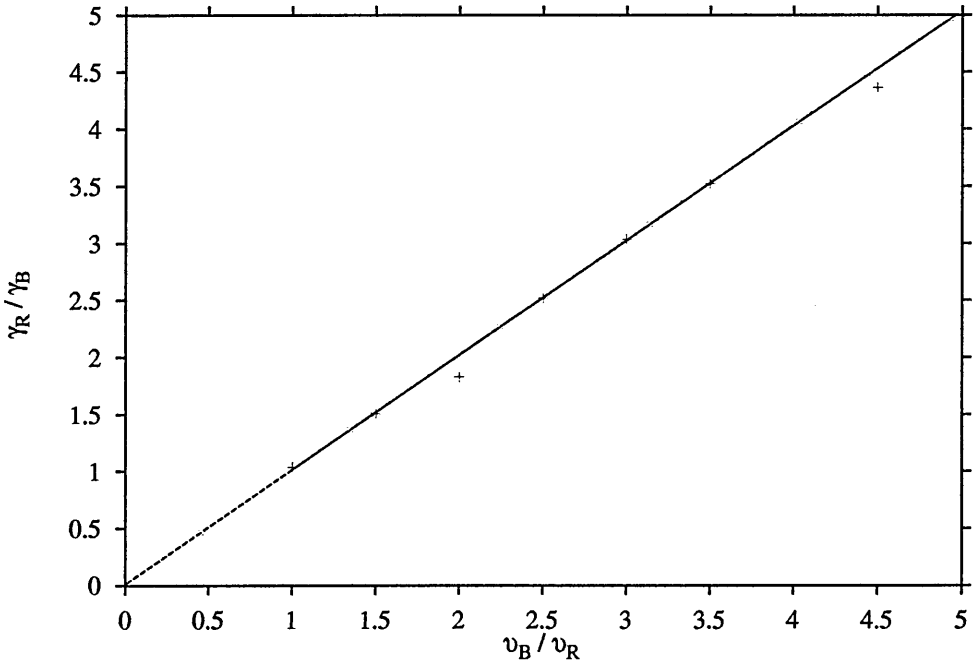

Figure 5.4: Variation between $\dot{\gamma}_R/\dot{\gamma}_B$ against ν_B/ν_R

relationship

$$\dot{\gamma}_R/\dot{\gamma}_B = \nu_R/\nu_B \tag{5.6}$$

derived from Eq. (5.4). For the data in this study a surface tension parameter of $\sigma = 0.0125$ was used, with a forcing increment of 0.02, the viscosity ranges were $\nu_R = 0.029412$ (corresponds to a relaxation parameter of $\omega = 1.7$) and $0.014076 \leq \nu_B \leq 0.147059$, $(1.1 \leq \omega \leq 1.7)$.

This first qualitative assessment of the LBGK interface supports, quantitatively correct hydrodynamical behaviour (as opposed to the hydrostatics measured by previous workers). Considerations of tangential stress transmission do not, however, quantitatively assess any correspondence between the surface tension measured in static Laplace Law tests and that surface tension which governs the dynamic response of the interface. This requires the investigation of the normal stress condition. We suggest that on the strength of the results presented in this section it is safe to conclude that tangential stresses are correctly handled by the LBGK interface. This assumption will assist our analysis of the normal stress behaviour, investigated in the next section.

5.3 Normal stress transmission

Consider a neutrally buoyant red fluid drop in a surrounding blue fluid of equal viscosity, deformed by a far–field shear flow. In two dimensions the drop deformation may be characterised by a single local radius of curvature $R(\theta)$. The situation is represented in Figure 5.5, in which the unit normal and (single) unit tangent at the red / blue interface must be related through

$$\hat{n}_y = -\hat{t}_z \qquad \hat{n}_z = \hat{t}_y \tag{5.7}$$

Writing the stress tensor as $\sigma_{\alpha\beta} = -p\delta_{\alpha\beta} + \sigma'_{\alpha\beta}$, using Eq. (5.7) and some algebra, we may combine the normal and tangential boundary condition equations Eq. (5.2)

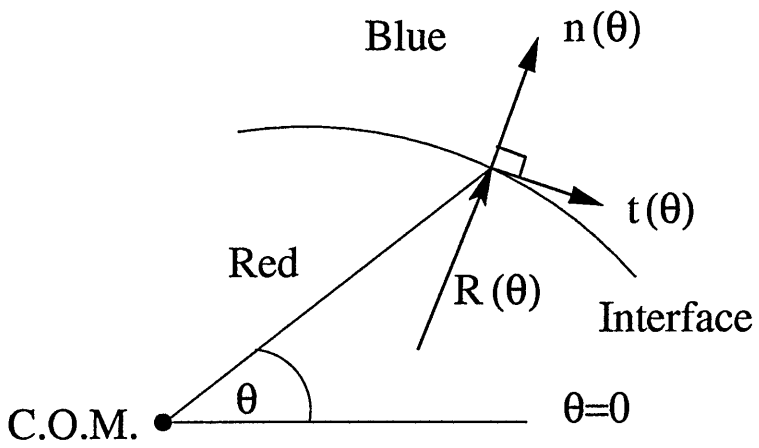

Figure 5.5: Schematic of the unit normal and tangent vectors for our $2D$ system, drawn at a site on the drop interface characterised by θ. $R(\theta)$ represents the local radius of curvature of the interface.

and Eq. (5.1) into a single form

$$p^R(\theta) - p^B(\theta) + 2\nu^R(\partial_y u_y^R + \partial_z u_z^R) - 2\nu^B(\partial_y u_y^B + \partial_z u_z^B) = \frac{\Sigma}{R(\theta)} \qquad (5.8)$$

in which all derivatives are evaluated at the location of the interface.

In the case of equal viscosity between the drop and the supporting fluid ($\nu^R = \nu^B$) and assuming a non–separating interface ($u_\alpha^R = u_\alpha^B$) we obtain from the last equation the result $\Delta p(\theta) = \frac{\Sigma}{R(\theta)}$. However, local behaviour is further complicated by the anisotropy of the LBGK interfacial tension already discussed in chapter 4. It has been shown that interfacial tension varies with orientation relative to the underlying D2Q9 lattice and θ, so that variation in the macroscopic surface tension parameter Σ with θ has to be admitted and

$$\Delta p(\theta) = \frac{\Sigma(\theta)}{R(\theta)} \qquad (5.9)$$

this result is true *in* $2D$ *only* and assumes tangential stress continuity (section 5.2). The local normal stress condition Eq. (5.9) appears as a pseudo–Laplace law or more

specifically in what we term a local Laplace Law form. The hydrostatic pressure difference $\Delta p(\theta)$ and radius of curvature $R(\theta)$, are obtained at a particular angular position θ on the interface (Figure 5.5). Thus, by measuring the local radius of curvature and pressure difference, and using the theory of chapter 4 to account for the angular variation of macroscopic surface tension, the extent to which Eq. (5.2) is valid for our interface may be assessed through Eq. (5.9). Our examination of the transmission of normal stress across a red / blue interface therefore proceeds by devising the means by which the radius of curvature measurements may be performed on a steady–state deformed fluid drop.

5.3.1 Radius of curvature measurement

The local radius of curvature $R(\theta)$ of the drop is needed for most lattice sites located on the drop interface. Drops are initialised centrally upon the lattice and sheared in the usual manner, to produce steady–state deformation. To determine $R(\theta)$, the lattice is initially scanned and the centre of mass of the fluid droplet located by calculating the moments of drop mass [43]. The coordinates (y, z) of each interface (mixed colour) site, relative to the drop centre, are then used to calculate the angle θ (Figure 1.5). The unit normal vector $\hat{\mathbf{n}}$ at position θ we calculate using simple differential geometry and the Frenet-Serret formula [50]

$$\frac{d\hat{\mathbf{t}}}{ds} = \kappa\hat{\mathbf{n}} \tag{5.10}$$

where $\hat{\mathbf{t}}$ is the unit tangent vector, s is length along the interface and κ is the interface curvature; the radius of curvature $R(\theta) = \kappa^{-1}$. For our two dimensional

study $\hat{n}_y = -\hat{t}_z$ and $\hat{n}_z = \hat{t}_y$ and we may substitute components of the unit normal with the unit tangent components and consider the unit normal (to the interface) in terms of components of the associated tangent. Expanding Eq. (5.10) in terms of subtended angle θ

$$\frac{d\hat{\mathbf{t}}}{ds} = \frac{d\hat{\mathbf{t}}}{d\theta}\frac{d\theta}{ds} \tag{5.11}$$

in which

$$\frac{d\theta}{ds} = \left[\left(\frac{dy}{d\theta}\right)^2 + \left(\frac{dz}{d\theta}\right)^2\right]^{-\frac{1}{2}} \equiv \left|\frac{d\theta}{d\mathbf{r}}\right| \tag{5.12}$$

Appealing to the definition of the unit tangent vector $\hat{\mathbf{t}}$

$$\hat{\mathbf{t}} = \frac{d\mathbf{r}}{ds} \tag{5.13}$$

we may rewrite Eq. (5.11) using Eqs. (5.12,5.13) as

$$\begin{aligned} \frac{d\hat{\mathbf{t}}}{ds} &= \left|\frac{d\mathbf{r}}{d\theta}\right|^{-1}\frac{d}{d\theta}\frac{d\mathbf{r}}{ds} \\ &= \left|\frac{d\mathbf{r}}{d\theta}\right|^{-1}\frac{d}{d\theta}\left[\frac{d\mathbf{r}}{d\theta}\left|\frac{d\mathbf{r}}{d\theta}\right|^{-1}\right] \end{aligned} \tag{5.14}$$

Performing the differentiations in Eq. (5.14), we calculate the y and z components of the tangent vector to be

$$\frac{d\hat{\mathbf{t}}_y}{ds} = \left|\frac{d\mathbf{r}}{d\theta}\right|^{-2}\left[\frac{d^2y}{d\theta^2} - \frac{dy}{d\theta}\left|\frac{d\mathbf{r}}{d\theta}\right|^{-2}\left(\frac{d^2y}{d\theta^2}\frac{dy}{d\theta} + \frac{d^2z}{d\theta^2}\frac{dz}{d\theta}\right)\right] \tag{5.15}$$

$$\frac{d\hat{\mathbf{t}}_z}{ds} = \left|\frac{d\mathbf{r}}{d\theta}\right|^{-2}\left[\frac{d^2z}{d\theta^2} - \frac{dz}{d\theta}\left|\frac{d\mathbf{r}}{d\theta}\right|^{-2}\left(\frac{d^2y}{d\theta^2}\frac{dy}{d\theta} + \frac{d^2z}{d\theta^2}\frac{dz}{d\theta}\right)\right] \tag{5.16}$$

From Eq. (5.10), the radius of curvature $R(\theta)$ can now be written in terms of the y and z components of the unit tangent

$$\frac{1}{R(\theta)} = \left|\frac{d\hat{\mathbf{t}}}{ds}\right| = \left[\left(\frac{d\hat{\mathbf{t}}_y}{ds}\right)^2 + \left(\frac{d\hat{\mathbf{t}}_z}{ds}\right)^2\right]^{\frac{1}{2}} \tag{5.17}$$

in which the terms in square brackets may be replaced using Eq. (5.15) and Eq. (5.16). We now consider the interface site coordinates (y, z) as functions of a continuous θ and write each of y and z in terms of their associated Fourier series (of period π), using primes to distinguish different Fourier components of the y and z coordinates

$$y(\theta) \approx \frac{a_0}{2} + \sum_n [a_n sin(n\theta) + b_n cos(n\theta)] \tag{5.18}$$

$$z(\theta) \approx \frac{a'_0}{2} + \sum_n [a'_n sin(n\theta) + b'_n cos(n\theta)] \tag{5.19}$$

This allows the derivatives like *e.g.* $\frac{d^2z}{d\theta}$ found in Eq. (5.15) to be written in terms of amplitudes a_0, a_n, b_n, a'_0, a'_n and b'_n. Fourier amplitudes a_0, a_n and b_n *etc.* may, in turn be approximated at a given (measured) $y(\theta)$ by numerical integration

$$a_0 = \frac{1}{\pi}\int_{-\pi}^{\pi} y(\theta)d\theta \approx \frac{1}{\pi}\sum y(\theta_i)\Delta\theta_i \tag{5.20}$$

$$a_n = \frac{1}{\pi}\int_{-\pi}^{\pi} y(\theta)sin(n\theta)d\theta \approx \frac{1}{\pi}\sum y(\theta_i)sin(n\theta_i)\Delta\theta_i \tag{5.21}$$

$$b_n = \frac{1}{\pi}\int_{-\pi}^{\pi} y(\theta)cos(n\theta)d\theta \approx \frac{1}{\pi}\sum y(\theta_i)cos(n\theta_i)\Delta\theta_i \tag{5.22}$$

$$\Delta\theta_i = \left|\theta_i - \theta_{(i-1)}\right| \tag{5.23}$$

where $\Delta\theta_i$ is the (small but irregular) angular interval between neighbouring interfacial sites. The local radius of curvature, at given θ was thus determined, *from a fit to the whole drop interface* using equations Eq. (5.17). As a check, the co-ordinates $(y(\theta), z(\theta))$ were similarly obtained from Fourier components Eqs. (5.18,5.19). Figure 5.6 shows the position of an (un-sheared) predicted interface (blue line), for a drop of undeformed radius $R = 40$, $\sigma = 0.005$ and $\omega = 1.5$, overlaid with the actual discrete measured interfacial sites (green points). Figure 5.7 shows similar results for a moderately deformed drop with the same simulation parameters. By a process of

trial and error, it was found that retaining the first ten Fourier harmonics ($n = 10$) was sufficient to obtain excellent agreement between the measured and predicted drop interface, allowing us to invest considerable confidence in the robustness and accuracy of our local radius of curvature measurements.

Figure 5.8 shows the calculated radius of curvature $R(\theta)$ obtained by our Fourier fitting technique, for the drop in Figure 5.6 with an originally undeformed radius of $R = 40$ lattice units. The drop is seen to exhibit (approximately) the expected periodic trend with repeated local structure over intervals $-\pi \leq \theta \leq 0$ and $0 \leq \theta \leq \pi$. The discrete nature of the simulation and interface is however evident, as the two halves of the drop are seen to have evolved in a slightly different manner, which asymmetry is attributable to the fact that the interface is predominately singular. For completeness, the mean value of the collected radius data gives a value of $\bar{R} = 40.236$ and it is appropriate again to emphasise that after Figure 5.6, the reconstruction of the drop interface using the discrete Fourier series validates the radius of curvature results obtained by this method.

5.3.2 Pressure "jump" calculation

The pressure jump across the interface $\Delta p(\theta)$, should clearly be measured as close as possible to the colour interface, but (we suggest) outside of the region about the interface in which the pressure oscillates (see chapter 4). By shrinking and expanding the Fourier fit to the interface, by (say) ≈ 10 lattice sites it is possible to find a pair of contours concentric and locally parallel with the interface, these points

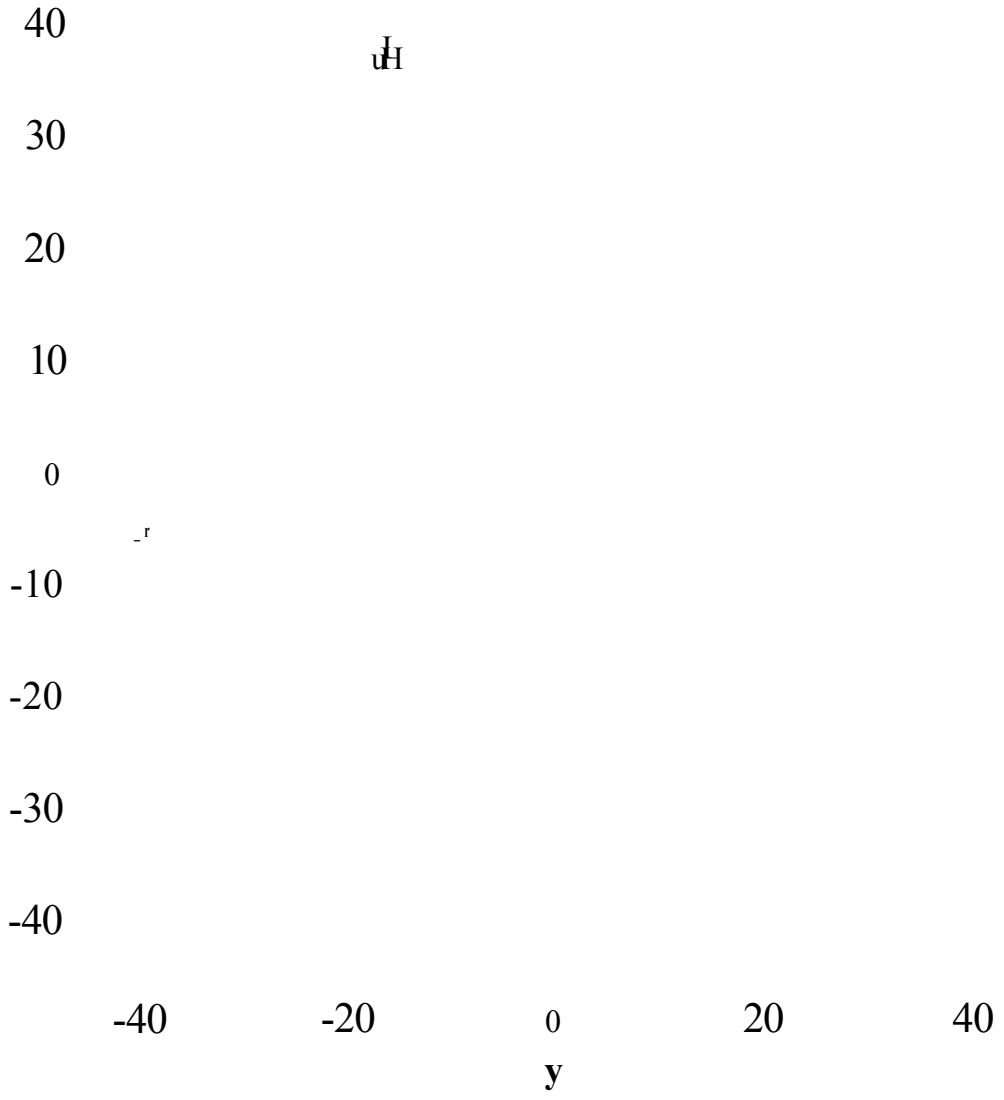

Figure 5.6: Simulated interface data for an un-sheared drop, superposed with the discrete Fourier fit to the interface for a drop with R = 40, a = 0.005 and U = 1.5.

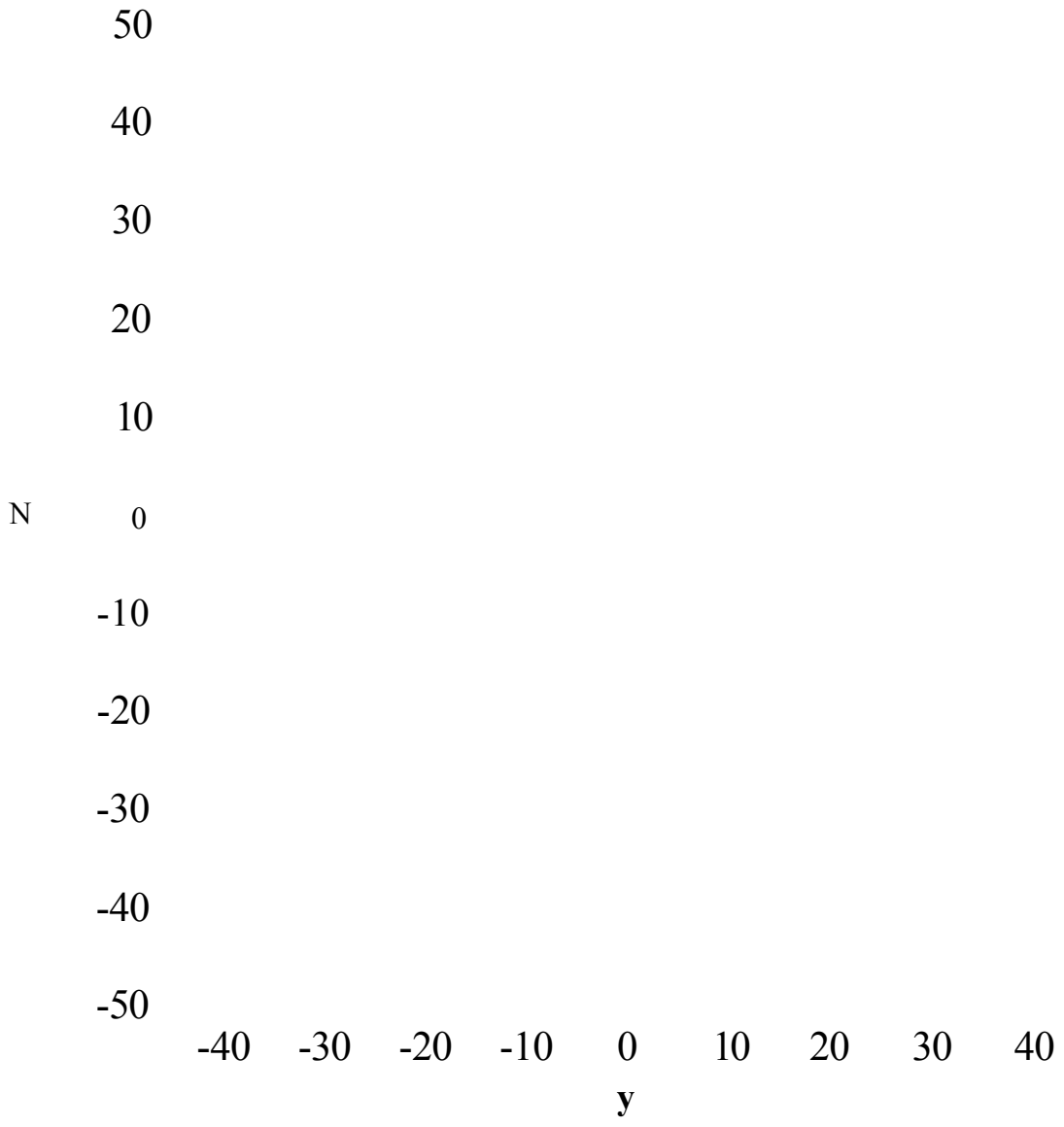

Figure 5.7: Simulated interface data for a sheared drop, superposed with the discrete Fourier fit to the interface for a drop with $R = 40$, $a = 0.005$ and $u = 1.5$.

Figure 5.8: Radius of curvature *R(6)* against *0* for the undeformed drop of Figure 5.6.

are characterised by the interface angle *9* Figure 5.9. Density (pressure) measured at points identified using this method are inevitably *off-lattice,* necessitating the use of linear interpolation between lattice nodes in order to infer pressures at these points and hence a pressure jump. The decision to avoid the region of the lattice in which the density is influenced unphysically by the interface means that what is measured in this way is only approximately a *normal* pressure jump.

Figure 5.10 shows the measured pressures in the fluid drop (green points) and the supporting fluid (blue points) with respect to angle *0.* Both sets of data show broadly the same periodic fluctuations with loosely coinciding local maxima and minima. The average pressure outside the drop is $p \approx 0.6$, calculated from the local density which corresponds to the initial site density $p = 1.8$. The drop pressure

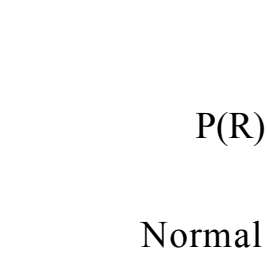

Figure 5.9: Schematic representation of the location of pressure measurement.

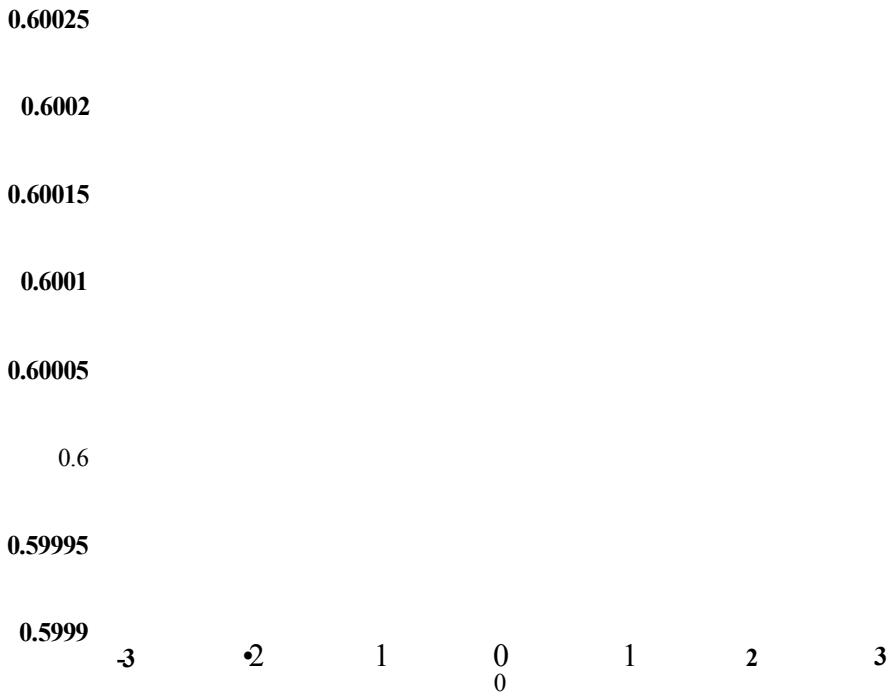

Figure 5.10: Variation of static fluid pressure p with rotational angle *9* for the undeformed drop of Figure 5.6.

data is seen to exhibit a far flatter overall profile, which does not correspond as correctly as the external pressure to the drop radius of curvature. Note also the correct hydrodynamical correspondence between the minimum pressure difference at intervals of (where *n* is an odd integer), which corresponds with the local maximum radius of curvature in Figure 5.8.

5.3.3 Numerical calculation of surface tension

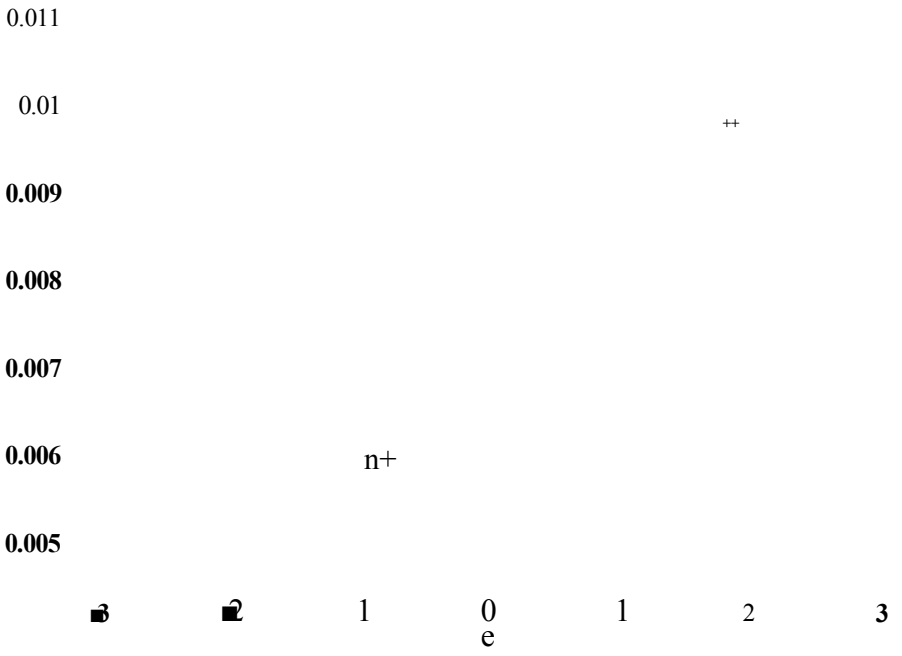

Figure 5.11: Variation of macroscopic surface tension £(0) with rotational angle *9* for the undeformed drop of Figure 5.6.

The local Laplace law macroscopic surface tension E*(9)* is shown in Figure 5.11 and is seen to display the correct qualitative periodic structure expected as E(0) is known to be anisotropic. The data reflects the angular dependence implicit in *R(9)* and *p(9)* and was extracted from a simulation of a static (un-sheared) drop

(see Figure 5.6) initialised on a 150×150 lattice, we remind the reader of the drop simulation parameters of $R = 40$, $\sigma = 0.005$ and $\omega = 1.5$. The minimum (maximum) value of surface tension $\Sigma(\theta)$ is observed to be $\Sigma(\theta)_{min} \approx 0.005$ ($\Sigma(\theta)_{max} \approx 0.011$). The degree of drop surface tension anisotropy may be quantified by introducing an anisotropy factor

$$A_\sigma = \frac{\Sigma(\theta)_{max}}{\Sigma(\theta)_{min}} \tag{5.24}$$

for the data shown in Figure 5.11 $A_\sigma \approx 2.2$. This value arises in part as a result of a tendency of the interface to adhere to lattice directions. Calculations in the last chapter have already shown that the macroscopic surface tension depends upon the orientation of the interface. Similar dependence of surface tension upon interface orientation is apparent from local Laplace Law calculations Figure 5.11.

A close examination of the interface's constitution reveals it to be highly singular, and except at a few isolated positions the drop interface does not exhibit the structure considered in the theory of the last chapter. This of course is unsurprising, for the cases considered in the last chapter were planar symmetric interfaces possessing an infinite radius of curvature and, as such were constrained to allow no density (pressure) gradient or microcurrent. Whilst the drop interface does exhibit a tendency to adhere to the lattice effectively lying parallel to lattice directions, at no point do we expect there to occur zero pressure across the interface, or infinite radius of curvature. Thus the quantitative structure exhibited by Figure 5.11 cannot be mapped directly to our earlier developed theory. Qualitatively we expect to see evidence of surface tension anisotropy, which is clearly evident with the correct

period.

A standard Laplace formula measurement to obtain the macroscopic surface tension was performed by calculating the mean static pressure inside the drop $\bar{p}_R$ up to a radius of $r \leq 32$ lattice units from the drop centre and the external mean pressure $\bar{p}_B$ was calculated at a radius $r \geq 48$. The radius of the drop was taken as the initialised drop radius $R = 40$

$$\Sigma = R\,(\bar{p}_R - \bar{p}_B) \tag{5.25}$$

For the same drop the standard Laplace surface tension $\Sigma = 0.00772$ was measured, this value lies in the centre of the local macroscopic surface tension data Figure 5.11 and differs by only a small amount from the mean simulated surface tension $\bar{\Sigma}(\theta) = 0.00797$, thus $\Sigma \approx \bar{\Sigma}(\theta)$ and is in good quantitative agreement as we would expect.

If we repeat the study for a moderately deformed drop see Figure 5.7 using the same simulation parameters, as the drop deforms it produces larger spikes in the radius of curvature measurement Figure 5.12. These spikes correspond with the flattening of the interface, and are a real artifact of the discrete nature of the lattice. However even though the radius of curvature spikes are considerably greater for the deformed drop the surface tension is qualitatively the same Figure 5.13, with a mean value of $\bar{\Sigma}(\theta) = 0.00781$, approximately the same as the undeformed drop.

Qualitatively the static and moderately deformed drops show the correct surface tension structure, however they show quantitatively different details from our developed theory. The closed drop is made up of vertical / horizontal and 45^0 orientated

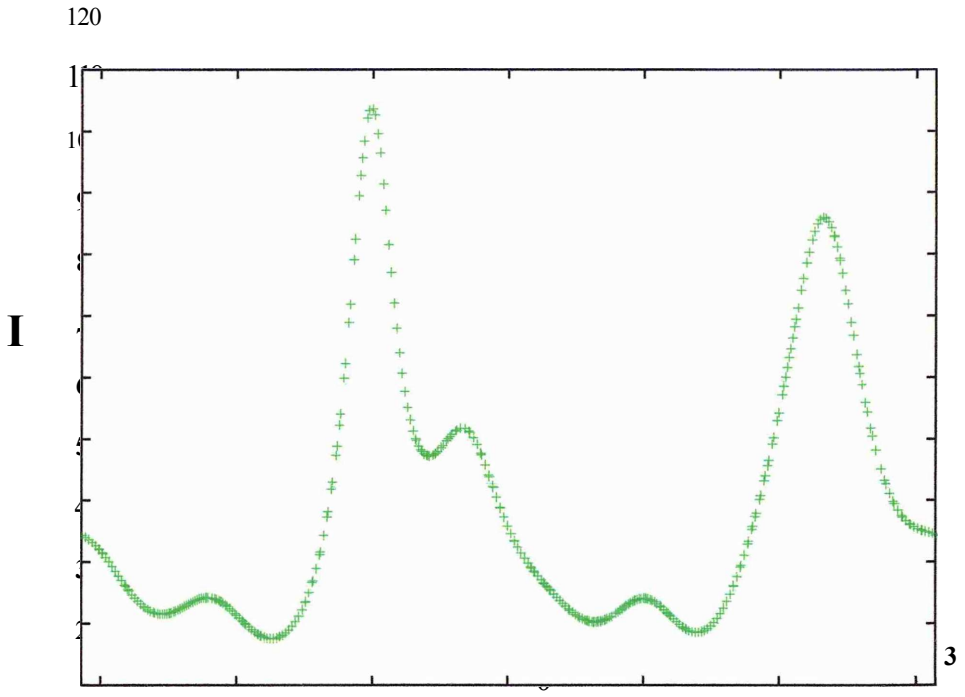

Figure 5.12: Radius of curvature *R(9)* against *6* for a moderately deformed drop.

interface segments, thus we expect a surface tension value to be approximately in the middle of this range. For our interface to support "correct" hydrodynamical boundary conditions the local surface tension would ideally produce a flat profile, with no oscillation. This profile would be derived from a constant radius of curvature and pressure difference across the interface for an undeformed drop. A constant radius of curvature and pressure difference is unattainable in our simulation due to the discrete nature of the lattice, however we may endeavour to reduce the surface tension anisotropy by reducing the amplitude of oscillation in Figure 5.11 by modification of the interface segregation rule. As the oscillation is reduced the interfacial boundary conditions will become more hydrodynamic and produce a closer mapping to Laplace law. We will now attempt to *tune* our model to reduce anisotropy and

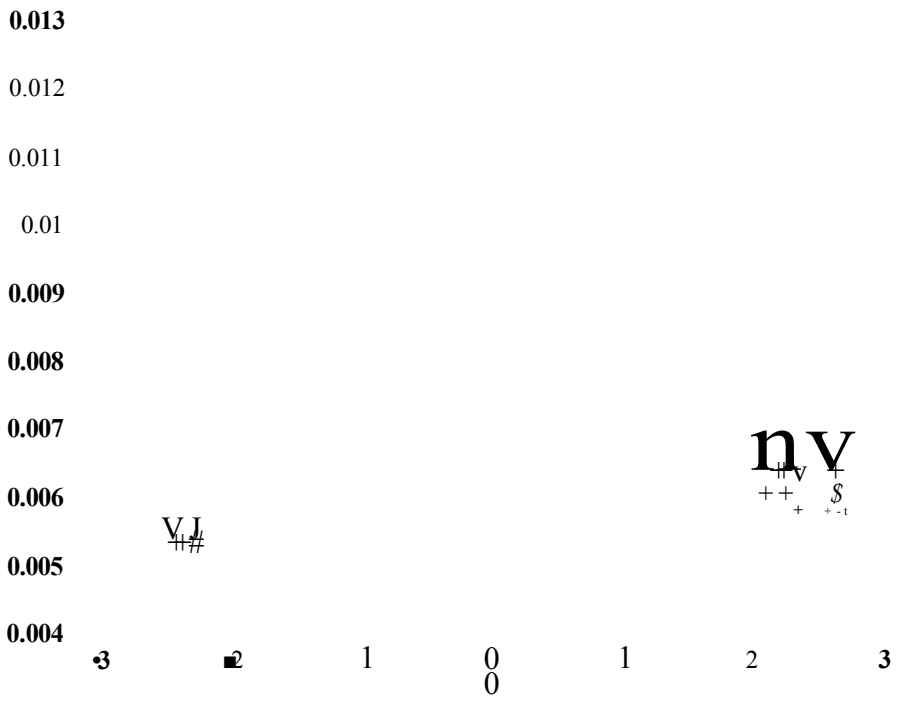

Figure 5.13: Variation of macroscopic surface tension E(0) with rotational angle *9* for a moderately deformed drop (see corresponding radius of curvature data).

try to make the pressure map more closely to the radius of curvature.

5.4 Surface tension with improved isotropy

A further modification is required to our interface segregation rule in order to improve the mapping of the static pressure to the drop radius of curvature and most importantly reduce the surface tension anisotropy of the interface *A a.* To improve the interface isotropy we aim to decrease *E(9)max,* we note that approximately the same result may achieved by increasing E(0)m*n or by using a combination of the two approaches. This final modification to the segregation rule results in the general

form

$$\Delta N_i(\mathbf{x},t) = \sigma\ g(\theta)C(\mathbf{x},t)\ cos(2(\theta_f(\mathbf{x}) - \theta_i)) \tag{5.26}$$

where $g(\theta)$ is a newly introduced angular function increasing surface tension isotropy and all other terms have their usual meaning. The $g(\theta)$ term may take many forms however we choose the simple computational efficient form

$$g(\theta) = \left[1 + k\ cos^2(2\theta_f(\mathbf{x}))\right] \tag{5.27}$$

where k is a negative real number in the range of $-1 \leq k \leq 0$ and the only tunable variable in this newly introduced parameter.

5.4.1 Optimisation of isotropy

To improve the surface tension isotropy of the drop interface, optimisation of the factor k in our newly developed interface perturbation is required, as we aim to decrease $\Sigma(\theta)_{max}$. An approximate optimum value of k may be predicted by considering the initial anisotropy factor value of the unmodified perturbation scheme where $A_\sigma \approx 2.2$. Consider the macroscopic surface tension $\Sigma(\theta)$ scaled with the newly introduced factor $g(\theta)$, where $\Sigma(\theta)_{max} = \Sigma(0)$ and $\Sigma(\theta)_{min} = \Sigma(\frac{\pi}{4})$ see Figure 5.11, to give

$$\Sigma(0)\ g(0) = \Sigma(\frac{\pi}{4})\ g(\frac{\pi}{4}) \tag{5.28}$$

rearranging Eq. (5.28) and using equation Eq. (5.24), we may write the anisotropy factor as

$$A_\sigma = \frac{\Sigma(0)}{\Sigma(\frac{\pi}{4})} = \frac{g(\frac{\pi}{4})}{g(0)} \tag{5.29}$$

Using the general form of the angular function $g\{0) — [1 + k\ cos2(26/(x))]$, it implies $\#(\mathbf{0}) = \mathbf{1}\ \mathbf{4}\ \blacksquare k$ and $g\{\backslash) — \mathbf{1}$ therefore

$$A, \quad \begin{matrix} 0(f) & 1 \\ 0(0) & 1 + \boldsymbol{k} \end{matrix} \tag{5.30}$$

giving an approximate value of minimum surface tension anisotropy at $k — —0.52$. This approximate value is confirmed by simulation Figure 5.14. The continuous line is a quadratic fit to the data of the form $ax2\ \mathbf{4}\ bx\ \mathbf{4}\ c$ where $a = 9.525$, $b = 9.714$ and $c = 4.296$.

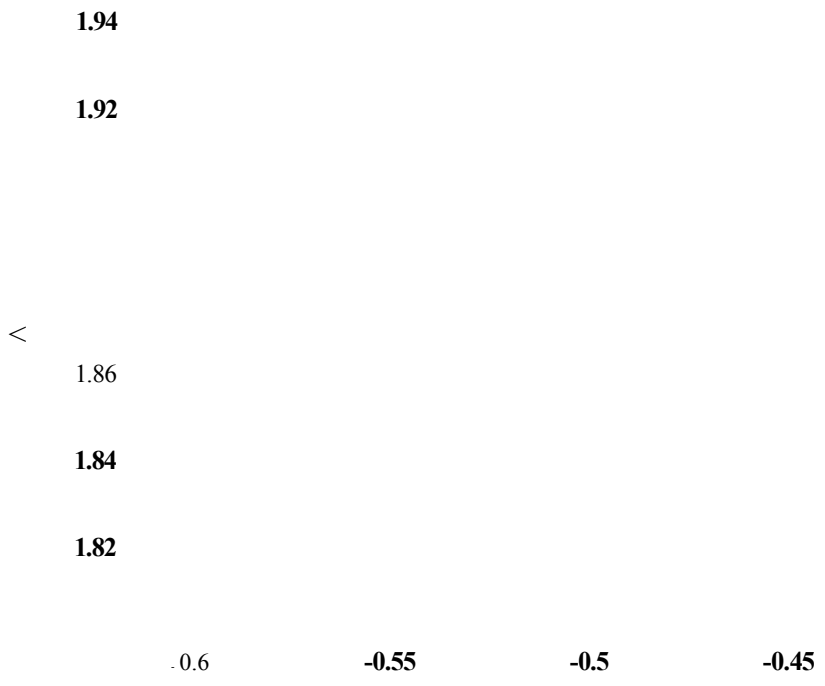

Figure 5.14: Variation of drop anisotropy $A\,a$ with perturbation factor k

The inclusion of this new cosine squared term has the effect of adding an oscillatory factor to the interfacial perturbation which makes the pressure adhere more closely to the local variation in the drop radius of curvature Figure 5.15. Comparison with Figure 5.10 shows a major improvement in the correspondence between the local

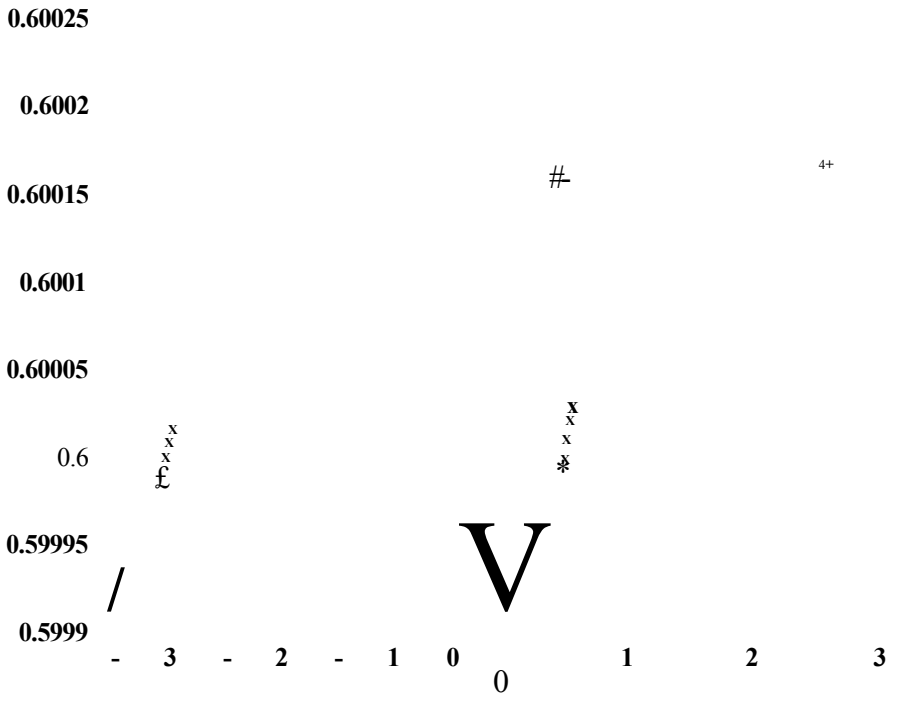

Figure 5.15: Variation of static fluid pressure p with rotational angle *9.* The green points indicate the internal pressure of the drop and the blue points indicate the external supporting fluid pressure.

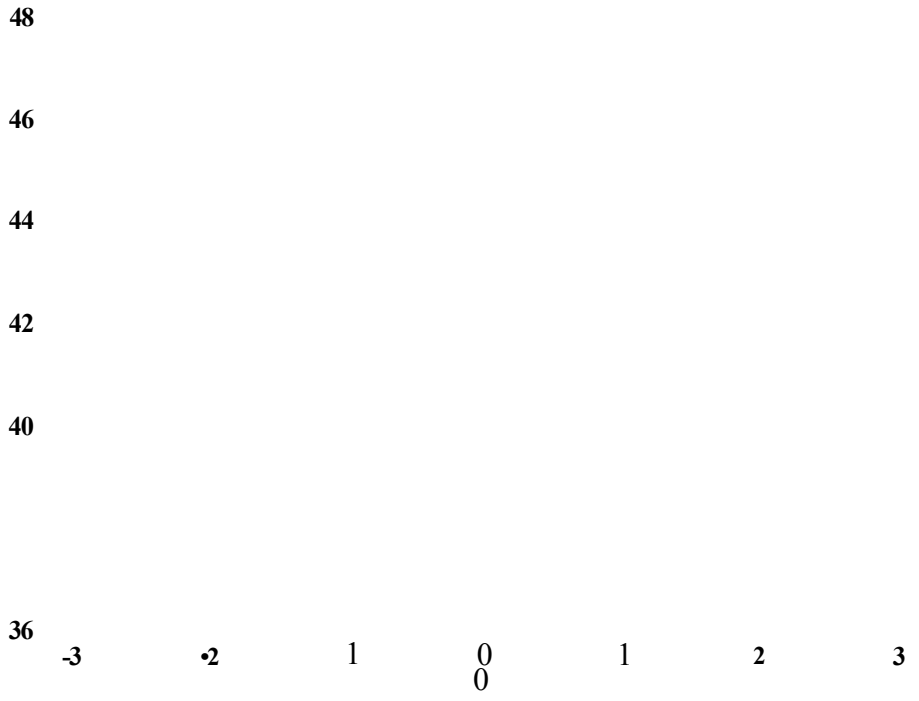

Figure 5.16: Variation of radius of curvature $R(9)$ with rotational angle 9.

maxima and minima of the red and blue fluid pressures. The flatter profile of the higher fluid drop pressure (green points) Figure 5.10 has been transformed. The closer mapping of the pressure to the local radius of curvature has the effect of squeezing the interface and thus increasing the periodicity of the the local radius of curvature Figure 5.16. The effect of the new perturbation on the anisotropy of the drop surface tension is seen in a reduction of the amplitude in the local Laplace law surface tension Figure 5.17, compared with Figure 5.11 the anisotropy of the surface is seen to reduce to Aa & 1.88 with k = —0.52 we note that the same simulation parameters of R = 40, a — 0.005 and UJ = 1.5 are used. A statistical comparison of the variance and the standard deviation of the improved isotropy interface with the unmodified interface is presented in the table in Figure 5.18 and shows a re-

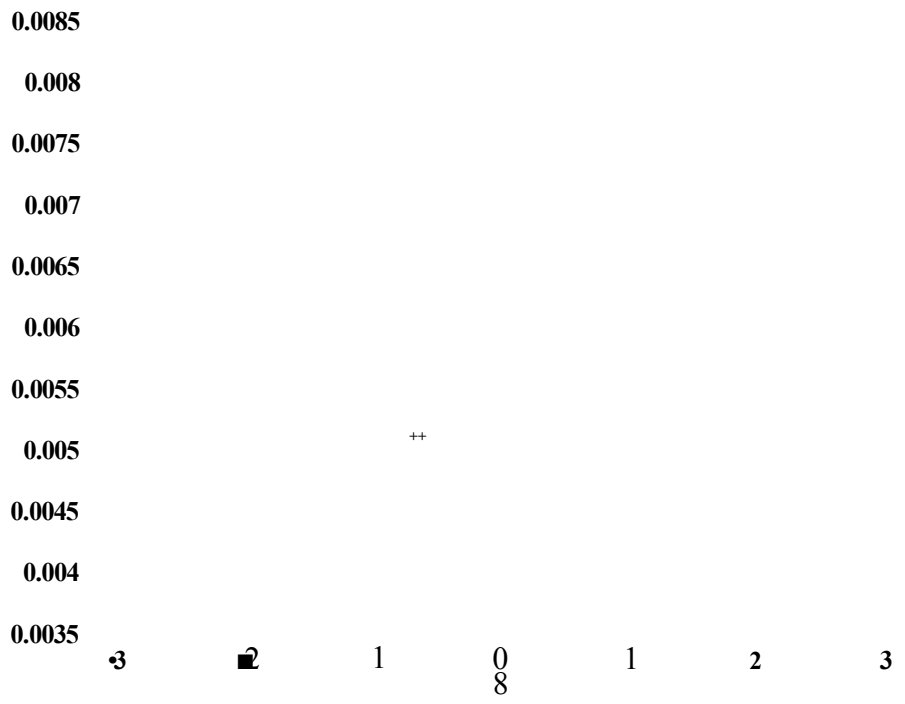

Figure 5.17: Variation of macroscopic surface tension E with rotational angle *0.*

duction in the standard deviation of the surface tension and an improvement in the hydrodynamics of the interface.

Interface type	mean E *(9)*	Variance	Standard Deviation
Unmodified interface	7.97 x 1(T3	3.14 x 1(T6	1.77 x 10~3
Improved isotropy interface	6.49 x 10"3	1.32 x 1<T6	1.15 x 1CT3

Figure 5.18: Comparison of the variance and standard deviation in the the local Laplace law surface tension E(0) between the unmodified and improved isotropy interface.

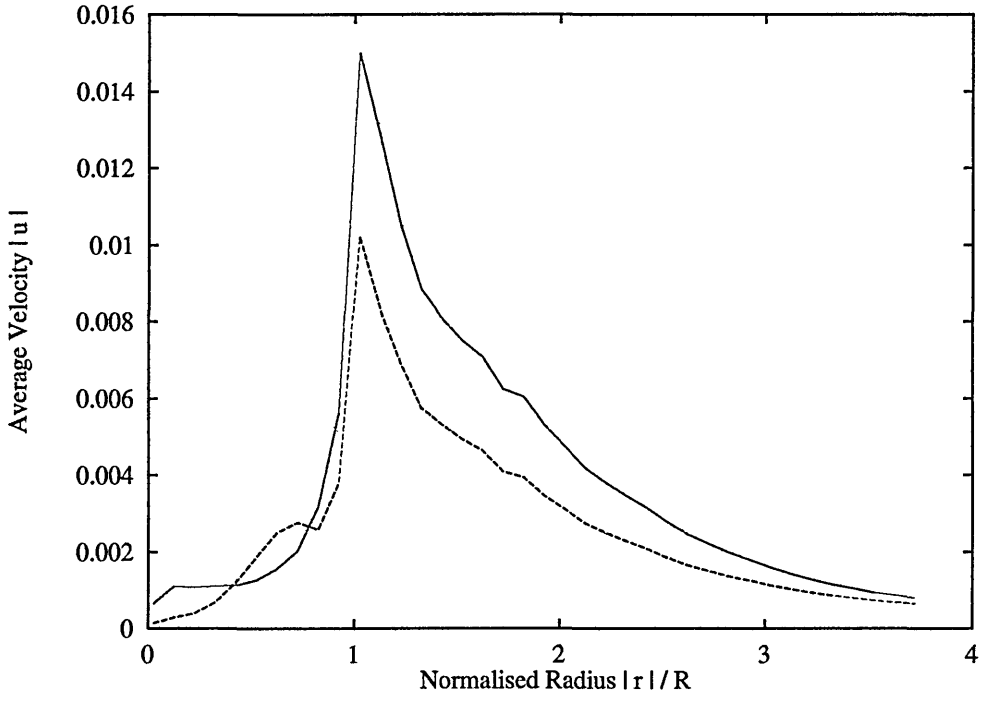

Figure 5.19: Variation of $|\mathbf{u}|$, microcurrent flow speed measured in units of lattice spacing per time step, against normalised distance from the drop centre, $|\underline{r}|/R$ at $\sigma = 0.005$ for the unmodified interface (green line) and the improved isotropy interface (blue line) at $k = -0.524$.

5.4.2 Microcurrent reduction

Figure 5.19 shows the variation of microcurrent flow speed $|\mathbf{u}|$ measured in units of lattice spacing per time step, against normalised distance from the drop centre $|\underline{r}|/R$ for our steady–state drop. The green line shows the magnitude of microcurrent using the unmodified interface perturbation, the blue line with lower maxima shows the magnitude of microcurrent activity using the new interface perturbation at $k = -0.52$. Note the approximately linear trend in peak flow activity at the interface. The maximum value of $|\mathbf{u}|_{max}$ is seen to be reduced by approximately one third. Comparisons by other workers of the microcurrents induced in Rothman–Keller derivative interfaces compared with Shan–Chen type interfaces [28] have shown that $|\mathbf{u}|_{max}$ is twice as large in the Rothman–Keller interface at the same interface perturbation parameter σ [51]. Thus the reduction in magnitude of the microcurrent produces a maximum velocity which is of the same order as the Shan–Chen interface.

5.5 Conclusions

Simulation measurements of the transmission by the immiscible fluid interface of tangential stress, by the investigation of the relationship between fluid shear and fluid viscosity in planar symmetric (blue–red–blue) interfaces shows comprehensive agreement with theory.

The examination of normal stress transmission in a simulation by substitution of the tangential stress components, has allowed the development of an Fourier interface investigation technique. This technique makes no predetermined assumption about the shape of the fluid drop, thus all analysis is based solely upon the discrete singular nature of the interface. This has allowed a quantitative analysis of the anisotropy of the macroscopic drop surface tension to be made for static and moderately deformed drops. It has also facilitated the development of an new computationally efficient interface perturbation technique with improved macroscopic surface tension isotropy. However, this improvement is not as large as might have been hoped.

The local radius of curvature measurement for the modified scheme Figure 5.16, is dependent upon the interface adhering to the lattice. Thus the geometrically improved isotropy drop gives the best attainable radius of curvature for the lattice shape. Qualitatively Figure 5.16 contains the same structure as the initialised *un-evolved* drop Figure 5.20. Thus Figure 5.20 is an illustration of how circular a drop can be made on the lattice, without further modification to our model, due to lattice *pixelation* effects. We note that pixelation errors may be reduced by simulating

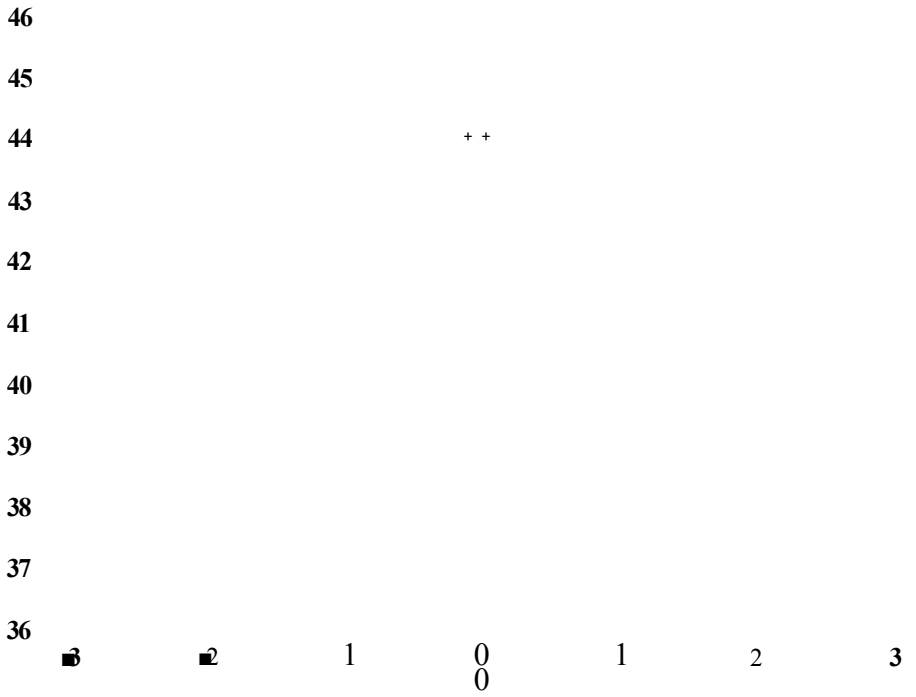

Figure 5.20: Variation of radius of curvature *R(9)* with rotational angle *9* for an unevoled drop.

drops with a radius $R > 10$ lattice units. Finally, our newly developed interface generation scheme benefits from increased adherence of drop pressure to the local radius of curvature and a reduction in the magnitude of the microcurrent by one third is seen.

Chapter 6

Induced drop deformation and burst

6.1 Introduction

As an application of our newly developed model we examine the deformation and burst of neutrally buoyant immiscible fluid drops subjected to a simple hydrodynamic shears. Measuring the dependence of critical shear rate $\dot{\gamma}_c$ for drop rupture on flow parameters, we aim to validate the model over a range of simulation variables. Investigation of the model's interfacial surface tension parameter σ, drop radius R and relaxation parameter ω and their effect upon the burst process is required in order to confirm the model exhibits the correct qualitative theoretical and experimental hydrodynamic behaviour. We employ the interface perturbation used in

chapter 4, to generate the interface between our immiscible fluid components. This is equivalent to our improved isotropy interface with parameter $k = 0$, as issues relating to isotropy are not concerns we wish to address in this chapter.

Drop deformation was first investigated experimentally by Taylor [52] and by Rumscheidt and Mason [53] for simple shear and plane hyperbolic flows. Fluid drops were deformed under shears by using Couette device and a four–roller apparatus respectively to induce external flows. Theoretical [54, 55] and numerical simulation results [43, 45] have been obtained for two dimensional drop deformations. Experimental, theoretical and numerical results [56, 57, 58] have been obtained for three dimensional systems. These results include the examination of large drop deformations and provide results for drops deformed in surrounding fluids of equal viscosity.

6.2 Theory of drop deformation

Drop deformation may be characterised in a dimensionless form by defining a drop deformation parameter D, where D lies in the range of $0 \leq D < 1$. Following Taylor

$$D = \frac{a - b}{a + b} \tag{6.1}$$

where a and b are the maximum and minimum distances measured from the drop centre to a point on the drop surface see Figure 6.1. For a spherical drop $a = b$ and $D = 0$, whilst for a long thin drop $D \to 1$.

Taylor first approximated the radius of a fluid drop which would resist the viscous

stresses of a supporting fluid in shear in the small deformation regime ($D \ll 1$) as

$$R = \frac{8\Sigma(\eta + \eta')}{\dot{\gamma}_c(19\eta' + 16\eta)\eta} \tag{6.2}$$

where η (η') is the suspending (drop) fluid shear viscosity and Σ is the macroscopic surface tension parameter. Thus Taylor's estimate Eq. (6.2), only indicates the conditions above which marked deviations from a spherical shape occur. Therefore Eq. (6.2) is taken as a comparison with theory, and the functional form for the critical shear rate $\dot{\gamma}_c$ at rupture is given by

$$\dot{\gamma}_c = \frac{\Sigma}{R\eta} f(\phi) \tag{6.3}$$

where $f(\phi)$ is a function of the viscosity ratio $\phi = \eta/\eta'$. Assuming that Eq. (6.3) is accurate, the dependence of $\dot{\gamma}_c$ may be rewritten by substituting for the kinematic viscosity

$$\nu = \frac{1}{6}\left[\frac{2}{\omega} - 1\right] \tag{6.4}$$

where $\nu = \eta/\rho$ and the macroscopic surface tension parameter is approximated by $\Sigma(\sigma, \omega) \sim \sigma/\omega$ giving

$$\dot{\gamma}_c \sim \frac{\sigma}{R} g(\rho, \phi) \left(\frac{1}{2 - \omega}\right) \tag{6.5}$$

and all other parameters have their usual meaning. The need for a determination of $g(\rho, \phi)$ may be avoided by constraining $\eta = \eta'$, thus making the two fluids the same viscosity and hence the viscosity ratio $\phi = 1$ (i.e. both fluids are relaxed using the same ω) in all the simulations. This allows Eq. (6.5) to be used to examine the relationship between the critical shear rate $\dot{\gamma}_c$ and the surface tension parameter σ and reciprocal drop radius $\frac{1}{R}$. Rearrangement and expansion of Eq. (6.5) to examine

the variation of $\frac{1}{\dot{\gamma}_c}$ with ω, is noted to give a predicted gradient / intercept ratio $m/c = -0.5$ see Eq. (6.6).

$$\frac{1}{\dot{\gamma}_c} \sim \frac{2R}{\sigma g(\rho, \phi)} - \frac{\omega R}{\sigma g(\rho, \phi)} \tag{6.6}$$

6.3 Experimentally observed drop deformations

In order to examine the ratio of flow forces attempting to deform and burst the drop to the surface tension we may define a Capillary number Ca [56]

$$Ca = \frac{\dot{\gamma} R \eta}{\sigma} \tag{6.7}$$

The capillary number is important when we wish to quantify the type of flow that is deforming a drop, once this is known along with the viscosity ratio ϕ we may predict the expected deformation or burst of the drop.

In a weak simple shear flow ($Ca \ll 1$) and $\phi = 1$ an initially circular drop is seen to deform to an elliptical shape, its principle axis is seen to orientate at an angle α to the direction of the flow Figure 6.1 [56]. As the flow rate is increased the drop shape elongates further, and an initial change in α is seen, the drop undergoes an initial rotation as the shear rate is increased initially reducing α. Under moderate shears the drop equilibrates itself to the increased external flow and α is seen to return to $\alpha \approx \frac{\pi}{4}$. An oscillation in the deformation parameter D and orientation angle α is seen as a result of this re–equilibration. As the drop is subjected to higher shear rates its shape is seen to deform further into an elongated "S" shape, as the drop necks it is seen to burst.

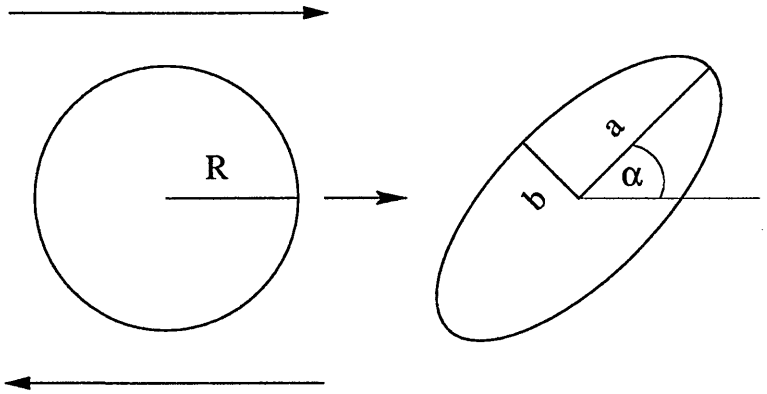

Figure 6.1: Schematic of drop deformation under a simple shear flow, the large arrows indicate the deforming flow direction.

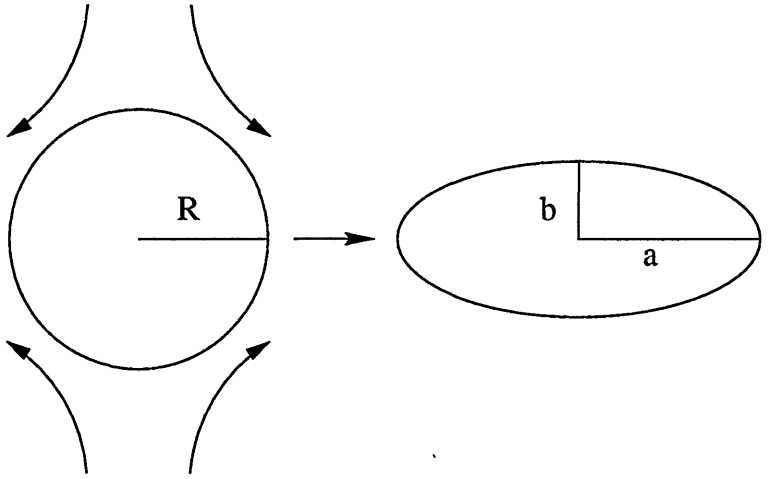

Figure 6.2: Schematic of drop deformation under an irrotational shear flow, the large arrows indicate the deforming flow direction.

In solenodial irrotational (plane hyperbolic) flow at small Ca and $\phi = 1$ an initially spherical drop is seen to deform to an elliptical shape, its principle axis is seen to orientate with the lattice y–direction Figure 6.2. If the flow rate is increased the drop is seen to deform further until a critical shear rate is reached and the drop will burst.

6.4 Simulation

In the simple shear flow examination of suspended fluid drops, a line of equally spaced neutrally buoyant red component fluid drops were simulated suspended in a supporting blue fluid of equal viscosity. This was achieved by simulating a drop located centrally on a 90×60 lattice, subjected to a uniform y–direction shear (see Figure 6.1) and employing periodic boundary conditions on the lattice edge sites. The hydrodynamic shear was induced in the far field of the drop by adding a uniform velocity to boundary links. Positive y–direction velocity was added to the top of the lattice, whilst negative y–direction velocity was added to the bottom of the lattice of the suspending blue fluid. This velocity increment was added at each update of the lattice after the collision step (pre–propagate) allowing the advection of the lattice to propagate the shear flow.

The implementation of this scheme produces a shear field within the suspending fluid, which is proportional to the forcing increment. It must be noted that the presence of the suspended drop will distort the shear field, however the size of the drop is sufficiently small to produce a negligible effect, allowing a steady state far field shear rate $\dot{\gamma}$ to be accurately measured. The simulated shear rate $\dot{\gamma}$ was measured as the mean value of $\partial_z u_y$ over a horizontal layer six sites deep and centred a fixed vertical distance of 25 lattice units from the undeformed drop centre. The shear rate was found to be constant over much of the suspending fluid, and also independent of system and drop size.

Irrotational solenoidal flow in 2D or axisymmetric flow may be described around a *stagnation* point O (where the fluid velocity $\mathbf{u} = 0$), by the motion of the fluid in terms of a stream function ψ [59]. In the case of 2D flow, with axes parallel to the principle axes of the rate of strain tensor G at the stagnation point O,

$$G = \frac{1}{2}h(y^2 - z^2) \tag{6.8}$$

$$\psi(y, z) = hyz \tag{6.9}$$

where h is a constant, making G analogous to $\dot{\gamma}$ as a measurement of the induced flow potential. The streamlines around O are rectangular hyperbolae, all of which asymptote to the two orthogonal directions of the streamline through O. The flow potential was calculated for each of the lattice boundary sites and scaled using the parameter h. A scaling of the flow potential to less than 10% of the mean link density ρ, was used to prevent spurious physical effects from being introduced into the system and creating subcritical burst [56]. The boundary sites were then re–allocated an equilibrium density through Eq. (6.10) to simulate the effect of the flow field.

$$N_i^{eq}(\mathbf{x}, t) = t_i\rho\left[1 + 3\mathbf{u}\mathbf{c}_i + \frac{9}{2}(\mathbf{u}\mathbf{c}_i)^2 - \frac{3}{2}\mathbf{u}^2\right] \tag{6.10}$$

This was achieved by setting the velocity components u of the equilibrium distribution, to the pre–calculated velocity, before the lattice was propagated. Implementation of this method initially affects the system's global mass and momentum, however these parameters are effectively reset to new conserved values after several updates of the lattice. Effectively an inverse mapping of the equilibrium distribution for the lattice edge sites will provide a slightly modified density compared to the

bulk system, however this effect is negligible due to the system size.

Droplet burst in each flow regime was established by increasing the shear flow and allowing the system to equilibrate, then examining the closing configuration of the system by inspection. If drop burst had occured the shear rate was halved, and the previous drop configuration reloaded and the simulation was repeated. This methodology was employed to prevent non–equilibrium effects from inducing drop rupture and allowed the isolation of the shear rate to a degree of accuracy defined by the simulator.

6.5 Drop deformation measurement

The drop deformation measurement was made by assuming that in the low deformation regime, the drop shape may be approximated by an ellipse. This assumption is verified by Halliday and Care [43] who used a grid search optimised fit of a deformed drop and found good agreement compared to a rotated ellipse. The drop symmetry axes (along a and b) of the drop coincide with the principal axes of the inertia tensor $\mathbf{I}$ (leading diagonal terms), with the smallest moment corresponding to the semi-major axis of the ellipsoid. The drop centre of mass was calculated by considering moments about the origin of the lab frame co-ordinates and components

$$I_{\alpha\beta} \equiv \sum_{\alpha\beta} \rho(r^2\delta_{\alpha\beta} - y_\alpha y_\beta) \tag{6.11}$$

of the inertia tensor $\mathbf{I}$ [60] were calculated, where $r = \sqrt{(y^2 + z^2)}$. An orthogonal transformation on $\mathbf{I}$ provides the drop's principle moments of inertia from the

eigenvalues of the calculated secular equation of the matrix. In two dimensions the secular equation has two roots, with two corresponding eigenvectors. The lab frame orientations of the drop semimajor and semiminor axes were then obtained from the direction cosines of the principle axes of **I**. The traceless inertia tensor was evaluated from

$$\mathbf{I} - \frac{1}{2} tr(\mathbf{I}) \mathbf{l}_{22} \tag{6.12}$$

where $\mathbf{l}_{22}$ is the unit two-dimensional matrix. Diagonal elements of Eq. (6.12), are given by the order parameter

$$D \equiv \pm \frac{1}{2}(I_y - I_z) \tag{6.13}$$

where I_y and I_z are the principle moments corresponding to rotation about the semiminor and semimajor axes respectively. As the eccentricity of the drop increases so does the value of the deformation parameter D, for a circular undeformed drop the quantity is zero. The angle between the semimajor axes and the y–axes of the lattice termed α is used to quantify the orientation of the drop to the induced shear flow.

6.6 Shear flow results

Induced drop deformation by a far–field shear was studied for a series of drops of radius $R = 13$ on a 90×60 lattice, unless otherwise stated. In the Figures 6.3...6.6 the progressive deformation of an originally circular suspended red fluid drop is illustrated. The successive frames illustrate the departure of the drop from it's

original circular shape before a critical shear rate $\dot{\gamma}_C$ is reached and the drop bursts. Under moderate shear the drop is seen to assume an ellipsoidal shape and orientate at an angle of $\alpha \approx 45°$ to the direction of the flow. As the shear rate is increased the drop shape is seen to elongate further, until a critical shear rate $\dot{\gamma}_c$ is reached the drop is seen to "neck" and rupture into two separate drops. After the drop has burst the surface tension is seen to restore the circular shape of the smaller drops.

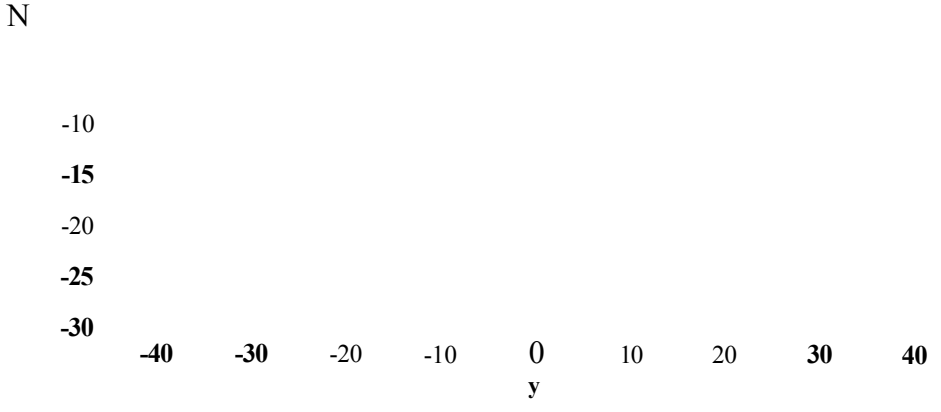

Figure 6.3: Frame (a) $\dot{\gamma} = 3.25 \times 10^{-3}$.

The variation of the drop orientation angle α with the shear rate $\dot{\gamma}$ for a drop with an originally undeformed radius $R = 13$, relaxation parameter $u = 0.91$ and a surface tension $a = 0.0075$ is shown in Figure 6.7. The fit through the data is of the functional form $\alpha = A(\dot{\gamma}_C - \dot{\gamma})^*$, with an optimum fit being found for $A = 3.2$, $K = 0.27$ and $\dot{\gamma}_c = 0.0057$. The angular dependence of α is seen to be linear

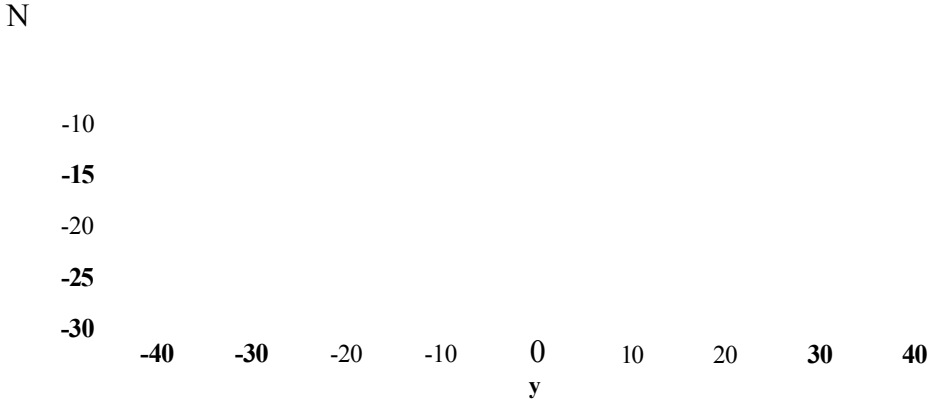

Figure 6.4: Frame (b) 7 = 3.45 x 10 3.

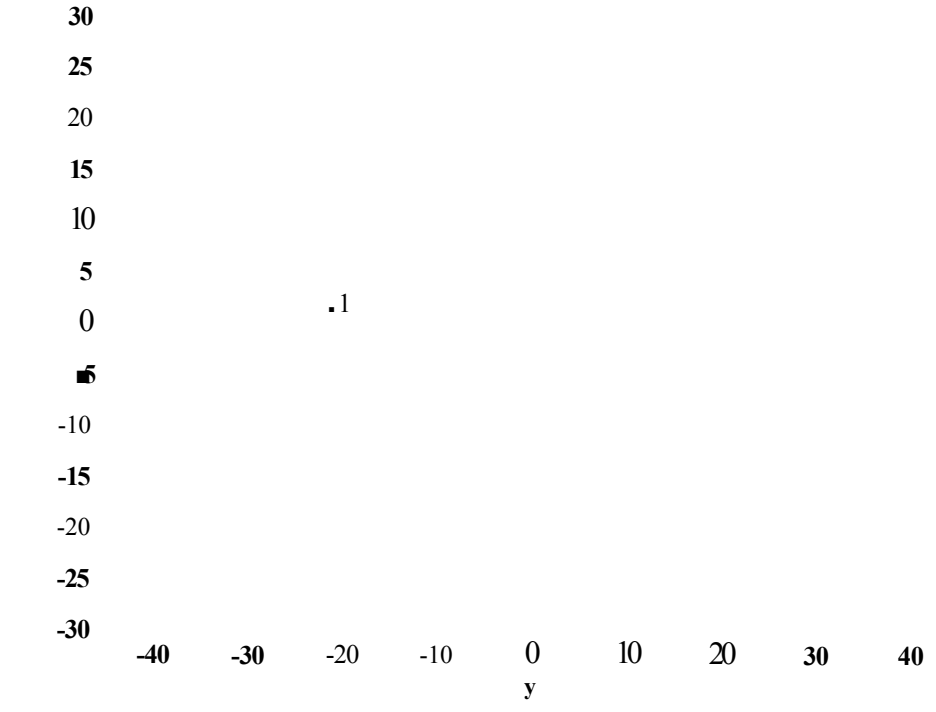

Figure 6.5: Frame (c) 7 = 3.6 x 10 3.

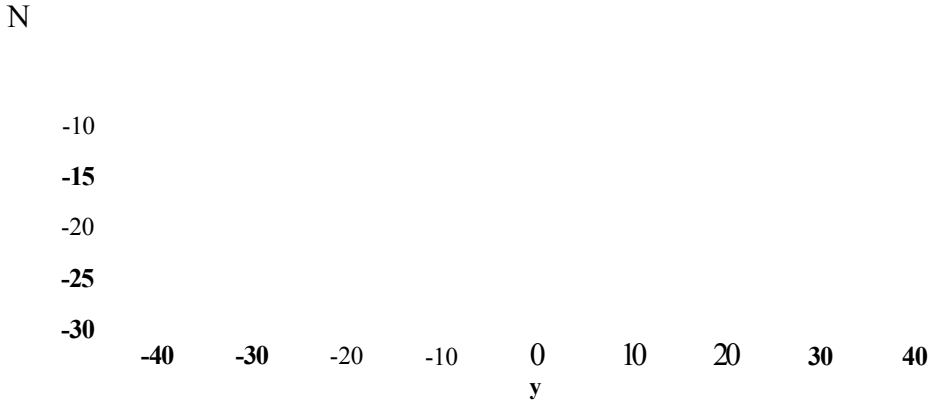

Figure 6.6: Frame (d) 7 = 3.7 x 10 3.

at low shear rates well below the *j c.* In this regime our ellipsoidal approximation to the interface is accurate, however as the deformation increases our approximation to the interface becomes invalid due to the large distortions in the drop shape. The intersection of the fit to the data and the abscissa may be used as an estimate of 7o however the critical shear rate was not measured in this way, but as described earlier by inspection.

Figure 6.8 shows the proportional relationship between the critical shear rate yc and the surface tension parameter a in the range of $0.002 < a < 0.015$. The continuous line represents a linear regression fit to the data with a gradient of 0.496 ± 0.015 with an ordinal intercept of —12.01 x 10~5± 8.049 x 10~5. The relationship between 7Cand the reciprocal radius T is shown in Figure 6.9. A surface tension a = 0.0075

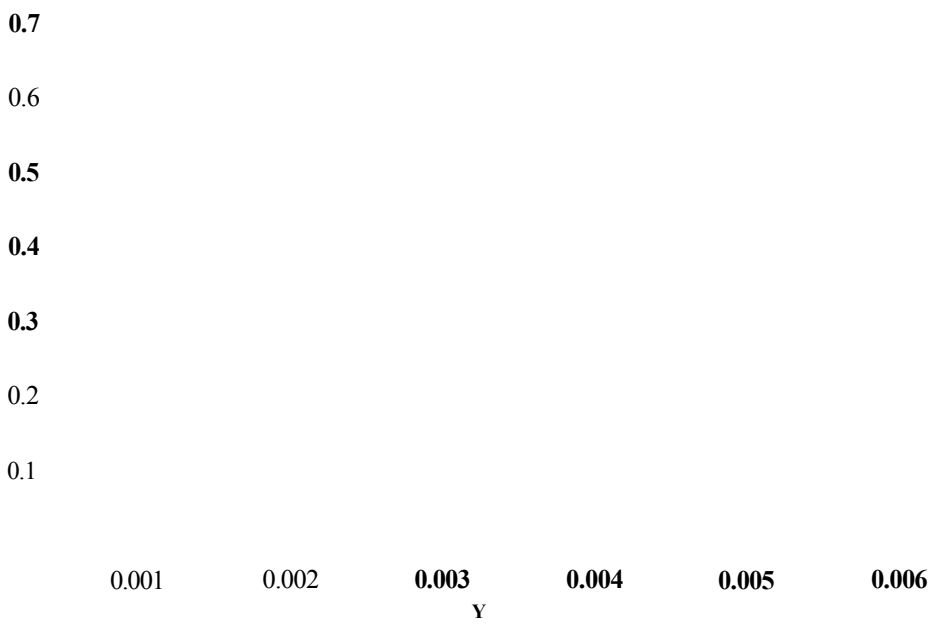

Figure 6.7: Variation of drop orientation angle a with shear rate $\dot{\gamma}$.

was used, whilst the lattice was scaled to keep the same aspect ratio. The data was collected over a drop radius range $10 < R < 20$ on lattice sizes ranging from 76x56 140x92, and with a lattice relaxation parameter $\omega = 0.91$. The continuous line is a linear regression fit to the data with a gradient of 0.051 ± 0.001 with an ordinal intercept of $29.174 \times 10^{-5} \pm 6.337 \times 10^{-5}$.

Figure 6.10 shows the variation of reciprocal critical shear rate $\dot{\gamma}^{-1}$ with the lattice relaxation parameter ω at $a \rightarrow 0.0075$. A range of equal red and blue fluid BGK relaxation parameters in the range $0.7 < \omega < 1.4$ were investigated, maintaining the viscosity ratio $\beta = 1$. The dotted line represents a fit through the centre of the data with a gradient / intercept ratio of $m/c = -0.5$ as predicted by our analysis, a linear regression fit to the data (solid line) obtains a gradient / intercept ratio of

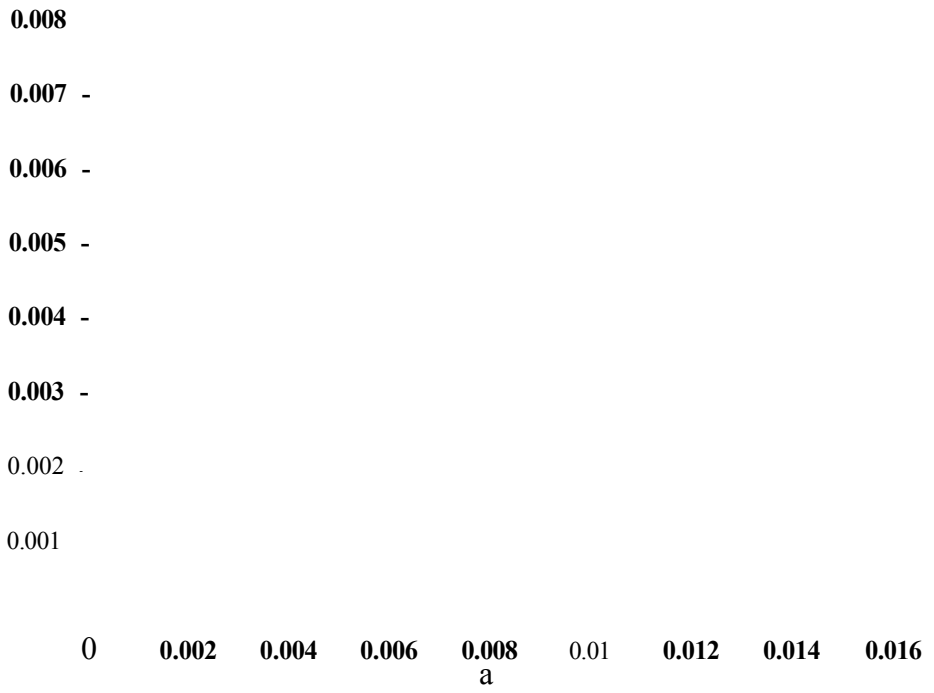

Figure 6.8: Variation in % with interface perturbation parameter α. The straight line represents a least squares fit to the data.

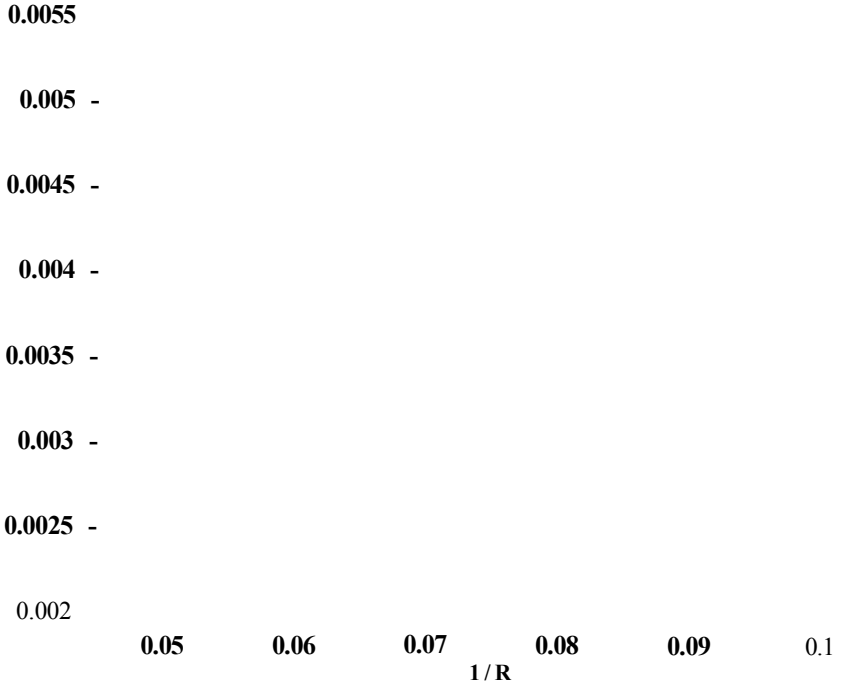

Figure 6.9: Dependence of τ_{22} on reciprocal drop radius $-h$. The straight line represents a least squares fit to the data.

$m/c = -0.425$. The difference between the measured and theoretical values of the gradient / intercept ratio may be explained by careful consideration of Figure 4.15. We see from this figure that the macroscopic surface tension Σ takes the general form

$$\Sigma = \frac{m\sigma}{\omega} + \sigma c \tag{6.14}$$

where the gradient is given by m and c is the ordinal intercept. Re-arranging Eq. (6.14) and letting $k' = \frac{c}{m}$ we may write

$$\Sigma = m\sigma \left[\frac{1 + \omega k'}{\omega}\right] \tag{6.15}$$

letting

$$\omega' = \left[\frac{\omega}{1 + k'\omega}\right] \tag{6.16}$$

gives the surface tension the functional form

$$\Sigma = \frac{m\sigma}{\omega'} \tag{6.17}$$

where ω' may be termed an effective relation parameter. The simplification used for $\Sigma \sim \sigma/\omega$ in Eq. (6.5), compared with the measured form in Eq. (6.17) may be used to explain the differences found between the measured and theoretical ratios. Additionally, Taylor's theoretical prediction of burst Eq. (6.2), is also approximate.

The streamlines around the drop are shown in Figure 6.11 and a stable shear is seen in the drop far field. The decreasing distance between streamlines at the top and bottom of the lattice, indicates the associated increase in velocity and agrees well with theory. The presence of the drop is seen to induce a small distortion to the velocity field, indicated by the oscillation in the streamlines towards the centre of the lattice.

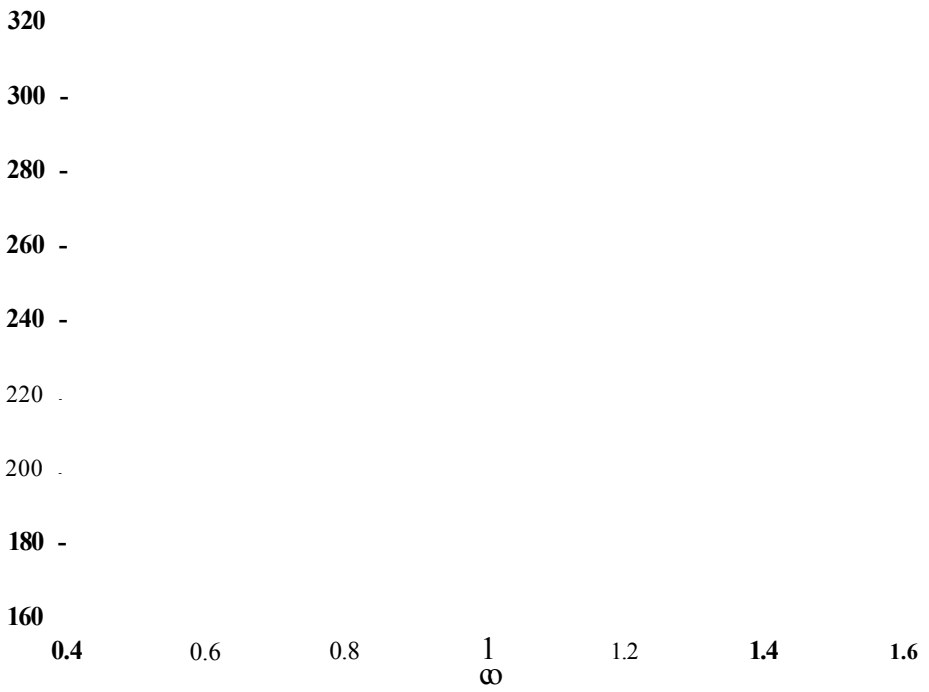

Figure 6.10: Dependence of $1/\%$ with BGK relaxation parameter u. The dotted line represents a fit through the centre of the data with a gradient / intercept ratio of $m/c = -0.5$ and the solid line represents a linear regression fit to the data with a gradient / intercept ratio of $m/c = -0.425$.

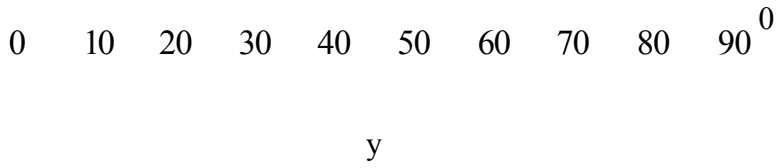

Figure 6.11: Streamlines around a moderately deformed drop with simulation parameters of $a = 0.0075$, $\omega = 0.91$ and $R = 13$.

6.7 Solenoidal irrotational flow results

Figures 6.12...6.17 illustrates the progressive deformation of an originally circular suspended red fluid drop under a solenoidal irrotational flow field. The successive frames illustrate the departure of the drop from it's original shape until burst. Drops with an undeformed radius $R = 13$ and a surface tension parameter $\sigma = 0.0075$ and relaxation parameter $\omega = 0.91$ were evolved on a 120×60 lattice, unless otherwise stated. The flow field causes the drops to deform into an elliptical shape with the drop semi–major axes parallel with the lattice y direction. As the magnitude of the flow field is increased the drop is seen to compress further in the z direction whilst elongating in the y direction, until the drop necks and finally bursts. Once the drop has burst into two separate drops of approximately equal size, the surface tension of the smaller drops drives their shape to a more circular configuration. Figure 6.17 shows the closing configuration of the drops as they approach the simulation box walls at a simulation interval of 20000 steps after burst. The drops have not had time to fully return to a circular shape and as they are driven to the boundaries they distort. We note with a simulation box on infinite length, as the simulation advances the drops would regain their circular shape, whilst drifting apart indefinitely.

The linear relationship between the critical solenodial flow potential G_c with surface tension parameter σ in the range $0.005 \leq \sigma \leq 0.015$ is shown in Figure 6.18. G_c is noted to be analagous to the critical shear rate $\dot{\gamma}_c$, used in the simple shear flow simulations. The continuous line is a linear regression fit to the data with a gradient of $0.057 \pm 2.234 \times 10^{-4}$ with an ordinal intercept of $5.2 \times 10^{-5} \pm 2.369 \times 10^{-6}$.

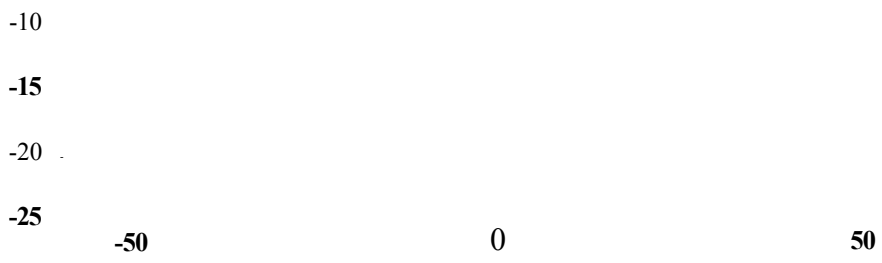

Figure 6.12: Frame (a) G = 3.55 x 10 4.

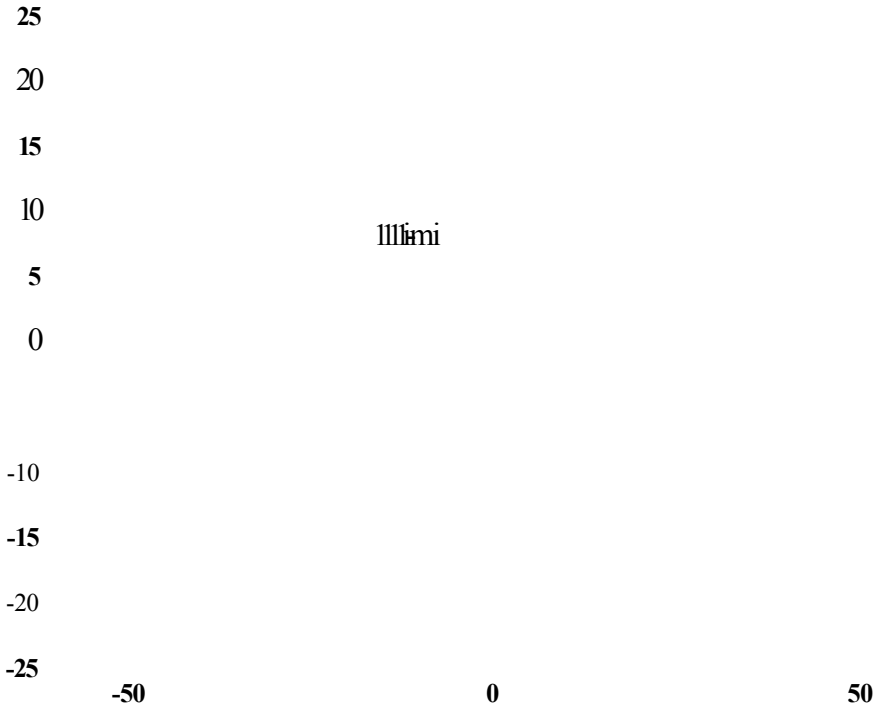

Figure 6.13: Frame (b) G — 3.9 x 10-4.

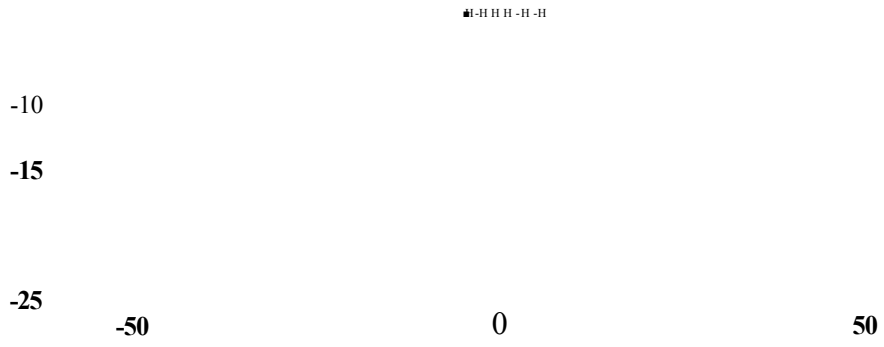

Figure 6.14: Frame (c) G = 4.45 x 10 4.

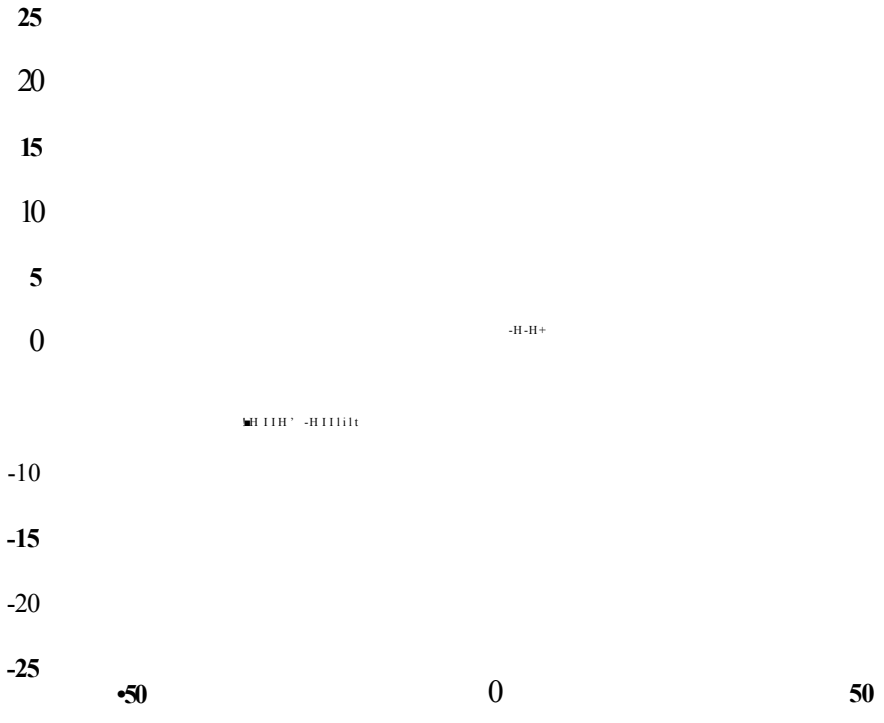

Figure 6.15: Frame (d) G = 4.6 x 10 4.

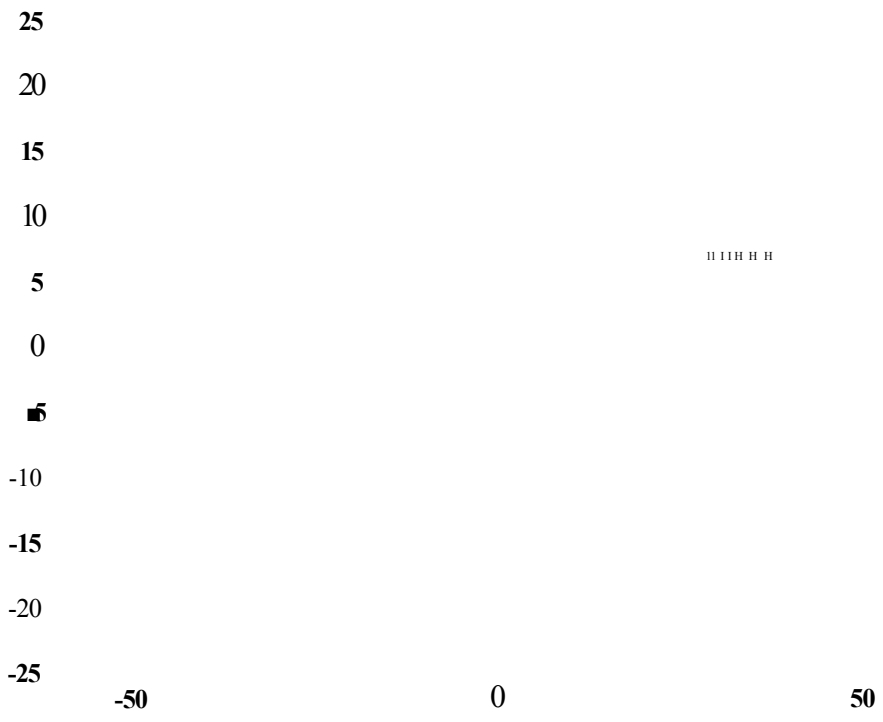

Figure 6.16: Frame (e) G = 4.8 x 10 4.

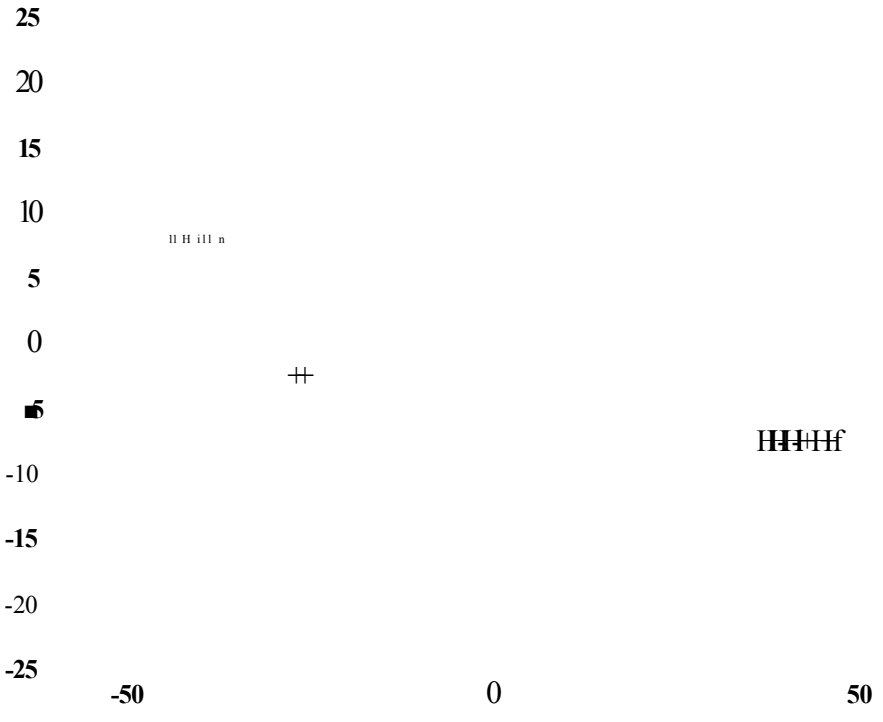

Figure 6.17: Frame (f) G = 4.8 x 10 4.

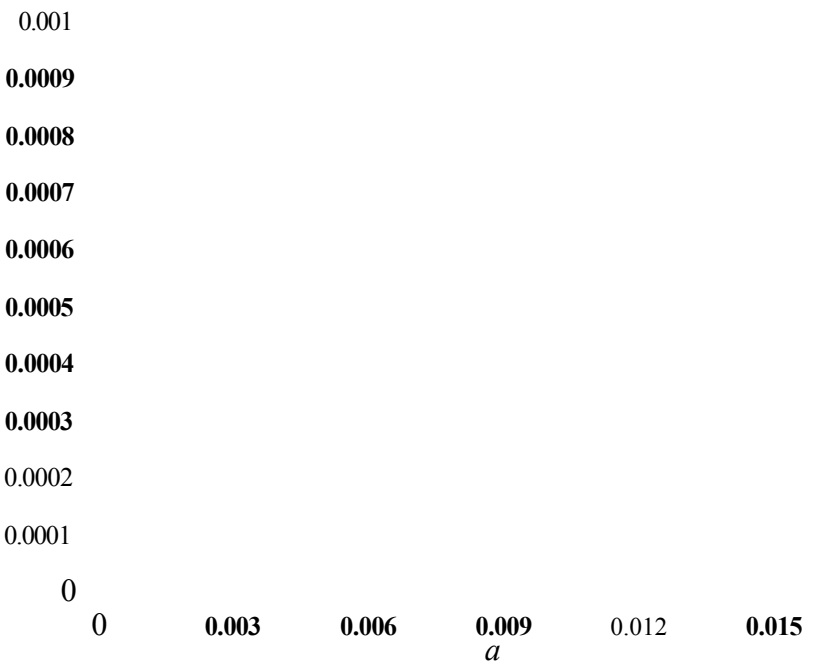

Figure 6.18: Variation in Gc with interface perturbation parameter a. The straight line represents a least squares fit to the data.

Figure 6.19 shows the variation of critical solenodial flow potential Gc with reciprocal radius A surface tension parameter of a — 0.0075 was used, whilst the lattice was scaled to keep the same aspect ratio. The data was collected over a drop radius range $10 < R < 20$ on lattice sizes from 92 x 46 —» 186 x 94. The continuous line is a linear regression fit to the data with a gradient of 6.570 x 10-3 ± 9.942 x 10-5 with an ordinal intercept of —1.981 x 10~5 dt 7.212 x 10~6.

The variation in reciprocal critical shear rate with the lattice relaxation parameter uj at $a = 0.0075$ is shown in Figure 6.20. A range of equal red and blue fluid BGK relaxation parameters in the range $0.7 < u < 1.5$ were investigated, maintaining the viscosity ratio β — 1. The continuous line represents a fit through the centre of the data with a gradient / intercept ratio of $m/c = -0.5$ as predicted by our analysis,

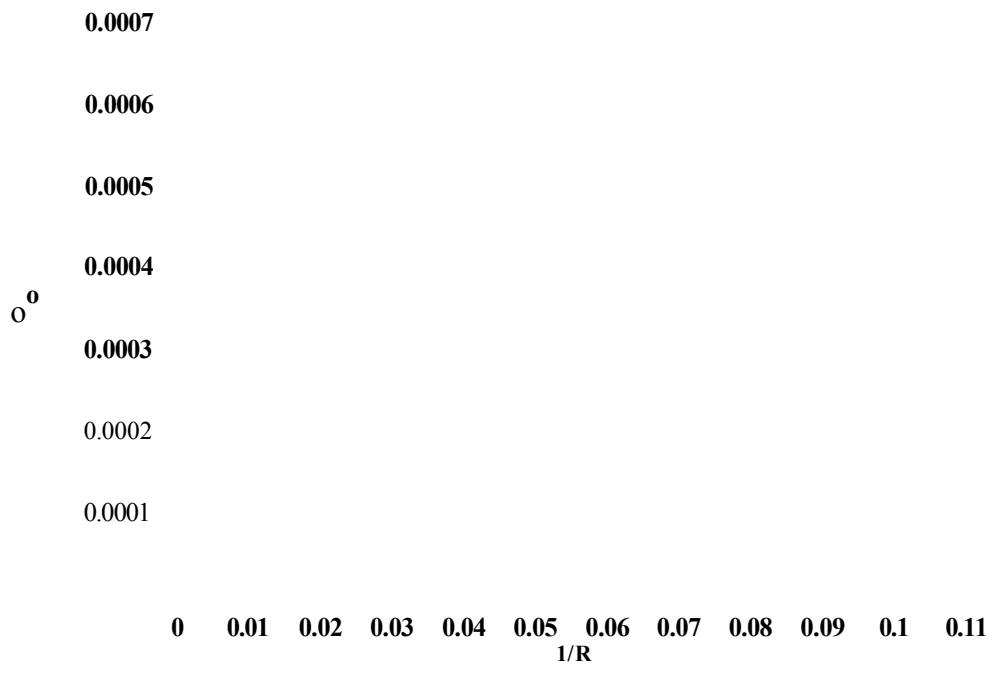

Figure 6.19: Variation in Gc with reciprocal drop radius The straight line represents a least squares fit to the data.

the dotted line represents a linear regression fit to the data and obtains a gradient / intercept ratio of m/c — —0.413.

Figure 6.21 depicts the streamlines around the elliptically deformed drop of Figure 6.13 and shows good agreement with theory in the drop far-field.

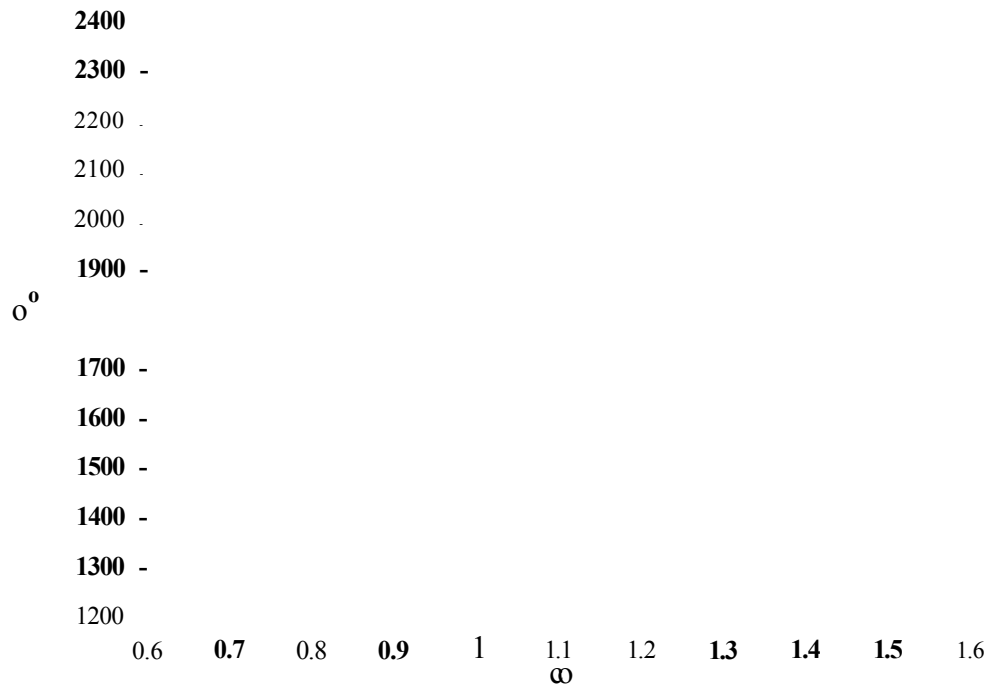

Figure 6.20: Variation of $1/Gc$ with BGK relaxation parameter $u_;$. The continuous line represents a fit through the centre of the data with a gradient / intercept ratio of mjc — —0.5 and the dotted line represents a linear regression fit to the data and obtains a gradient / intercept ratio of mjc — —0.413.

Figure 6.21: Streamlines around a moderately deformed drop (see Figure 6.13) with simulation parameters $a = 0.0075$, $u = 0.91$ and $R = 13$.

6.8 Conclusions

In this chapter our model has been used to simulate the deformation and burst of neutrally buoyant immiscible fluid drops of different radii R, surface tension σ and BGK relaxation parameter ω. The model allows the simulator to set the kinematic viscosity ν and the viscosity ratio ϕ, and adjust the macroscopic surface tension parameter Σ through σ. We may implement with relative ease, different boundary conditions in order to simulate simple shear flows and capture the correct hydrodynamics of ruptured liquid drops. As predicted by theory drop burst occurs at higher shear rates, than analogous irrotational solenoidal flow fields in our simulations.

Under shear flow drops exhibit qualitatively the correct deformation with the semimajor axis orientating at 45^0 to the induced flow. The dependence of measured critical shear rate $\dot{\gamma}_c$ for drop burst upon all independent simulation parameters is in good agreement with hydrodynamic theory. The proportional dependence of the critical shear rate $\dot{\gamma}_c$ upon the surface tension parameter σ and reciprocal drop radius $\frac{1}{R}$ as predicted by theory is found. However an extra complexity in the relation between the reciprocal critical shear rate $\dot{\gamma}_c$ and relaxation parameter ω, beyond $O(1)$ in velocity is seen.

Under irrotational solenoidal flow, drops again exhibit qualitatively correct deformation, with the semimajor axis parallel to the horizontal y axis. Again a linear relation is found between the flow field potential G_c and σ and $\frac{1}{R}$. A similar relation between the reciprocal critical shear $\frac{1}{G_c}$ and the relaxation parameter ω, is found for

the irrotational solenoidal flow field compared with the simple shear simulations.

The dependence of reciprocal critical shear rate upon BGK relaxation parameter ω, for both types of flow suggests that the relaxation parameter may be analysed in terms of an effective relaxation parameter of the form $\omega' = p\,\omega$. However, due to the excellent agreement between the critical shear rate and the other simulation parameters such a line of inquiry would require cautious investigation.

Chapter 7

Conclusions and Future Work

7.1 Summary

In this thesis, we have developed theory which is used to calculate the surface tension induced in static plane interfaces in a two component LBGK fluid. This analysis is based upon the examination of the microscopic collisions in the model and the obtained results compared well with simulation measurements. We extend our analysis to curved interfaces and propose a scheme for incorporating the influence of the interfacial microcurrent, which is based upon arguments of lattice symmetry. We find good agreement between theory and simulation results, based upon the microcurrent stream function and the surface tension calculated from the pressure tensor and Laplace law. These results reveal that the surface tension in our model is anisotropic, and dependent upon lattice link orientation, which we proceed to

investigate further

The results of chapter 5 convincingly prove that the transmission of tangential stress by the interface separating the immiscible fluid components shows comprehensive agreement with theory. The examination of normal stress transmission in two dimensional by substitution of the tangential stress components, has allowed us to develop a Fourier based interface investigation technique. By making no predetermined assumption about the interface shape, we are able to base our analysis solely upon the discrete singular nature of the interface. This has allowed a quantitative analysis of the anisotropy of macroscopic drop surface tension to be made, for static and moderately deformed drops. It has also facilitated the development of a new interface perturbation technique with improved macroscopic surface tension isotropy, and a reduced microcurrent.

Finally, we describe in chapter 6 the results of an application of our model to the deformation and burst of neutrally buoyant drops subjected to simple external flows. Under simple shear and irrotational flows, drops are seen to exhibit qualitatively the correct deformation and orientation to the external flows. The relationship between the measured critical shear rates for drop burst upon all simulation parameters is in good agreement with hydrodynamic theory. The dependence of reciprocal critical shear rate for drop burst upon BGK relaxation parameter ω for both types of flow suggests that the model may need to be analysed in terms of an effective relaxation parameter of the form $\omega' = p\,\omega$. However, the excellent agreement found between the other simulation parameters would restrict this line of investigation and effect

our calculated value of macroscopic surface tension $\Sigma \sim \frac{\sigma}{\omega}$.

7.2 Future work

It is perhaps the case that by liberating the interface from the lattice we may increase the isotropy of both drop shape and surface tension. Examination of the interface geometry for both static and deformed drops shows clear evidence of preferential interface orientation parallel to lattice link directions. This may we suggest be attributed to the highly singular nature of the drop interface. However the interface may be liberated from the underlying lattice, by performing a modification to the interfacial link densities after they have been re–allocated to the lattice via the re–colour procedure. The idea behind this modification is probably best explained through the use of the following example. Consider the interfacial site depicted in Figure 7.1, we see the allocation of the red density (red circles) at a particular site and the superposing of the calculated colour field $\mathbf{f}(\mathbf{x}, t)$ and colour flux $\mathbf{q}(\mathbf{x}, t)$, for this particular allocation. The colour flux is observed to be below the colour field, and requires rotation in the anti–clockwise direction in order to lie exactly along the colour field direction $\mathbf{f}(\mathbf{x}, t)$ to maximise the colour flux along the colour field direction.

In this particular case the first lattice link to be allocated red density was the $i = 3$ link (first link to be allocated in the precalculated re–colour hierarchy). Starting from this link we may move clockwise to identify a *source* link, the source link is

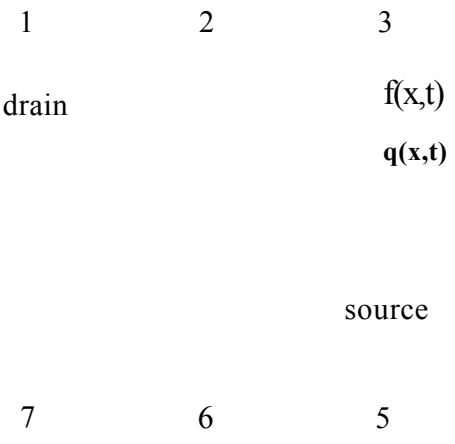

Figure 7.1: Schematic representation of the identification of *source* and *drain* links

defined as the last link in a clockwise direction from $i = 3$ (in this example) which contains some red density, the source link in our example is link $i = 5$. This process may be repeated in the anti-clockwise direction to find the first link which does not contain a completely full allocation of red density, this link is then termed the *drain.* In this particular example link $i = 2$ is completely full (filled circle) so the next link to be allocated red density in this direction is link $i — 1$ (unfilled circle). This scheme may simply be reversed to locate a source and drain link for cases where the colour flux angle is greater than the colour angle. The physical effect of interface liberation on the isotropy of the drop may be examined through the harmonics of our developed Fourier fitting procedure to the interface. An improvement in the isotropy of the drop shape would be evident by a reduction in magnitude of higher order harmonic components of our discrete approximation (the fit) to the drop interface. We note as the fit to the interface is performed in two parts (firstly a fit to the y then z co-ordinate data), consideration of the harmonics of the y and z co-ordinates fits separately would be required. By considering the sum of the Fourier components

$F_n = \sqrt{(a_n^2 + b_n^2)}$ against n the harmonic number, we may examine the magnitude of the harmonics for systems with and without this modification and thus the associated improvement in isotropy.

Our Fourier based interface investigation technique makes no predetermined assumptions about the immiscible interface, thus, it may be employed to investigate other interface generation models such as the Shan and Chen type interface [32]. We suggest that a comparison of our improved isotropy interface (of chapter 5) with other models, by measuring the magnitude of the microcurrent and the isotropy of the surface tension would allow questions relating to the hydrodynamic boundary conditions of immiscible lattice Boltzmann models to be addressed. This would allow the identification of the most hydrodynamic interface generating technique.

An important and obvious extension to this research is the expansion of our model to three dimensions $3D$. This will allow the effect of the second radius of curvature upon the burst process to be fully assessed in the case of induced drop burst, and allow the simulation of real world applications. The BGK model may be easily implemented in three dimensions using the $D3Q19$ scheme [23], which is based upon a cubic lattice. Interface generation in three dimensions would require the development of a modified interface perturbation scheme, based upon the discretisation of a unit sphere. The discretisation may be made to any required limit of accuracy, and such schemes have already been implemented in three dimensions for LG simulations [36]. We note however, the computational expense of moving to three dimensions will probably require the use of parallel computation, in order to simulate systems large enough to

perform realistic simulations of physical processes. Parallel development is facilitated by the inherently parallel nature of the LB scheme, and the current development of lattice models on massively parallel machines [61]. We note that a parallel model may be easily developed from our existing codes and quickly parallelised for computation on a shared memory computer, such as the Silicon Graphics Origin2000. By using the fork–join parallelisation technique employed by OpenMP [62], compiler directives may be simply introduced into the code to parallelise individual routines and loops.

The development of a three dimensional model would be further facilitated by employing the Shan and Chen interface technique as this scheme requires no re–colouring technique to be devised and has been shown recently [51] to produce a more hydrodynamic interface. A further extension may be made to allow the simulation of fluid components with differing densities. This may be achieved by following Shan and Chen [32] (see chapter 2), and introducing a scaling factor determining the molecular mass of a particular fluid component.

The investigation of new hydrodynamic models such as immiscible Dissipative Particle Dynamics techniques [47], that allow the examination of immiscible fluids at the same mesoscopic length scales as LB models also warrant further examination. This technique allows the modelling of complex multi–component fluids and as the fluid particles are unrestricted to lie upon a discrete lattice, the transition from two dimensions to three dimensions is greatly simplified. As the models are *off-lattice* they will not suffer as greatly from problems related to anisotropy.

7.3 Conclusion

In conclusion we have developed a new two component fluid model based upon a D2Q9 lattice BGK scheme. The model has been used to simulate the deformation and burst of neutrally buoyant immiscible fluid drops of different radii R, surface tension σ and BGK relaxation parameter ω. The model allows the simulator to set the kinematic viscosity ν and the viscosity ratio ϕ, and adjust the macroscopic surface tension parameter Σ through σ. Our model allows the implementation, with relative ease of a range of boundary conditions in order to simulate simple shear flows and solid boundaries. The potential for further development of this technique to simulate industrially relevant systems is wide ranging. This work has shown for the first time that hydrodynamic stresses are transmitted correctly by an immiscible Lattice Boltzmann BGK interface and this will hopefully inspire greater interest in the development of this type of fluid modelling technique in both academia and industry.

Bibliography

[1] A. K. Gunstensen, D.H. Rothman, S. Zaleski and G. Zanetti, *Phys. Rev. A*, **43** (8) (1991) pp.4320–4327.

[2] M.B. Abbot and D.R. Basco, *Computational Fluid Dynamics : An Introduction for Engineers*, Longman Press (1989).

[3] B. Lafaurie, C. Nardone, R. Scardovelli, S. Zaleski and G. Zanetti, *J. Comp. Phys.*, **113** (3-4) (1994) pp.134–147.

[4] S. Zaleski, J. Li and S.Succi, *Phys. Rev. Lett.*, **75** (2) (1995) pp.244–247.

[5] M.P.Allen and D.J. Tildesley, *Computer Simulation of Liquids*, Claredon Press, Oxford Science Publications (1987).

[6] J. Goodfellow, *Molecular Dynamics*, Macmillan Press (1991).

[7] U. Frisch, D. d'Humieres, B. Hasslacher, P. Lallemand, Y. Pomeau and J.P.Rivet, *Complex Systems*, **1** (1987) pp.649–707 and references therein.

[8] D. H. Rothman and S. Zaleski, *Rev. Mod. Phys.* **52** (1994) pp.1417–.

[9] R. Benzi, S. Succi and M. Vergassola, *Phys. Reports* **22** (3) (1992) pp.145–197.

[10] Y.H. Qian, S. Succi and S.A. Orszag, *Ann. Rev. Comp. Phys.* **3** (1995) pp.195–242.

[11] S. Chen and G.D. Doolen, *Ann. Rev. Fluid Mech.* **30** (1998) pp.329–364.

[12] J. Hardy, Y. Pomeau and O. de Pazzis, *J. Math. Phys.*, **14** (1973) pp.1746–.

[13] J. Hardy, O. de Pazzis and Y. Pomeau, *Phys. Rev. A*, **13** (1976) pp.1949–.

[14] L. D. Landau and E.M. Lifshitz, Fluid Mechanics, Pergamon Press (1966).

[15] D. d'Humieres, P. Lallemand and U. Frisch, *Europhys. Lett.*, **56** (1986) pp.1505–

[16] S. Wolfram, *J. Stat. Phys.*, **45** (3/4) (1986) pp.471–525.

[17] R. Cornubert, D. d'Humieres and D. Levermore, *Physica D*, **47** (1991) pp.241–.

[18] D. d'Humieres, P. Lallemand and G. Searby, *Complex Systems*, **1** (1987) pp.633–.

[19] G. McNamara and G. Zanetti, *Phys. Rev. Lett.*, **61** (20) (1988) 2332–2335.

[20] F. Higuera and J. Jimenez, *Europhys. Lett.*, **9** (7) (1989) pp.663–.

[21] F. Higuera, S. Succi and R. Benzi, *Europhys. Lett.*, **9** (4) (1989) pp.345–.

[22] P. Bhatnagar, P.E. Gross and M.K. Krook, *Phys. Rev.*, **94** (1954) pp.511–.

[23] Y. H. Qian, D. d'Humieres and P. Lallemand, *Europhys. Lett.*, **17** (6) (1992) pp.479–484.

[24] H. Chen, S. Chen and W.H. Matthaeus, *Phys. Rev. A*, **45** (8) (1992) pp.R5339–R5342.

[25] S. Chapman and T.Cowling, *The Mathematical Theory of Non-Uniform Gases*, Cambridge University Press (1970).

[26] D. H. Rothman and J.M. Keller, *J. Stat. Phys.*, **52** (3-4) (1988) pp.1119–1127.

[27] C. Adler, D. d'Humieres and D.H. Rothman, *J. de Physique I*, **4**, (1) (1994) 29–46.

[28] S. Chen, G.D. Doolen, K. Eggert, D. Grunau and Y.E. Loh, *Phys. Rev. A*, **43** (12) (1994) pp. 7053–7056

[29] A. K. Gunstensen, *Lattice Boltzmann Studies of Multiphase Flow Through Porous Media* Thesis, MIT (1992).

[30] J.S. Rowlinson and B. Widom, Molecular Theory of Capillarity, Oxford Publications (1989).

[31] D. Grunau, S.Chen and K.Eggot, *Phys. Fluids A* (10) (1993) pp2557–2562.

[32] X. Shan and H.Chen, *Phys. Rev. E* **47** (3) (1993) pp.1815–1819.

[33] M.R. Swift, W. R. Osborn and J.M. Yeomans, *Phys. Rev. Lett* **75** (1995) pp.830–833.

[34] E. Orlandini, G. Gonnella and J.M. Yeomans, *Physica A* **240** (1-2) (1997) pp.277–285.

[35] E. Orlandini, M.R. Swift and J.M. Yeomans, *Europhys. Lett.*, **32** (1995) pp.463–468.

[36] J.F.Olson and D.H.Rothman, *J. Stat. Phys.* **81** (1/2) (1995) pp.199–222.

[37] N. Martys and H Chen, *Phys. Rev. E* **53** (1) (1996) pp.743–750.

[38] D.R. Noble, S.Y. Chen, J.G. Georgiadis and R.O. Buckius, *Phys. of Fluids* **7**, (1995), (1), pp.203–209.

[39] X.W. Shan and G. Doolen, *Phys. Rev. E* **54** (4) (1996) pp.3614-3620.

[40] X.W. Shan and H.D. Chen, *Phys. Rev. E* **49** (4) (1994) pp.2941-2948.

[41] F.J. Alexander, S. Chen and D.W. Grunau, *Phys. Rev. B* **48** (1) (1993) pp.634–637.

[42] G. Gonnella, E. Orlandini and J.M. Yeomans, *Phys. Rev. Lett.* **78** (9) (1997), pp.1695–1698.

[43] I. Halliday and C.M. Care, *Phys. Rev. E*, **53** (3) (1995) pp.1602–.

[44] O. Behrend, R. Harris and P.B. Warren, *Phys. Rev. E*, **50** (6) (1994) 4586–4595.

[45] A.J. Wagner and J.M. Yeomans, *J. Mod. Phys. C*, **8** (4) (1997) pp.773–782.

[46] M. Schelkle and A. Frohn, *J. Aerosol Sci.* **26** (1) (1995) pp.S145–S146.

[47] P.V. Coveney and K.E Novik, *Phys. Rev. E*, **54** (5) (1996) pp.5134–5141.

[48] P.J. Hoogerbrugge and J.M.V.A. Koelman, *Europhys. Lett.*, **19** (4) (1992) pp.155–.

[49] S. Hou, Q. Zou, S. Chen, G. Doolen and A.C. Cogley, *J. Comp. Phys.*, **118** (6) (1995) pp.329–347.

[50] M. R. Spiegel, Vector analysis and an introduction to Tensor analysis, Schaum's Outline Series, McGraw–Hill (1959).

[51] S. Hou, X. Shan, Q. Zou, G.D. Doolen and W.E. Soll, *J. Comp. Phys.*, **138** (2) (1997) pp.695–713.

[52] G.I. Taylor, *Proc. Royal. Soc. A* **138** (1932) pp.41–48.

[53] F.D. Rumscheidt and S.G. Mason, *J. Coll. Sci.* **16** (1961) pp.238–261.

[54] S.J. Richardson, *J. Fluid Mech.* **33** (1968) pp.476–493.

[55] J.D. Buckmaster and J.E. Flaherty, *J. Fluid Mech.* **60** (1973) pp.625–639.

[56] J.M. Rallison, *Ann. Rev. Fluid Mech.* **16** (1984) pp.45–66.

[57] H.A. Stone, *Ann. Rev. Fluid Mech.* **26** (1994) pp.65–102.

[58] J.M. Rallison, *J. Fluid Mech.* **109** (1981) pp.465–482.

[59] G.K. Batchelor, *An Introduction to fluid dynamics*, Cambridge University Press, (1973).

[60] H. Goldstein, *Classical Mechanics*, Addision–Wesley Publisbing Company Inc. Reading MA, (1966).

[61] D. Talia, "Cellular Automata thrive on parallel machines", *Scientific Computing World*, **42** (1988) pp.21–22.

[62] http://www.OpenMP.org

Appendix A

A.1 Lattice link vector index

i	c_{ix}	c_{iy}	c_i^2	θ_i	$cos(2\theta_i)$
1	-1	1	2	135	0
2	0	1	1	90	-1
3	1	1	2	45	0
4	1	0	1	0	1
5	1	-1	2	-45	0
6	0	-1	1	-90	-1
7	-1	-1	2	-135	0
8	-1	0	1	180	1
9 (rest)	NA	NA	0	NA	NA

Figure A.1: Lattice link vector index, length and orientation

A.2 Colour Field Hierarchy Table

Hierarchy Order	1	2	3	4	5	6	7	8	9
Segment *1*	3	4	5	2	9	6	1	8	7
Segment *2*	3	4	2	5	9	1	6	8	7
Segment *3*	3	2	4	1	9	5	8	6	7
Segment *4*	3	2	1	4	9	8	5	6	7
Segment *5*	1	2	3	8	9	4	7	6	5
Segment *6*	1	2	8	3	9	7	4	6	5
Segment *7*	1	8	2	7	9	3	6	4	5
Segment *8*	1	8	7	2	9	6	3	4	5
Segment *9*	7	8	1	6	9	2	5	4	3
Segment *10*	7	8	6	1	9	5	2	4	3
Segment *11*	7	6	8	5	9	1	4	2	3
Segment *12*	7	6	5	8	9	4	1	2	3
Segment *13*	5	6	7	4	9	8	3	2	1
Segment *14*	5	6	4	7	9	3	8	2	1
Segment *15*	5	4	6	3	9	7	2	8	1
Segment *16*	5	4	3	6	9	2	7	8	1

Figure A.2: Colour Field Hierarchy Table

The colour field hierarchy table contains the order which links are allocated red density in the *re-colour* procedure. Consider the allocation required when the colour field intersects Segment 2. Red density is firstly allocated to link $i = 3$, then $i = 4$, $i = 2$ and so on down the hierarchy, the final link to be allocated is diametrically opposite the first link $i = 7$. Note the stationary link $i = 9$ is chosen to lie in the middle of the hierarchy.

Induced burst of fluid drops in a two-component lattice Bhatnager-Gross-Krook fluid

I. Halliday and C. M. Care
Division of Applied Physics and Materials Research Institute, Sheffield Hallam University, Pond Street, Sheffield S1 1WB, United Kingdom

S. Thompson and D. White
Materials Research Institute, Sheffield Hallam University, Pond Street, Sheffield S1 1WB, United Kingdom
(Received 20 February 1996)

We describe a two-dimensional simulation of burst in neutrally buoyant drops subject to shear using a two-component, two-speed lattice Bhatnager-Gross-Krook (BGK) fluid. Measuring the dependence of critical shear rate for drop rupture on flow parameters, our results validate the method over a range of simulation variables. The model's interfacial tension parameter σ, undeformed drop radius, and BGK relaxation parameter ω are all found to have the correct influence upon the process of burst required by simple hydrodynamic theory. Within the model, the macroscopic surface tension and fluid viscosity are coupled; however, this does not limit the application of the technique. [S1063-651X(96)11008-4]

PACS number(s): 47.55.Dz, 05.50.+q

The mechanical formation of emulsions from multicomponent immiscible fluid mixtures is a complex problem of considerable technological and theoretical interest. Advection of suspended drops and marked departures in shape before burst reduce the utility of traditional numerical methods. However, competitor lattice Boltzmann (LB) techniques allow the simulator to calculate the flow of a viscous incompressible fluid by solving the dynamics of colliding and propagating prototype particles on a regular lattice using a Boltzmann type equation [1]. The simplest and probably most tractable lattice Boltzmann variant derives its inspiration from the work of Bhatnagar, Gross, and Krook on the Boltzmann equation of statistical physics [2]. The appropriately named lattice BGK method [3–5], then, incorporates both isotropy and Galilean invariance directly into a model that has the advantage of simple collision step and that has been shown to recover single phase hydrodynamics [3–5].

Two-dimensional lattice Boltzmann *immiscible* lattice gas (LBILG) techniques [6] have been applied to droplets under shear to demonstrate qualitatively correct steady-state interfacial hydrodynamic boundary conditions [7] and, in three dimensions, to sheared phase separation [8]. The growing literature on this method has been recently reviewed by Rothmann and Zaleski [9].

Here we report on simulations using a LBILG BGK algorithm enhanced to contain different species and an interface, with advantages similar to the model in [7], applying the method to the simulation of burst in an infinite, equispaced line of neutrally buoyant *red* fluid component drops suspended along the x axis, within a *blue* component, the flow in the far field of which is a uniform shear of rate $\dot{\gamma}$ [10].

As we have commented, an attractive feature of the BGK approach is its simple collision step with a scalar collision operator ω controlling the simulated fluid kinematic viscosity through [4]

$$\nu=\frac{1}{6}\left[\frac{2}{\omega}-1\right]. \tag{1}$$

Designated D2Q9 [4], our lattice BGK algorithm uses a square lattice with links $\mathbf{c}_i$ to both nearest and next-nearest neighbors. As such we use a two-speed lattice, the multispeed nature of which requires careful consideration when incorporating algorithmic extensions designed to separate red and blue densities $R_i(\mathbf{x},t)$, $B_i(\mathbf{x},t)$ [6]. As a measure of local gradient in the color distribution, a local "color field" $\mathbf{f}(\mathbf{x},t)$ is calculated using direction-weighted contributions of chromatic link densities from $\mathbf{f}(\mathbf{x},t)=\Sigma_{ij}[R_j(\mathbf{x}+\mathbf{c}_i,t)-B_j(\mathbf{x}+\mathbf{c}_i,t)]\mathbf{c}_i$ [6,7]. The BGK collision step redistributes achromatic density $N_i(\mathbf{x},t)\equiv R_i(\mathbf{x},t)+B_i(\mathbf{x},t)$ to links according to the local flow conditions. The tendency of an equivalent automaton color segregation algorithm [11] to accumulate (denude) density on links perpendicular (parallel) to an interface line is introduced at this stage, after Gunstensen *et al.* [6], by applying perturbations to link densities with reference to the direction of $\mathbf{f}(\mathbf{x},t)$, the amplitude of these perturbations having a linear dependence on a "surface tension" parameter σ [7]. However, it should be noted that Gunstensen *et al.* use a linearized lattice Boltzmann scheme rather than the BGK method described in this work. Color is allocated to collided, perturbed link densities in that distribution which maximizes the work done by a color flux in the direction of the color field [6,7]. Essentially, all that is necessary to achieve such an allocation is that as much red (blue) as possible should color the density on the link $\mathbf{c}_i$ of largest (smallest) projection onto the direction of $\mathbf{f}(\mathbf{x},t)$.

For a surface tension algorithm such as ours, it may be shown [10,11] that the form of the macroscopic surface tension Σ takes the form

$$\Sigma(\sigma,\omega)\sim\sigma/\omega, \tag{2}$$

where ω determines lattice fluid kinematic viscosity as given in Eq. (1). Other LBILG's exhibit similar dependence of Σ upon collision parameters and hence viscosity. In [6], Σ is shown to depend directly upon λ^{-1} where λ is that eigenvalue of the collision matrix which determines the simulated fluid kinematic viscosity through $\nu=-\frac{1}{8}(2\lambda^{-1}+1)$. The de-

pendence of Σ upon a collision parameter in an LB fluid has important consequences to which we shall return.

Having initialized links within a circular central portion of lattice with red density to form a drop, a shear in the x direction was applied in its far field to the outlying blue fluid by perturbing appropriate lattice-edge link densities [7]. The observed shear rate $\dot{\gamma}$ generated by this perturbation was measured as the mean value of $\partial v_x/\partial y$ over a horizontal layer 6 sites deep, always centered a fixed vertical distance from the axis of the line of undeformed drops. A position for this layer, sufficiently far from the axis to render the measured shear rate sensibly independent of system and drop size, was easy to establish for $\dot{\gamma}$ was observed to be constant over much of the blue fluid.

For the large distortions encountered in this work, approximate theories cease to apply and we here characterize drop shape and orientation only in terms of a, the largest distance from the center of mass O to any point A on the perimeter (defined by mixed color sites) and drop orientation α, the angle subtended at the horizontal by $\vec{OA}$.

All results derive from steady-state drops with undeformed radii R: $10<R<20$ lattice spacings, each evolved (collided, streamed) for 20 000 lattice updates, over which site density was initialized to 1.8 and unless otherwise stated, results relate to lattices of 90×60. Sizes of up to 140×93 were used to minimize size effects and to facilitate comparisons between drops of different initial radii, when overall lattice proportions were scaled with the initial radius. The range of surface tension parameter σ was determined by requiring the interfacial density perturbations be less than 10% of a typical nonzero velocity link density. The range of parameter ω was determined from considerations of equilibration time and stability [4].

Figure 1 illustrates a progressive drop distortion with increasing applied shear, the constant direction of which is indicated by the arrows in frame 1(a). The sequence demonstrates progressively greater departure from an initially ellipsoidal shape well before a critical shear rate $\dot{\gamma}_c$ is reached, where rupture into two or more drops occurs depending on conditions. $\dot{\gamma}_c$ was measured by increasing the perturbations applied to lattice-edge densities (throughout, these remained $<10\%$ of unforced values), allowing stabilization and measuring the resulting blue fluid shear rate while observing the final configuration of the drop(s). In this way one can determine, to any required accuracy, the value of $\dot{\gamma}$ at which rupture occurs, and its associated error, by extrapolating the (linear) graph of applied $\dot{\gamma}$ against lattice-edge perturbation beyond the last observed $\dot{\gamma}$ admitting of a whole drop. Note that $\dot{\gamma}_c$ was obtained, as for all data, at a fixed distance from the drop, in a horizontal layer of sites 25 lattice units off center.

According to approximate theory [7,12] the drop orientation α increases linearly in small applied shear. In a typical variation between α and $\dot{\gamma}$, Fig. 2 shows this linear regime in our data when $\dot{\gamma}$ is well away from the critical value. It is tempting to associate the point at which a curve of the form $\alpha=A(\dot{\gamma}-\dot{\gamma}_c)^K$ fitted through these data cuts the abscissa with the critical shear rate $\dot{\gamma}_c$ and, within the limits of observational accuracy, this did appear to be the case. However, the latter quantity, as recorded in Figs. 3–5, was actually determined as discussed above.

Taylor [13] first approximated, in the surface tension (small deformation) regime, a maximum stable radius R for drops suspended in shear fields, which may withstand the disruptive viscous stresses of the shearing fluid,

$$R=\frac{8\Sigma(\eta+\eta')}{\dot{\gamma}_c(19\eta'+16\eta)}, \tag{3}$$

with η (η') the suspending (drop) fluid shear viscosity. In our results (e.g., Fig. 1) even drops with large surface tensions depart markedly from a spherical form before burst. Strictly, Taylor's estimate (3) only indicates the conditions under which marked deviations from a spherical shape occur. However, when one considers that the only adimensional quantities that can be constructed with the parameters of the problem are a capillary number $\Sigma/R\eta\dot{\gamma}_c$ and viscosity ratio $\phi=\eta/\eta'$ it becomes clear that, at least, the general form of the last equation is valid as a means for predicting $\dot{\gamma}_c$ in terms of the present flow's parameters. Equation (3) is therefore taken as a basis for comparison with theory and by rearranging it we obtain a functional form for the critical shear rate $\dot{\gamma}_c$ at a rupture of

$$\dot{\gamma}_c=\frac{\Sigma}{R\eta}f(\phi) \tag{4}$$

where f is a function of only ϕ and which, on the basis of Taylor's approximation [Eq. (3)], would be of the form $f(\phi)=(a+b\phi)/(c+d\phi)$. We assume that (4) applies to our model and, substituting from (1) and (2), we take the dependence of $\dot{\gamma}_c$ upon simulation parameters ω, ϕ, and σ for this lattice BGK fluid to be of the form

$$\dot{\gamma}_c\sim\frac{\sigma}{R}g(\rho,\phi)\left(\frac{1}{2-\omega}\right), \tag{5}$$

where ρ denotes lattice density and $g(\rho,\phi)$ may be related to $f(\phi)$ by using (4) and the relation $\nu=\eta/\rho$. The need for a specific determination of the function $g(\rho,\phi)$ may be avoided by restricting the BGK parameter ω to take the same value in both fluids and hence $\phi=1$ in all our results.

Figures 3 and 4 exhibit the proportional dependence of $\dot{\gamma}_c$ upon independent parameter σ and $1/R$ as predicted by (5), for simulations in which the BGK relaxation parameter for both fluids is held fixed at $\omega=0.91$. For Fig. 3, the undeformed drop radius was maintained constant at $R=13$. In the case of Fig. 4 the surface tension parameter was fixed at $\sigma=0.0075$, and the lattice size was scaled to maintain a constant proportion between drop radius R and the linear lattice dimension.

Figure 5 shows the variation in $1/\dot{\gamma}_c$ with the BGK relaxation parameter ω for fixed interfacial perturbation parameter $\sigma=0.0075$ and undeformed radius $R=13$. $\dot{\gamma}_c$ was obtained for a range of equal red and blue fluid BGK relaxation parameters $0.7\leq\omega\leq1.4$, thereby maintaining the viscosity ratio ϕ constant. Collision parameter ω influences the model's macroscopic surface tension through (2) and hence (5). This latter equation predicts a linear dependence of $1/\dot{\gamma}_c$ upon ω, other parameters being constant, and Fig. 5 provides sup-

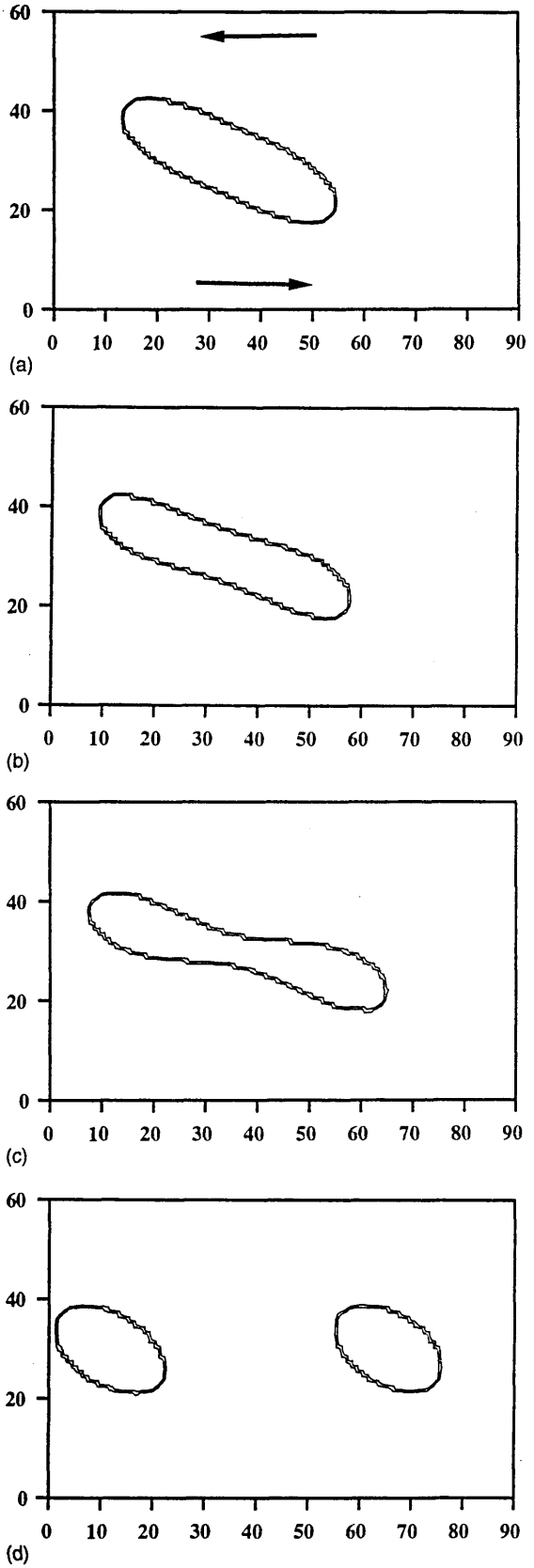

FIG. 1. Contour plots of constant red density depict a selection four configurations [(a)–(d)] in the progressive deformation and entual burst of a drop of original radius $R=13$ lattice spacings in plied shear fields of 3.270×10^{-3}, 3.503×10^{-3}, 3.569×10^{-3}, d 3.500×10^{-3} (time steps)$^{-1}$, on a lattice of 90×60. The BGK laxation parameter in use for these data was $\omega=0.91$ and the erfacial tension perturbation parameter was $\sigma=0.0075$.

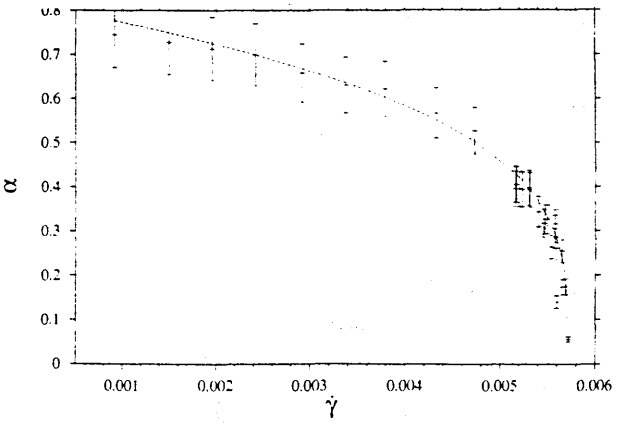

FIG. 2. A typical variation of α with $\dot{\gamma}$ for a drop with undeformed radius $R=13$, $\omega=0.91$ for both fluids and $\sigma=0.0075$ on a lattice of xy dimension of 90×60. The line fitted through this data is $\alpha=A(\dot{\gamma}-\dot{\gamma}_c)^K$. Optimum fit is obtained with the parameters $A=3.2$, $K=0.27$, $\dot{\gamma}_c=0.0057$.

port for this prediction. The recorded values of $1/\dot{\gamma}_c$ lie approximately on a line of best fit with gradient to intercept with a ratio of -0.41 against the predicted ratio -0.5 and this perhaps suggests that the model may need to be analyzed in terms of an effective relaxation parameter, possibly of the form $\omega'=k\omega$. Caution needs to be exercised, however, bearing in mind the excellent agreement with the simulation of Eq. (1) [4] and also the effect of such a modification upon macroscopic surface tension, through (2).

It is known [12] that high viscosity drops may be broken (after long times) by solenoidal (irrotational) flows but are invulnerable to flows with high vorticity. The range of our simulated fluids' kinematic viscosities was restricted and for larger values of the latter parameter ($\nu>1$, corresponding to $\omega<0.29$) the drop did not rupture with the simulationally accessible applied (nonsolenoidal) shears, instead appearing to align indefinitely to the horizontal.

In conclusion, using a lattice Boltzmann fluid we have simulated rupture in neutrally buoyant, immiscible fluid

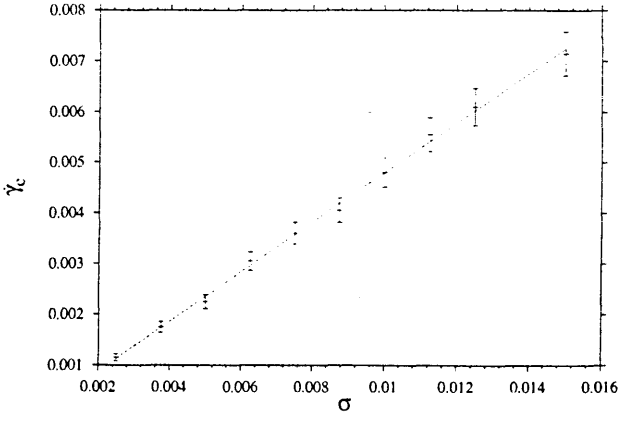

FIG. 3. Variation in $\dot{\gamma}_c$, with interface perturbation parameter σ in the range $0.002\leq\sigma\leq0.016$ with $\omega=0.9$ in both fluids. All data were obtained from a drop of constant undeformed radius R of 13 lattice units on a lattice of xy dimension 90×60. The solid line represents a straight-line least squares fit with an ordinal intercept of 9.5×10^{-5}.

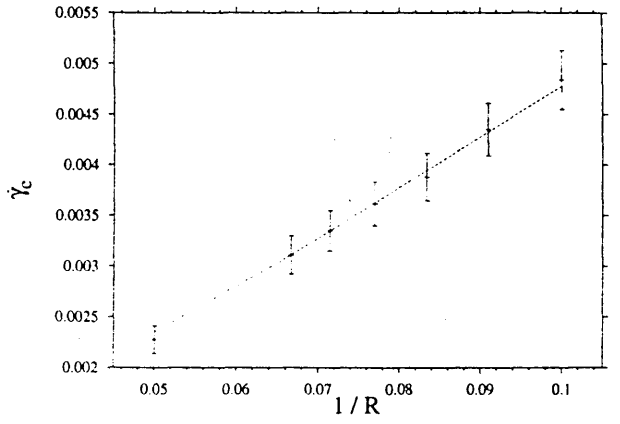

FIG. 4. Dependence of $\dot{\gamma}_c$ on reciprocal drop radius R with $10 \leq R \leq 20$ (lattices 76×56–140×92) for a drop with fixed surface tension parameter $\sigma = 0.0075$, and $\omega = 0.91$ in both fluids. The solid line represents the least squares fit to the data with an ordinal intercept of -2.3×10^{-4} (time steps)$^{-1}$.

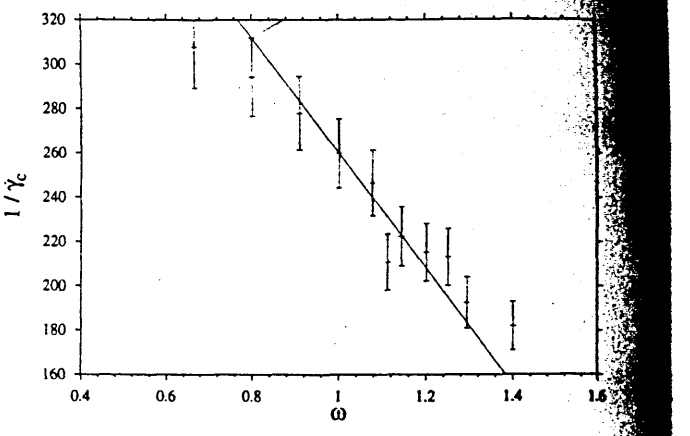

FIG. 5. Dependence of reciprocal $\dot{\gamma}_c$ on BGK parameter ω ($0.7 \leq \omega \leq 1.4$), for drops with constant surface tension perturbation parameter $\sigma = 0.0075$ and undeformed radius $R = 13$ lattice units. The solid line represents a least squares fit to these data obtained by varying the ordinal intercept c in such a way as to maintain the ratio $m/c = -0.5$, where m is the gradient.

drops of various undeformed radii R, surface tension σ, and BGK relaxation ω parameters. The dependence of macroscopic surface tension Σ upon σ and ω does not impinge upon useful application of the method since a simulator may fix ν, ϕ (via ω, ω'), and thereafter adjust Σ through σ. However, the data of Fig. 5 suggest a possible need to refine our present understanding of the interplay between σ and BGK relaxation parameter ω beyond first order in velocity.

The dependence of measured critical shear rate $\dot{\gamma}_c$ for drop burst upon all independent simulation parameters is, overall, in good agreement with a simple hydrodynamic theory and the established relationships between, for example, ω and ν [4]. The method should apply in any regime and capture the hydrodynamic interactions of drops formed *after* rupture, which provides for useful applications.

[1] U. Frisch, D. d'Humieres, B. Hasslacher, P. Lallemand, Y. Pomeau, and J. P. Rivet, Complex Syst. **1**, 649 (1987), and references therein.
[2] P. Bhatnagar, E. P. Gross, and M. K. Krook, Phys. Rev. **94**, 511 (1954).
[3] R. Kingdon (private communication).
[4] Y. H. Qian, D. d'Humières, and P. Lallemand, Europhys. Lett. **17**, 479 (1992).
[5] H. Chen, S. Chen, and W. H. Matthaeus, Phys. Rev. A **45**, 5339 (1992).
[6] A. K. Gunstensen, D. H. Rothman, S. Zaleski, and G. Zanetti, Phys. Rev. A **43**, 4320 (1991).
[7] I. Halliday and C. M. Care, Phys. Rev. E **53**, 1602 (1996).
[8] J. Olson and D. Rothman, J. Stat. Phys. **81**, 199 (1995).
[9] D. Rothman and S. Zaleski, Rev. Mod. Phys. **66**, 1417 (1994).
[10] I. Halliday and C. M. Care (unpublished).
[11] D. H. Rothman and J. M. Keller, J. Stat. Phys. **52**, 1119 (1988).
[12] J. M. Rallison, Annu. Rev. Fluid. Mech. **16**, 45 (1984).
[13] G. I. Taylor, Proc. R. Soc. London Ser. A **138**, 41 (1932).

Macroscopic surface tension in a lattice Bhatnagar-Gross-Krook model of two immiscible fluids

I. Halliday,[1] S. P. Thompson,[2] and C. M. Care[2]

[1]*Division of Applied Physics, School of Science and Mathematics, Sheffield Hallam University, Pond Street, Sheffield, S1 1WB, United Kingdom*

[2]*Materials Research Institute, Sheffield Hallam University, Pond Street, Sheffield, S1 1WB, United Kingdom*

(Received 28 March 1997; revised manuscript received 10 July 1997)

We present a method by which an interface generating algorithm, similar to that of earlier lattice Boltzmann models of immiscible fluids, may be extended to a two component, two-speed two-dimensional (D2), nine-link (Q9) lattice Bhatnagar-Gross-Krook fluid. For two-dimensional, microcurrent-free planar interfaces between the two immiscible fluids we derive expressions for static interfacial tensions and interfacial distributions of the two fluids. Extending our analysis to curved interfaces, we propose a scheme for incorporating the influence of interfacial microcurrents that is based upon general symmetry arguments and is correct to second order in lattice velocity. The analysis demonstrates that the interfacial microcurrents have only second-order influence upon the macroscopic behavior of the model. We find good agreement between our calculations and simulation results based on the microcurrent stream function and surface tension results from the pressure tensor or Laplace law. [S1063-651X(98)03801-X]

PACS number(s): 47.11.+j, 47.55.Dz, 47.55.Kf, 68.10.−m

I. INTRODUCTION

Formation of emulsions from multicomponent immiscible fluid mixtures is a complex problem of considerable technological and theoretical importance. The utility of traditional numerical methods is inhibited by advection of suspended drops and marked departures in shape before burst. As a result, there is increasing interest in the study of rheological problems by lattice Boltzmann [1–5] and, most recently, dissipative particle dynamics technique [6].

Of the *one-component* lattice Boltzmann schemes available, that which is algorithmically the simplest draws its inspiration from the work of Bhatnagar, Gross, and Krook on the Boltzmann equation of statistical physics. The eponymous *lattice* Bhatnagar-Gross-Krook (BGK) scheme has isotropy and Galilean invariance directly embedded into a technique that benefits from a simple collision step and has been shown to recover single-phase hydrodynamics [4,5]. For these reasons we construct the two-component lattice Boltzmann immiscible lattice-gas (LBILG) model described in Sec. II upon a particular variant of the BGK scheme and not the linearized lattice Boltzmann algorithm of previous work [7]. The variant used is two-dimensional with nine lattice links and is thus designated D2Q9. [5]

Multicomponent immiscible lattice Boltzmann techniques allow one to calculate flows of viscous incompressible fluid mixtures by solving the dynamics of colliding and propagating particles on a regular lattice using a Boltzmann-type equation [1–3] subject to the additional influence of a color-based segregation rule. Recently, the method has been used to simulate deformation and burst in droplets under shear in two dimensions [8,9] and sheared phase separation in three dimensions [10]. The growing literature on the method has been reviewed by Rothmann and Zaleski [11].

It has been argued that small-scale fluid velocity circulations, induced at an interface by the phase segregation rules, are endemic in LBILG simulations [8]. The influence of such microcurrents upon the macroscopic behaviour of LBILG fluids is therefore of interest. In this paper an analysis similar to that of Gunstensen *et al.* [7,8] is applied to calculate the tension in the interface generated between two D2Q9 BGK fluids.

The model is presented in Sec. II. In Sec. III we present the analysis of the static properties of two prototypical LBILG BGK based interfaces. The results are used to predict surface tension (a) in a plane interface from which symmetry precludes any microcurrent (Sec. IV) and (b) in interfaces where these circulations are present (Sec. V). For clarity, all possible commonality with the work of Gunstensen *et al.* is maintained. In Sec. VI we present details of simulations of our D2Q9 scheme, which are used to obtain mechanical and Laplace law surface tension measurements. The results and conclusions are presented in Sec. VII and VIII, respectively.

II. MODEL

Our model is a BGK scheme similar to that used in [7] but based on a square lattice that supports link density propagation at two speeds and designated D2Q9. Figure 1 and Table I serve to define the nine D2Q9 lattice velocities (links) $\mathbf{c}_j$ and the associated indexing used in this work; we note that $\mathbf{c}_9$ is a rest direction. The densities that populate the lattice are designated red or blue, $R_i(\mathbf{x},t)$ $[B_i(\mathbf{x},t)]$ denoting the red [blue] density at position $\mathbf{x}$, time t moving in direction i. Multi-component fluid behavior arises when segregation is imposed upon such densities by a generalization of the BGK collision to three steps.

First, the usual BGK collision step redistributes achromatic density

$$N_i(\mathbf{x},t) \equiv R_i(\mathbf{x},t) + B_i(\mathbf{x},t) \tag{1}$$

to links using the scalar collision operator ω, which controls fluid shear viscosity through [4,5]

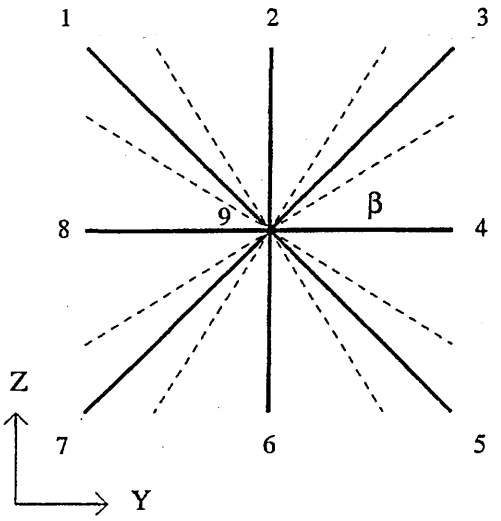

FIG. 1. Lattice link vectors (bold lines) used in the lattice BGK model for the reported simulations. Links indexed by odd values of i subtend an angle of 45° to the horizontal. The angle $\beta=26.56°$. The angular intervals into which the color field direction must be resolved in order to produce an unambiguous prioritization of link directions are each delimited by one solid and one dashed line.

$$\nu=\frac{1}{6}\left[\frac{2}{\omega}-1\right]. \tag{2}$$

In the second collision step the local lattice fluid pressure tensor $P_{\alpha\beta}(\mathbf{x},t)$, approximated [1,7] by

$$P_{\alpha\beta}(\mathbf{x},t)=\sum_i N_i(\mathbf{x},t)c_{i\alpha}c_{i\beta}, \tag{3}$$

is rendered anisotropic at interfacial sites by accumulating (denuding) density on links perpendicular (parallel) to an interface tangent. (The interfacial sites are those that include nonzero densities of both colors.) The motivation for this step is found by reference to the parent lattice-gas techniques (see, e.g., the work of Rothmann and Keller [7]) and is a process not without foundation in hydrodynamics [12]. To achieve this redistribution we follow Gunstensen *et al.* and adjust $N_i(\mathbf{x},t)$ at mixed nodes by applying a density and momentum conserving perturbation

$$\Delta N_i(\mathbf{x},t)=\sigma C(\mathbf{x},t)\cos\{2[\theta_f(\mathbf{x})-\theta_i]\}, \tag{4}$$

TABLE I. Angular orientations and components of the D2Q9 lattice velocity vectors. NA denotes not applicable.

i	c_{ix}	c_{iy}	c_i^2	θ_i	$\cos(2\theta_i)$
1	−1	1	2	135	0
2	0	1	1	90	−1
3	1	1	2	45	0
4	1	0	1	0	1
5	1	−1	2	−45	0
6	0	−1	1	−90	−1
7	−1	−1	2	−135	0
8	−1	0	1	180	1
9 (rest)	NA	NA	0	NA	NA

where σ is a *surface tension parameter* controlling the amplitude of perturbations, angle θ_i is the angular orientation of link i (Fig. 1), and $\theta_f(\mathbf{x},t)$ is the direction of a *color field* $\underline{f}(\mathbf{x},t)$, defined by

$$\underline{f}(\mathbf{x},t)=\sum_{i,j}[R_j(\mathbf{x}+\mathbf{c}_i,t)-B_j(\mathbf{x}+\mathbf{c}_i,t)]\mathbf{c}_i, \tag{5}$$

where the underline denotes a vector quantity. We have also introduced into Eq. (4) a *concentration factor* $C(\mathbf{x},t)$,

$$C(\mathbf{x},t)=1-\left|\frac{\rho_R(\mathbf{x},t)-\rho_B(\mathbf{x},t)}{\rho_R(\mathbf{x},t)+\rho_B(\mathbf{x},t)}\right|, \tag{6}$$

where $\rho_R(\mathbf{x},t)$ $[\rho_B(\mathbf{x},t)]$ denote the total of the red [blue] densities at the node with position $\mathbf{x}$. The incorporation of the concentration factor (6) into the perturbation makes evolution outside the interfacial region exactly the same as in the monophasic model and removes the possibility of surface tension being activated by *one-color* density gradients, as is the case in the "classical" immiscible lattice gas (ILG), where the presence of an interface induces changes that may be "felt," in the case of interactions between droplets, at distances of several lattice units. Thus the range of interactions is likely to be reduced by the use of the rules encapsulated in Eqs. (4)–(6), which may prove advantageous for certain applications.

In the third and final step, nodal color $\rho_B(\mathbf{x},t)$, $\rho_R(\mathbf{x},t)$ is allocated to link densities in that distribution which maximizes the work done by *color flux* $q(\mathbf{x},t)\equiv\Sigma_i[R_i(\mathbf{x},t)-B_i(\mathbf{x},t)]\mathbf{c}_i$ against the direction of $\underline{f}(\mathbf{x},t)$ [7]. Clearly, to achieve maximum segregation as much red (blue) as possible should color the density on the link $\mathbf{c}_j$ of largest (smallest) projection onto the direction of $\underline{f}(\mathbf{x},t)$. As the multi-speed nature of our lattice affects any prioritization of links for color allocation, an unambiguous hierarchy for red population of links 1–9 requires that $\underline{f}(\mathbf{x},t)$ be resolved into the 16 angular intervals identified in Fig. 1. Then, for example, the prioritization of links 1–9 that results when $\underline{f}(\mathbf{x},t)$ is found to lie in angular interval β is, in descending order, $i=3,4,5,2,9,6,1,8,7$. The need to resolve $\underline{f}(\mathbf{x},t)$ into 16 intervals emerges as one attempts to determine which of links $i=2$ or 5 is *third* most favorable for red occupation, for such prioritization can be made only after determining the direction onto which short link 2 and long link 5 have equal projection. The latter is specified by the angle $\beta=26.56°$. Symmetry then requires that the positive quadrant is resolved into the four angular intervals shown (Fig. 1). Note that link $i=9$ (rest) will always have priority 5. The propagate step in which all densities are translated by the appropriate velocity vector is carried out in the usual way on each red and blue density.

In an immiscible lattice-gas cellular automaton [7], the color field cannot influence the outcome of *monochromatic* collisions. Thus sites of high average color purity are relatively unaffected by the presence of a color field. It is this fact and the need to promote a tractable model that motivate our inclusion into the perturbation of the additional factor $C(\mathbf{x},t)$.

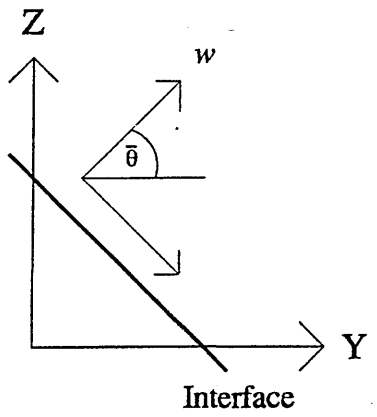

FIG. 2. Coordinate system used in the region of a planar interface.

III. ANALYSIS OF THE MODEL

Throughout we assume there to be sufficient local flatness for the mechanical definition of surface tension [12]:

$$\Sigma=\int_{-\infty}^{\infty}[P_N(w)-P_T(w)]dw \tag{7}$$

to be applicable, where w measures distance normal to the plane of the interface (Fig. 2), i.e., we assume that $P_N(w)\to P_T(w)$ quickly, as w increases. We postulate that the principal modification necessary to account for interfacial curvature derives solely from the phenomenological inclusion of the microcurrent. We consider the structure of the *steady-state* interface and therefore omit the time t from all quantities throughout the following analysis.

Consider a stable planar interface, separated about a well-defined line, a situation, if that line is appropriately selected (parallel with a lattice link direction $\mathbf{c}_i$), has sufficient transitional symmetry (parallel to the interface) to preclude variation between adjacent interfacial sites' color gradient $f(\mathbf{x},t)$. The latter [coinciding with the interfacial normal and thereby the direction of the contour of integration in Eq. (7)] may therefore be characterized by the constant angle $\bar{\theta}$ subtended at the horizontal y axis (Fig. 2). These assumptions are justified by such a situation being readily realizable in appropriately initialized lattice Boltzmann (LB) simulations [7], but note that interfacial *fluctuations* (indigenous in any class of direct simulation employing discrete particles) are present in the parent ILG technique [13,14]. However, even in the context of the ILG, a calculation, founded on assumptions similar to ours and performed within the Boltzmann approximation [1], may be employed to calculate surface tension from a prediction of the structure of the ensemble-average interface at steady state [14]. Adler, d'Humieres, and Rothman also demonstrate [14] that ILG interface fluctuations broadly obey classical statistics, but, importantly for the present work, similar fluctuations in the interfacial behavior of lattice BGK (LBGK) interfaces are not observed for the cases we consider here. We return to this point in Sec. IV. Although some similar effect might be inserted deliberately, the absence of such fluctuations from LBGK calculations is what originally motivated the model [7].

Pressure tensor contractions, analogous to those in Eq. (7), are obtained using Eq. (3) as usual:

$$P_N(\mathbf{x})=\sum_i N_i c_{iN}^2, \tag{8}$$

$$P_T(\mathbf{x})=\sum_i N_i c_{iT}^2, \tag{9}$$

where c_{iT} (c_{iN}) denotes that component of $\mathbf{c}_i$ tangential (normal) to the interface:

$$c_{iN}(\mathbf{x})=|\mathbf{c}_i|\cos(\theta_i-\bar{\theta}),\quad c_{iT}(\mathbf{x})=|\mathbf{c}_i|\sin(\theta_i-\bar{\theta}). \tag{10}$$

Following Ref. [7], Eq. (7) is considered as an average over M_0 adjacent, long integration lines z=const and then cast as a discrete summation over lattice nodes in the *area A* so-defined (Fig. 2):

$$\Sigma=\int_{w=-\infty}^{\infty}[P_N(w)-P_T(w)]dw$$

$$\to\frac{\cos(\bar{\theta})}{M_0}\sum_{\mathbf{x}\in A}\sum_i N_i(\mathbf{x})U_i, \tag{11}$$

in which the summation on $\mathbf{x}$ is over all $\mathbf{x}\in A$ and we have introduced, following Eq. (10) and the notation of Ref. [7],

$$U_i(\mathbf{x})\equiv(c_{iN}^2-c_{iT}^2)=c_i^2\cos[2(\theta_i-\bar{\theta})]. \tag{12}$$

Note that while it is independent of $\bar{\theta}$ (Sec. V), the factor $\cos(\bar{\theta})/M_0$ in Eq. (11) is retained for the sake of compatibility with the work of Ref. [7]. $N_i(\mathbf{x})$ devolves, for D2Q9, into *equilibrium* and *nonequilibrium* parts [4,5]:

$$N_i^{\text{noneq}}(\mathbf{x})\equiv N_i(\mathbf{x})-N_i^{\text{eq}}(\mathbf{u}), \tag{13}$$

$$N_i^{\text{eq}}(\mathbf{u})=t_i(1+3u_\alpha c_{i\alpha}-\tfrac{3}{2}u_\alpha u_\alpha+\tfrac{9}{2}u_\alpha u_\beta c_{i\alpha}c_{i\beta}), \tag{14}$$

$$t_i=\begin{cases}\frac{1}{36}\rho, & i=1,3,5,7\\ \frac{1}{9}\rho, & i=2,4,6,8\\ \frac{4}{9}\rho, & i=9.\end{cases} \tag{15}$$

We note that the $\mathbf{x}$ dependence of $N_i^{\text{eq}}(\mathbf{u})$ arises only through the $\mathbf{x}$ dependence of the velocity field; however, N_i^{noneq} will depend upon $\mathbf{x}$ through both the velocity and its gradients. Using Eqs. (12) and (13), Eq. (11) may be rewritten as

$$\Sigma=\frac{\cos(\bar{\theta})}{M_0}\sum_{\mathbf{x}}\sum_i N_i^{\text{eq}}(\mathbf{u})U_i(\mathbf{x})$$

$$+\frac{\cos(\bar{\theta})}{M_0}\sum_{\mathbf{x}}\sum_i N_i^{\text{noneq}}(\mathbf{x})U_i(\mathbf{x}), \tag{16}$$

the two contributions to which we proceed to treat separately. Using Eqs. (14) and (15), we find by evaluation with a standard computer algebra package, and confirmed by direct evaluation, that

$$\sum_{\mathbf{x}} \sum_{i} N_i^{\mathrm{eq}}(\mathbf{u}) U_i(\mathbf{x}) = \sum_{\mathbf{x}} \rho u^2 \cos\{2[\theta_u(\mathbf{x}) - \bar{\theta}]\}, \quad (17)$$

where we have introduced $\theta_u(\mathbf{x})$ such that

$$u_x = u \cos[\theta_u(\mathbf{x})], \quad u_y = u \sin[\theta_u(\mathbf{x})]$$

and we have used the components of $\mathbf{c}_i$ defined in Table I. To deal with the *second* term on the right-hand side of Eq. (16) we follow Gunstensen *et al.* and appeal to the lattice Boltzmann equation for the BGK algorithm, appropriately modified to account for the presence of interfacial achromatic density perturbations and adapted to the steady state [7]:

$$N_i(\mathbf{x}+\mathbf{c}_i) = N_i(\mathbf{x}) - \omega N_i^{\mathrm{noneq}}(\mathbf{x}) + \Delta N_i(\mathbf{x}). \quad (18)$$

Noting, for a closed lattice, that $\Sigma_{\mathbf{x}} N_i(\mathbf{x}+\mathbf{c}_i) = \Sigma_{\mathbf{x}} N_i(\mathbf{x})$ and using Eq. (4), one obtains after some algebra

$$\sum_{\mathbf{x}} \sum_{i} N_i^{\mathrm{noneq}}(\mathbf{x}) U_i = \frac{\sigma}{\omega} \sum_{\mathbf{x}} C(\mathbf{x}) \sum_{i} \cos[2(\theta_i - \bar{\theta})] U_i$$

$$= \frac{\sigma}{\omega} [6 - 2\cos(4\bar{\theta})] \sum_{\mathbf{x}} C(\mathbf{x}), \quad (19)$$

which we note has the expected fourfold rotational symmetry. Incorporating Eqs. (17) and (19) into Eq. (16) yields an expression for macroscopic surface tension:

$$\Sigma(\sigma,\omega) = \frac{\cos(\bar{\theta})}{M_0} \sum_{\mathbf{x}} \rho \mathbf{u}^2 \cos\{2[\theta_u(\mathbf{x}) - \bar{\theta}]\}$$

$$+ \frac{\sigma \cos(\bar{\theta})}{M_0 \omega} [6 - 2\cos(4\bar{\theta})] \sum_{\mathbf{x}} C(\mathbf{x}). \quad (20)$$

Reminding the reader that $\cos(\bar{\theta})/M_0$ is independent of $\bar{\theta}$, we remark that Eq. (20) for $\Sigma(\sigma,\omega)$ is correct to all orders of fluid velocity. The second term on its right-hand side is relatively straightforward to evaluate if we remember that $C(\mathbf{x})$ vanishes at pure, noninterfacial sites. No simplification is evident in the first term of Eq. (20), however, and the positional summation must be evaluated over all $\mathbf{x} \in A$. Notwithstanding, to leading order in $\mathbf{u}$ its contribution to $\Sigma(\sigma,\omega)$ at practical values of σ (see Sec. VII) is small. In this regime, therefore, $\Sigma(\sigma,\omega) \sim \sigma/\omega$, where we recall that ω determines lattice fluid kinematic viscosity through Eq. (2). To the same order of approximation, Gunstensen *et al.* reported an analogous dependence of their Σ upon their LBILG collision parameter λ^{-1}, where λ is the eigenvalue of the LBILG collision matrix that determines the simulated fluid kinematic viscosity.

IV. SURFACE TENSION IN PLANE INTERFACES

A. Plane interface parallel to the z axis

Throughout this and subsequent sections we take a microcurrent to be an interfacial effect resulting in a nonzero mass flux across a line parallel to a static interface and we do not consider further microcurrents defined in alternative terms, which produce no mass flux on mesoscopic length scales and have no physical influence on surface tension. Consider a steady-state planar interface parallel to short lattice links along the z axis in which color is symmetrically separated (Fig. 3), so $\cos(\bar{\theta}) = 1$. Translational symmetry along the z axis implies an absence of any microcurrent and a color gradient $\hat{f}(\mathbf{x}) = f(y)\hat{y}$. It is appropriately illustrative of the notable stability of the LB techniques in general that the direction of the color field in the final steady state is free of any fluctuations. For purposes of verification, the direction of the color field measured from simulation showed no measurable departure from this assumption. Note, however, that even for the plane geometries considered here, cellular automata based ILG simulations would contain *fluctuating* interfaces, even at "steady state."

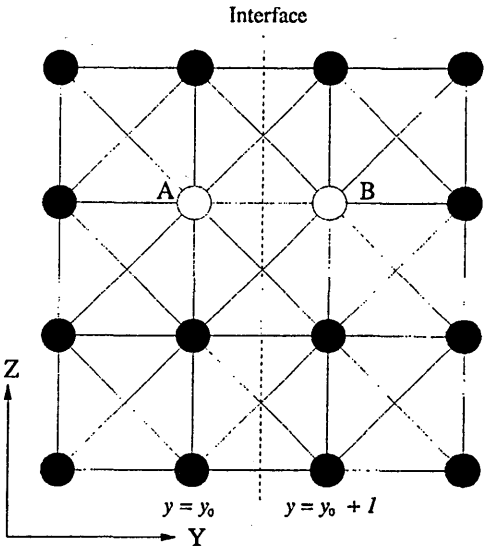

FIG. 3. Symmetry of populations in a vertical interface. This figure shows a lattice excerpt containing several mixed nodes of which two have been highlighted (open circles) in an interface centered on the dashed line. Nodes to the left are predominantly red ($\rho_R \gg \rho_B$) while, in the stable interface, those to the right are predominantly blue ($\rho_B \gg \rho_R$). Note that color populations in nodes A and B are equivalent under color reversal and rotation through 180°. The dotted line indicates the initial interface.

For these initial lattices, we consider that the stable interface cannot be centered on a single layer and will require a minimum thickness of two layers, say, $y = y_0$ and $y_0 + 1$, and a color distribution symmetrical under color reversal, corresponding to a concentration given by

$$C(\mathbf{x}) = C(\delta(y - y_0) + \delta(y - y_0 - 1)), \quad (21)$$

where C is a constant. If there are no microcurrents, $\mathbf{u} = \mathbf{0}$ everywhere and the expression for the surface tension reduces to

$$\Sigma(\sigma,\omega) = \frac{4\sigma C}{M_0 \omega} \sum_{z=1,\cdots,M_0} \sum_{\forall y} [\delta(y - y_0) + \delta(y - y_0 - 1)]$$

$$= \frac{8\sigma C}{\omega}. \quad (22)$$

At steady state, when the color content of each node must be constant between successive steps, links connecting two mixed sites should contain, at each end, counter-propagating equal densities of each color. If it is further assumed that achromatic link densities depart only negligibly from their *rest* equilibrium values t_i, the value of the constant C in Eq. (21) may be calculated.

Each interfacial site connects to three other mixed nodes and three monochromatic sites in the y direction and with two equivalent sites in the z direction (Fig. 3). We assume in the following that the sites are pure red for $y<y_0$ and pure blue for $y>y_0+1$. For diagonal, "speed 2," links $i=3,5$ in $y=y_0$ interacting with links $i=7,1$ in $y=y_0+1$:

$$R_3(y_0,z)=B_3(y_0,z)=R_5(y_0,z)=B_5(y_0,z)=\tfrac{1}{2}t_1=\tfrac{1}{72}\rho_0,$$

$$R_1(y_0+1,z)=B_1(y_0+1,z)=R_7(y_0+1,z)=B_7(y_0+1,z)$$
$$=\tfrac{1}{2}t_1=\tfrac{1}{72}\rho_0,$$

and similarly for the speed 1 link $i=4$ in $y=y_0$ interacting with link $i=8$ in $y=y_0+1$:

$$R_4(y_0,z)=B_4(y_0,z)=\tfrac{1}{2}t_2=\tfrac{1}{18}\rho_0,$$

$$R_8(y_0+1,z)=B_8(y_0+1,z)=\tfrac{1}{18}\rho_0,$$

where ρ_0 is the achromatic density of the interfacial lattice node and we have used identities (15). With this information the color density of the nodes in $y=y_0$ may be calculated:

$$\rho_B(y_0,z)=B_3(y_0,z)+B_4(y_0,z)+B_5(y_0,z)$$
$$=(\tfrac{1}{72}+\tfrac{1}{72}+\tfrac{1}{18})\rho_0=\tfrac{1}{12}\rho_0,$$

$$\rho_R(y_0,z)=\rho_0-\tfrac{1}{12}\rho_0=\tfrac{11}{12}\rho_0,$$

whence, from Eq. (6), $C=\frac{1}{6}$. This value for C, on insertion into Eq. (22), gives, for our model of a horizontal interface parallel to the short D2Q9 lattice links, a macroscopic surface tension

$$\Sigma(\sigma,\omega)=\frac{4\sigma}{3\omega}. \tag{23}$$

B. Plane diagonal interface

For a steady *diagonal* plane interface separated in a line parallel to the longer lattice links (Fig. 4) two different (but simply related) cross-interface density profiles occur. However, the macroscopic surface tension can be calculated with a small modification. In the simplest case of an interface constituted by mixed sites A,B in adjacent sections aa',bb' (Fig. 4) densities at A, $\{R_i(A),B_i(A)\}$, and those at B, $\{R_i(B),B_i(B)\}$, are equivalent under combined color reversal and a two-fold rotation. If the achromatic densities are again assumed to depart negligibly from their rest equilibrium values t_i, the simplest distribution of color through this diagonal interface may be deduced. For links in the only (mainly red) mixed node in section aa' (Fig. 4), connecting to the mixed mainly blue node in two bb' sections, postcollision densities are

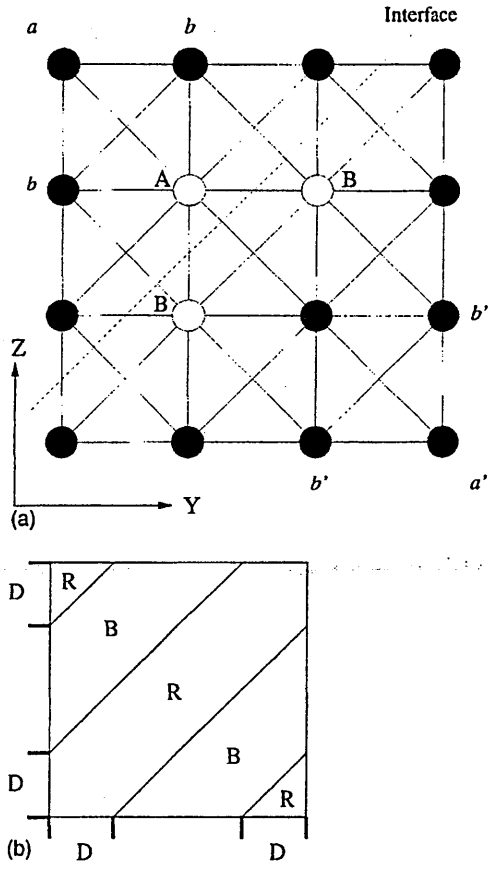

FIG. 4. (a) Populations in a diagonal interface. This figure shows a lattice excerpt containing several mixed nodes of which three have been highlighted (open circles) in the interface centered on the dashed line. Nodes above the dashed line are predominantly red ($\rho_R\gg\rho_B$), while, in the stable interface, those below are predominantly blue ($\rho_B\gg\rho_R$). Populations in nodes A and B are again equivalent under color reversal and rotation through 180°. (b) Initial distribution of color for the simulation of a diagonal interface on the square D2Q9 lattice showing the periodic images of the red diagonal layer in the box corners. Regions marked R (B) correspond to red (blue) mass. Distance $D=27$ lattice units.

$$R_4(A)=B_4(A)=R_6(A)=B_6(A)=\tfrac{1}{2}t_2=\tfrac{1}{18}\rho_0, \tag{24}$$

while for link 5 in section aa' connecting to a pure blue node

$$R_5(A)=0,\quad B_5(A)=t_1=\tfrac{1}{36}\rho_0, \tag{25}$$

where we have again used identities (15). Densities for the mixed B node are easily obtained from the symmetry arguments already rehearsed. The color density of the mixed nodes in the diagonal interface is therefore

$$\rho_B(A)=B_5(A)+B_4(A)+B_6(A)=(\tfrac{1}{36}+\tfrac{1}{18}+\tfrac{1}{18})\rho_0=\tfrac{5}{36}\rho_0, \tag{26}$$

$$\rho_R(A)=\rho_0-\tfrac{5}{36}\rho_0=\tfrac{31}{36}\rho_0, \tag{27}$$

whence, from Eq. (6), $C=\frac{5}{18}$ for both the A and B mixed sites. Setting $\bar{\theta}=45°$ and noting that there is an A *and* a B

mixed site on any horizontal line crossing a diagonal interface, it follows from Eq. (20) that the macroscopic surface tension is

$$\Sigma(\sigma,\omega)=\frac{40\sigma}{9\sqrt{2}\omega}. \tag{28}$$

The preceding analysis of flat interfaces between static fluids neglects perturbation-induced departures from equilibrium rest density, the validity of which assumption increases with decreasing perturbation amplitude σ and is supported from the results of Sec. V. It should be noted that this assumption implicitly restricts the principal analytical results of this section [Eqs. (23) and (28)] to apply when the induced macroscopic surface tension is small. Note also that due to the absence of local curvature in the interface no density (pressure) change between the bulk fluids separated by the interface is to be expected. Moreover, the fact that, for the present model in the case of, e.g., the vertical interface along the z direction, the population of link 4 may, on general grounds, be different from that of links 3 and 5 allows for density to be constant through the interface. We now consider the effect of microcurrents that are precluded by symmetry in planar interfaces.

V. SURFACE TENSION IN CURVED INTERFACES

Microcurrents are normally induced close to an interface by the segregating effect of the surface tension rule [8,9,15]; only in the presence of suitable symmetry, such as the cases considered in Sec. IV, will the microcurrents be absent. The presence of interfacial curvature and a gradient in the color field mean makes it impossible to argue on general grounds that an interfacial microcurrent should be absent from the rest interface. Its influence will be felt principally through the first term in Eq. (20). The magnitude of the microcurrent velocity close to the interface has been observed [8,15] to be of the form

$$u=u(\mathbf{x})\sigma. \tag{29}$$

For circular interfaces in two-dimensional simulations of static (say) red drops, the interfacial microcurrent pattern must conform with the rotational symmetry of the underlying lattice and two complementary, counterrotating microcurrent *cells* must occupy any lattice quadrant, the maximum velocity in each occurring close to the generating interface (Fig. 6). In fact, the maximum value of the surface tension inducing perturbation occurs for the maximum value of U_i in Eq. (12) at $\bar{\theta}=45°$, accounting for the fact that the microcurrent circulation close to the interface is radial along the diagonal bisectors of each quadrant (Fig. 6). Moreover, on grounds of lattice symmetry and hydrodynamics (which must ultimately govern the microcurrent), one expects the extent of a microcurrent cell to be determined by lattice extremities and drop radius R. We approximate the flow in a microcurrent cell outside the interface with a uniform rotation such that its outermost streamline touches the interface and has a velocity determined principally by σ. We then write the microcurrent velocity field $u(\mathbf{x})=u(\hat{r},|\underline{r}|/R)$ in Eq. (25) and note that $\mathbf{u}(\hat{r},|\underline{r}|/R)$ must have the fourfold rotational symmetry of the lattice. Hence Eq. (20) becomes

$$\Sigma=\frac{\sigma^2\cos(\bar{\theta})}{M_0}\sum_{\mathbf{x}} u(\hat{r},|\underline{r}|/R)^2\rho\cos\{2[\theta_u(\mathbf{x})-\bar{\theta}]\}$$
$$+\frac{\sigma\cos(\bar{\theta})}{M_0\omega}[6-2\cos(4\bar{\theta})]\sum_{\mathbf{x}} C(\mathbf{x}). \tag{30}$$

This result, it should be noted, applies only to the D2Q9 BGK model through the assumed form of the equilibrium distribution function defined in Eqs. (14) and (15) and introduced by Qian, d'Humieres, and Lallemand [5]. Clearly, the potential for anisotropy entailed in the second term therefore applies only to the model under consideration here and the actual extent of any anisotropy in surface tension may be determined only after $C(\mathbf{x})$ is known. To interpret Eq. (30) in the presence of curvature, we consider an interfacial element of length $R\Delta\theta$ from a large circular drop of radius R, subtending a small angle $\Delta\theta$ at the drop center. This element we assume to be locally flat and contained within an area defined by M_0 long horizontal lattice lines $z=$const. Then $M_0=R\Delta\theta\cos(\bar{\theta})$, whence $\cos(\bar{\theta})/M_0=1/R\Delta\theta$. The magnitude of the positional summation in the second term of Eq. (30) will be proportional to $R\Delta\theta$ and a form $\sigma k_2/\omega$ is assumed. With respect to the first term, we take the microcurrent activity to decay rapidly away from the interface (an assumption supported by the results of Fig. 7) and this will yield finite contributions to the first summation only from a number of sites proportional in number to the $R\Delta\theta$ and the velocity at all of these sites we take to be determined principally by σ. The positional summation in the first term in Eq. (30) will therefore also be proportional to $R\Delta\theta$ and we assume a form $\sigma^2 k_1$. For the interfacial tension of a drop we therefore find

$$\Sigma(\sigma,\omega)=\sigma^2 k_1+\frac{\sigma}{\omega}k_2, \tag{31}$$

in which for small values of the perturbation parameter σ, the dominant contribution is from the second term and hence

$$\Sigma(\sigma,\omega)\cong\frac{\sigma}{\omega}k_2. \tag{32}$$

VI. SIMULATION

In order to make a comparison with the calculations for plane interfaces we construct an effectively infinite system and thus periodic boundaries were used all around a square lattice and retained for all other simulations reported here. A suitable box size and equilibration time were determined on the basis of stability. For all the data presented, sites were initialized to achromatic density $\rho_0=1.8$ with rest equilibrium link densities of 0.8, 0.18, and 0.045 for speed 0, 1, and 2 links, respectively, the initial color being allocated so as to produce a particular interface configuration.

Results were obtained for plane, $y=$const, interfaces on a 120×120 lattice containing a red vertical layer sandwiched between two blue fluids. The initial interface lay between consecutive y planes of nodes and the red layer was defined

TABLE II. Calculated and measured values of the Laplace law surface tension. Calculated values are derived from Eqs. (23) and (28). For the planar horizontal interface $(\sigma,\omega)=(5\times10^{-3},0.91)$, while for the planar diagonal interfaces simulated $(\sigma,\omega)=(5\times10^{-4},0.91)$.

Interface orientation	Calculated $\Sigma(\sigma,\omega)$	Measured $\Sigma(\sigma,\omega)$	Calculated C	Measured C
horizontal	7.33×10^{-3}	7.37×10^{-3}	0.166	0.15
diagonal	1.73×10^{-3}	1.73×10^{-3}	0.28	0.28

by $\rho_R(x,y)=1.8$ and 0, $39<y<81$. The diagonal interface was constructed by initializing as red those nodes which lay on the lattice of Fig. 4(b) with y coordinates such that $z-26\leq y\leq z+26$, *with the periodic images of this red layer incorporated in the lattice corners* [Fig. 4(b)]. An equilibration time of 15 000 updates was allowed for both plane interface orientations and the steady-state density distribution was measured through the interfacial region. Also measured through the interface was quantity P_N-P_T, using Eqs. (8) and (9). These measurements, in conjunction with a simple discrete approximation to the mechanical definition (7), allowed the planar interfacial tension to be evaluated.

Links within a circular, central portion of radius R of an otherwise blue 150×150 lattice were initialized red to form a circular drop. Different combinations of surface tension perturbation parameter σ and BGK collision parameter ω were used to generate stable drops with the values of ω now being chosen so as best to recover classical hydrodynamic behavior [16]. Laplace law measurements were used upon these drops to obtain surface tension $\Sigma(\sigma,\omega)$ from the gradient of pressure difference $\Delta p=\Delta\rho/3$ [4,5] as a function of $1/R$ for $15<R<40$. The steady-state value of R was obtained from the drop inertia tensor [8].

In order to observe the influence of microcurrent activity from circular interfaces the stream function

$$\psi(x,y)=\int_{y=0}^{y'=y}u_y(x,y')dy' \tag{33}$$

was calculated from the velocity field along with the corresponding pressure (lattice density) field. The variation with normalized distance from the drop center $\bar{r}\equiv r/R$, of velocity modulus averaged over an annular lattice sample concentric with the drop center, radius $\bar{r}$, yields a quantitative measure of microcurrent activity and a test of the assumptions made in deriving Eq. (31).

VII. RESULTS

Consistent with the assumptions made in Sec. II, quiescent color mixing in appropriately initialized plane interfaces was confined to layers of two sites. Table II shows the close agreement between calculated and measured interfacial quantities for both cases of planar interface considered. The measured values of surface tension were obtained directly from a trapezium rule approximation to Eq. (7):

$$\Sigma(\sigma,\omega)=\frac{|\mathbf{c}_i|}{2}\left(\sum_l\left[P_N(l)-P_T(l)+P_N(l+\mathbf{c}_i)-P_T(l+\mathbf{c}_i)\right]\right), \tag{34}$$

where l denotes position on a lattice line perpendicular to the interface and we use Eqs. (8) and (9) to obtain $P_N(l),P_T(l)$.

Figure 5(a) shows, on the same axes, normalized variation of color and pressure tensor contraction $[P_N(l)-P_T(l)]$ through the vertical interface described in Sec. III. For the corresponding case of a diagonal interface [Figs. 5(b) and 5(c)] color is not, as expected, symmetrically distributed about the maximum value of $P_N(l)-P_T(l)$; Figs. 5(b) and 5(c) represent sections of the interface along adjacent diagonals (Fig. 4) that are interrelated by a rotation of π radians and a color reversal. For the results of Fig. 5 the BGK collision parameter $\omega=0.91$ was used in conjunction with surface tension perturbations $\sigma=0.005$ [Fig. 5(a)] and $\sigma=0.0005$ [Figs. 5(b) and 5(c)].

Figure 6 shows the microcurrent structure generated at the surface of a red drop through the stream function $\psi(x,y)$ calculated by a process of numerical integration after Eq. (33). The microcurrents are seen to be consistent with the symmetry of the underlying lattice and the maximum perturbation. The range of influence of the microcurrent for a periodically bounded drop on a 150×150 lattice is shown in Fig. 7, which charts the variation of $|\mathbf{u}|$, flow speed, against normalized distance form the drop center $|\underline{r}|/R$ for several values of parameter σ. As a quantitative assessment we note that Eq. (31) predicts that a graph of $\Sigma(\sigma,\omega)/\sigma$ against $1/\omega$ will have an ordinal intercept (gradient) from which constant k_1 (k_2) may be inferred. Accordingly (Fig. 8), $\Sigma(\sigma,\omega)/\sigma$ was obtained from Laplace's law (see Sec. VI) applied to drops with $0.5\leq\omega\leq2.0$ and $\sigma=0.025$. With the latter value of perturbation parameter the number of data points necessary to apply linear regression reliably entails significant processing, but yields values of 30.55 and 1.26 for k_1 and k_2. Hence, for $\sigma=0.025$, the microcurrent contribution to the macroscopic surface tension in our model is seen to approximate to that arising from the second term in Eq. (31) and we infer an estimated upper limit $\sigma\leq0.025$ such that, for the particular model of the present study, the influence of a microcurrent upon the macroscopic surface tension is of decreasing importance.

Figure 9 concentrates upon values of $0.001\leq\sigma\leq0.0125$, well below this upper limit, and shows results for surface tension $\Sigma(\sigma,\omega)$ for $1.5\leq\omega\leq1.9$ plotted against the quotient σ/ω; these results for the surface tension are derived from Laplace law measurements described above. The continuous line represents a linear regression fit to this data and although *unconstrained* to pass through the origin, the fit generates an intercept that lies well within one standard deviation of zero and a gradient that identifies k_2 [Eq. (32)]. Obtained from Eq. (20), Eq. (23) is valid for a flat horizontal interface at rest. Based as it is on the mechanical definition of surface tension [12] [Eq. (20)], we interpret only with respect to equilibrium (rest) fluids and the velocity dependence entailed in its first term, we suggest, should be regarded as arising only from that flow present in a rest simulation: the mi-

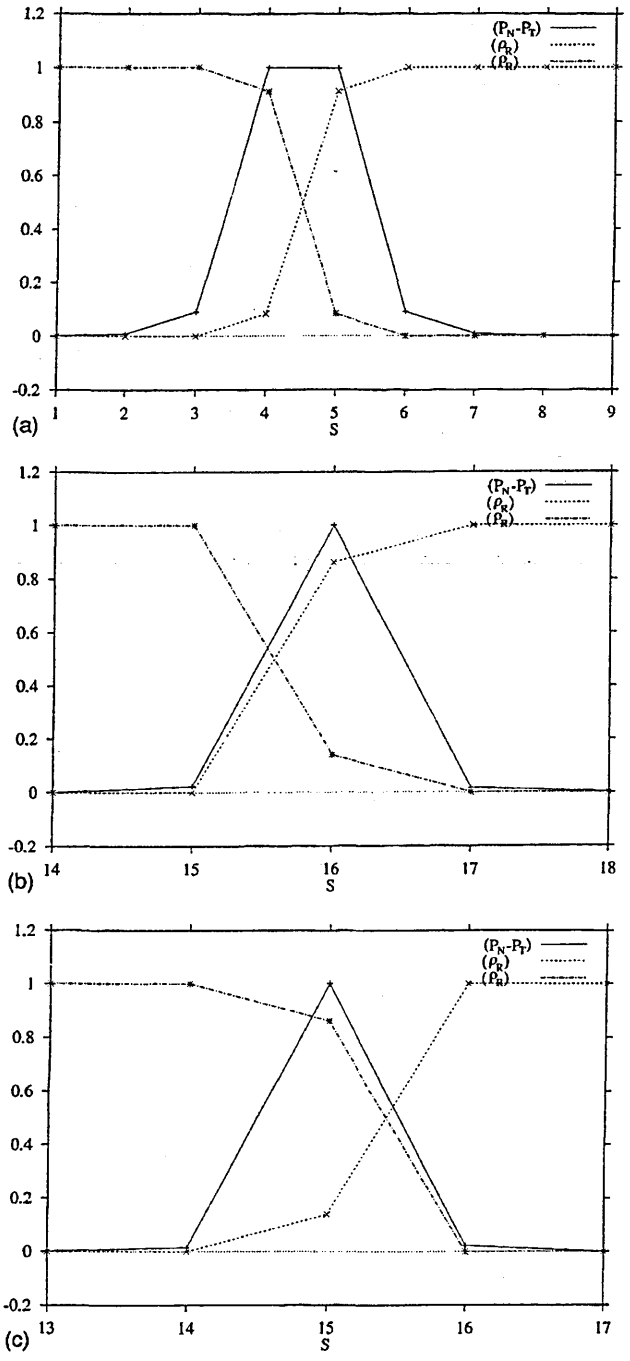

FIG. 5. (a) Normalized variations across a vertical interface, with S measured in lattice units. The dotted (dashed) line connects calculated blue (red) densities and symbols mark corresponding measured values. The solid line corresponds to the value of $P_N - P_T$. The achromatic density in use was $\rho_0 = 1.8$, $\omega = 0.91$, and $\sigma = 0.005$. (b) Normalized variations across a diagonal interface, sampled along aa' (Fig. 4). The parameter s is related to the coordinate y through $s = \sqrt{2}y$. After (a) lines connect calculated points and symbols show results obtained from simulation. The solid line corresponds to the value of $P_N - P_T$. The achromatic density in use was $\rho_0 = 1.8$, $\omega = 0.91$, and $\sigma = 0.005$. As expected, this plot does not show the same color-reversal symmetry as in the case of (a); instead the color distribution is related to that displayed in (c); See Sec. IV B. (c) Normalized variations across a diagonal interface, sampled along bb' (Fig. 4). Other parameters are the same as in (b).

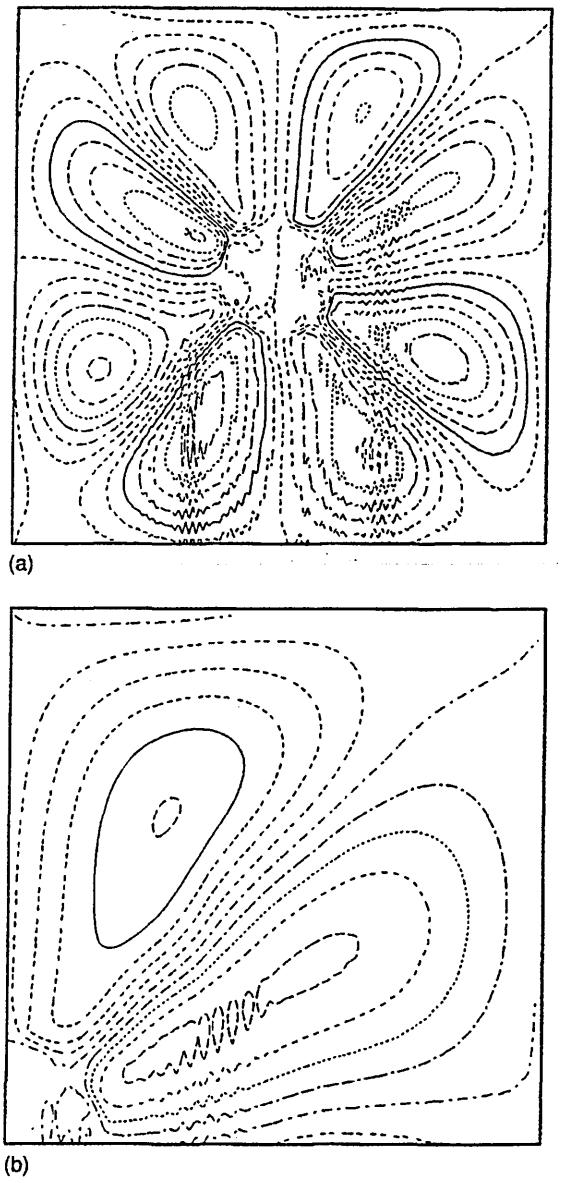

FIG. 6. Stream function for steady circulation pattern developed by a drop of radius 40 lattice units placed centrally on a square lattice. The flow pattern is observed to be stable after approximately 4000 time steps. The results were obtained for the same simulation parameters as Fig. 5(a).

crocurrent. Nevertheless, a useful check on Eq. (20) may be performed by applying a uniform shear of increasing rate parallel to the flat vertical layer $-10 \leq y \leq 10$ on a 60×60 lattice (see the discussion above and Fig. 3), the shears being generated in the usual manner [8,9]. Setting $\bar{\theta} = 0$ and $\theta_u(\mathbf{x}) = \pi/2$ for small σ, we may omit the second term from Eq. (20) and

$$\Sigma(\sigma,\omega) \sim -\frac{\rho}{M_0} \sum_{\mathbf{x}} \mathbf{u}^2 = -\rho \sum_{y=-10}^{y=20} \mathbf{u}(y)^2. \qquad (35)$$

Figure 10 shows the results of plotting $\Sigma(\sigma,\omega)$, obtained from Eq. (34), as the ordinate against summation $S_0 \equiv \Sigma_{y=-10}^{y=20} \mathbf{u}(y)^2$, obtained for a small range of shear rates, as the abscissa, with the expected linear trend emerging. At

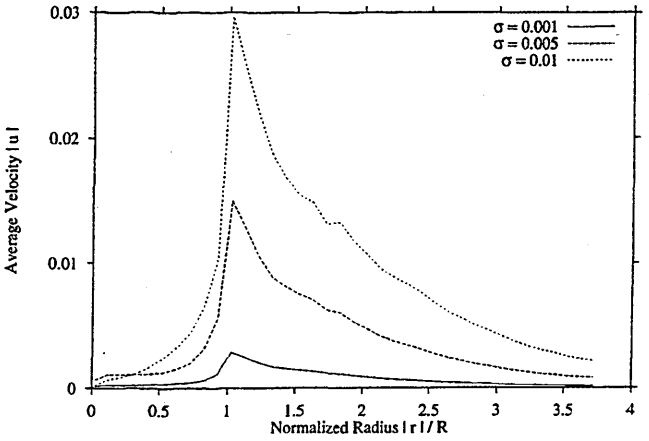

FIG. 7. Variation of $|\mathbf{u}|$, microcurrent flow speed measured in units of lattice spacing per time step, against normalized distance from the drop center $|\underline{r}|/R$ for several values of parameter σ (see key). Note the approximately linear trend in peak flow activity with σ, which occurs close to the interface.

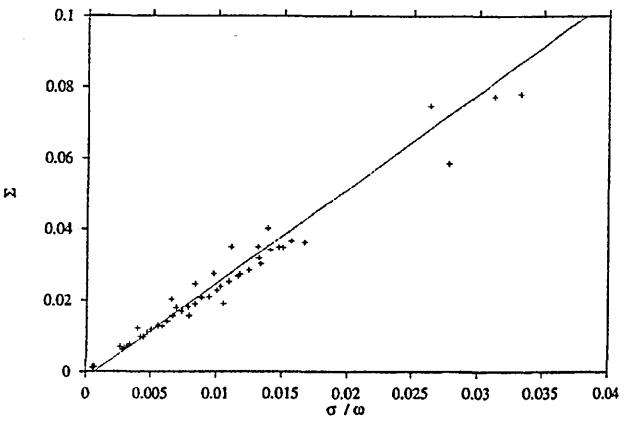

FIG. 9. Plot of $\Sigma(\sigma,\omega)/\sigma$ (measured in lattice units) against (dimensionless) $1/\omega$ for $0.5 \leqslant \omega \leqslant 2.0$. The former were obtained from Laplace's law applied to drops with $\sigma = 0.025$ and $15 \leqslant R \leqslant 40$ on a 150×150 lattice.

smaller shear rates the (constant, positive) contribution of the first term in Eq. (20) begins to become apparent. It is important to note that, for the reasons set out above, we do not claim that Fig. 10 represents more than an interesting property of Eq. (20), Eqs. (20) and (30) resting on definitions in which a static interface is implicit [12].

VIII. CONCLUSIONS

We have presented a method by which the interface generating algorithm of Gunstensen *et al.*, itself an extension of the automaton-based algorithm of Rothman and Keller [7], may be successfully extended to a D2Q9 lattice BGK scheme and generalized to promote both tractability and correspondence with the progenitor cellular automaton technique. As Table II shows, simulation measurements of surface tension and cross-interfacial color distributions for this model are in good agreement with those values calculated from analysis of our algorithm, for both plane horizontal and diagonal microcurrent-free interfacial orientations. The difference between the two expressions suggests an orientational-dependent anisotropy in the model's surface tension and the effect of this upon shape in drops simulated by this method is currently under study. We have deduced, on general grounds, the structure of the microcurrent circulation generated by circular drops and compared these with measurements. These measurements demonstrate that the simple theory successfully accounts for the broad structure of the microcurrent flow field. The analysis allows us to develop an expression [Eq. (31)] for the surface tension of a drop and this expression demonstrates that the microcurrent velocity field might be expected directly to influence the model's surface tension. For small values of parameter σ the corrections are only found to be second order in σ and this is

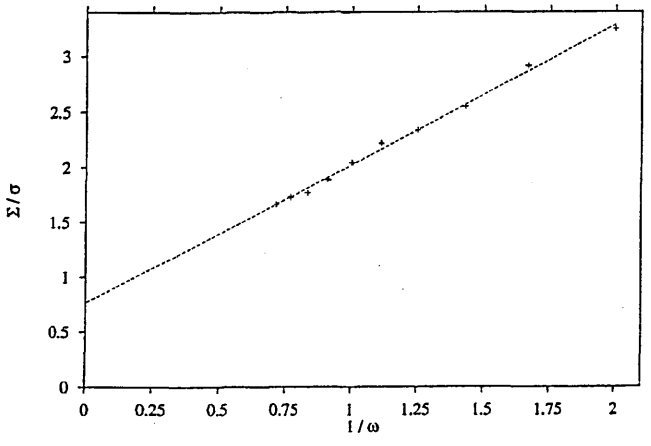

FIG. 8. Simulational measurements of the Laplace law surface tension $\Sigma(\sigma,\omega)$ (measured in lattice units) for $0.001 \leqslant \sigma \leqslant 0.0125$, $1.5 \leqslant \omega \leqslant 1.9$ as a function of quotient σ/ω (where σ and ω are dimensionless). The continuous line is a linear regression fit to the data.

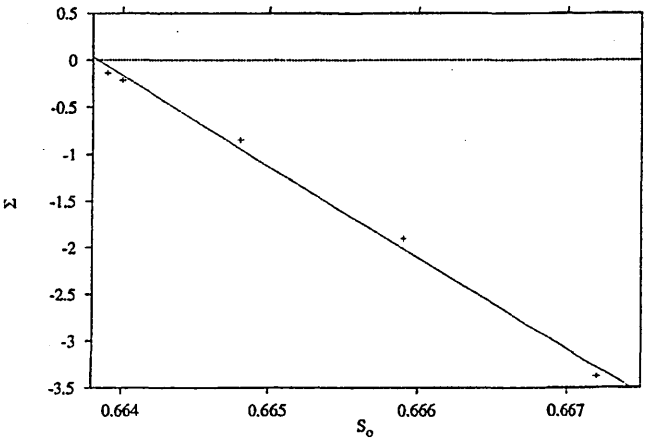

FIG. 10. $\Sigma(\sigma,\omega)$ [measured in lattice units obtained from Eq. (34)] as ordinate against summation $S_0 \equiv \Sigma_{y=-10}^{y=20} \mathbf{u}(y)^2$ (dimensions of lattice units squared) for a vertical interface exposed to a uniform shears parallel to the vertical interface $-10 \leqslant y \leqslant 10$ placed on a 90×60 lattice.

substantiated by the measurements summarized in Fig. 9. Any attempt quantitatively to assess the approximate theory of microcurrent contribution presented here will require substantial quantities of data and should be undertaken only after a more rigorous analysis of the contribution of the first term in Eq. (31). The undertaking would be facilitated by a calculation of the steady microcurrent flow field as an approximate or numerical solution of the equations of creeping flow, which should fully account for the microcurrent structure. Although our general arguments yield a qualitative insight into the origin of the microcurrent, such a calculation would provide the most useful check on our understanding of this phenomenon and hence upon the ability of the method in the area of its most important potential application.

[1] U. Frisch, D. d'Humieres, B. Hasslacher, P. Lallemand, Y. Pomeau, and J. P. Rivet, Complex Syst. **1**, 649 (1987), and references therein.
[2] G. McNamara and G. Zanetti, Phys. Rev. Lett. **61**, 2332 (1988).
[3] For an extended bibliography see *Lattice Gas Methods for Partial Differential Equations*, edited by G. D. Doolen (Addison Wesley, Reading, MA, 1989).
[4] R. Kingdon (private communication).
[5] Y. H. Qian, D. d'Humieres, and P. Lallemand, Europhys. Lett. **17**, 479 (1992).
[6] P. Espanol, Phys. Rev. E **52**, 1734 (1995).
[7] A. K. Gunstensen, D. H. Rothman, S. Zaleski, and G. Zanetti, Phys. Rev. A **43**, 4320 (1991); D. H. Rothman and J. M. Keller, J. Stat. Phys. **52**, 111 (1988); A. K. Gunstensen and D. H. Rothman, Europhys. Lett. **18**, 157 (1992).
[8] I. Halliday and C. M. Care, Phys. Rev. E **53**, 1602 (1996).
[9] I. Halliday, C. M. Care, S. Thompson, and D. White, Phys. Rev. E **54**, 2573 (1996).
[10] J. F. Olson and D. H. Rothman, J. Stat. Phys. **81**, 199 (1995).
[11] D. Rothman and S. Zaleski, Rev. Mod. Phys. **81**, 181 (1995).
[12] J. S. Rawlinson and B. Widom, *Molecular Theory of Capillarity* (Oxford University Press, New York, 1989).
[13] J. Armstrong (unpublished).
[14] C. Adler, D. d'Humieres, and D. H. Rothman, J. Phys. I **4**, 29 (1994).
[15] A. K. Gunstensen, Ph.D. thesis, Massachusetts Institute of Technology 1992 (unpublished).
[16] O. Behrend, R. Harris, and P. B. Warren, Phys. Rev. E **50**, 4586 (1994).

Mesoscopic hydrodynamics of diphasic Lattice Bhatnagar Gross Krook fluid interfaces

S. P. Thompson,[a] I. Halliday[b] and C. M. Care[c]

[a] *Computer Services for Academic Research (CSAR), Manchester Computing, The University of Manchester, Oxford Road, Manchester, UK M13 9PL*
[b] *Division of Applied Physics, School of Science and Mathematics, Sheffield Hallam University, Pond Street, Sheffield, UK S1 1WB*
[c] *Materials Research Institute, Sheffield Hallam University, Pond Street, Sheffield, UK S1 1WB*

Received 16th December 1998, Accepted 19th February 1999

We consider the most appropriate way to assess the interfacial tension locally, on a meso-scale, in one particular class of diphasic lattice Bhatnagar Gross Krook fluid, in which the interface is supported by a simple segregation algorithm. Our investigative methodology and observations will support similar analysis of other lattice Boltzmann models containing discrete interfaces. By assessing the performance of a lattice fluid/fluid interface against the most general hydrodynamic boundary conditions, we measure an orientational dependence in the model's surface tension. In attempting to assess this anisotropy, which must obstruct the performance of the model and others similarly conceived, we devise a simple correction to the segregation algorithm. The useful result provides a platform for future work.

1 Introduction

Given their physical and practical significance, it is unfortunate that traditional numerical methods find difficulty in simulating *diphasic* fluids: two-component immiscible fluid mixtures. The past decade has, however, seen increasing interest in the study of rheological problems using better-adapted, novel techniques. Lattice Boltzmann (LB) simulation is one such method with acknowledged advantages making LB a very useful tool for simulating (amongst other things) diphasic fluids, particularly at the meso-scale.

Currently several diphasic LB-based methods exist, each employing a different algorithm to segregate the simulated fluids (see below). Here we attempt fundamentally to assess the *hydrodynamics* of a diphasic LB as it might be used to simulate multi-component flow: that is, in the narrow interface limit. Therefore, whilst the most recent segregation algorithms capture, for instance, phase separation kinetics,[1] for present purposes an adaptation[2] of a much earlier, minimal segregation algorithm due to Gunstensen[3] is used. This algorithm is nevertheless capable of producing the narrow interfacial region germane to applications in multi-component flow simulation. Moreover the particular LB model is ancillary: our methodology might be applied to assess the hydrodynamics of any diphasic LB simulation.

Key developments in the monophasic LB method and its additional *segregation rules* for immiscible fluids are contained in refs. 1 and 3–12. Of all monophasic LB schemes, the simplest (Qian *et al.*,[11]) is inspired by the work of Bhatnagar, Gross and Krook on the Boltzmann equation. The eponymous *lattice* BGK (LBGK) scheme designated D2Q9[11] is the *core* model for our diphasic LBGK, outlined in Section 2 (see also ref. 2). Diphasic lattice Boltzmann techniques allow one to calculate flows of immiscible fluid mixtures by augmenting the core lattice Boltzmann algorithm with an additional segregation rule which acts between the separated fluids, which are traditionally designated red and blue. These rules differ considerably: in Shan and Chen,[12] Gunstensen *et al.*[3] and Swift *et al.*[1] the interface is maintained in rather different ways and each of these extensions to the core LB method have been used to simulate a range of problems: Laplace Law behaviour,[3] deformation and burst in droplets under shear in two dimensions,[13,14] sheared phase separation in three dimensions and as a vehicle to study the kinetics of phase separation.[1,15,16] The growing literature on the method has been reviewed by Rothman and Zaleski.[17] Our particular model is defined in Section 2).

Broadly, the results from the different segregation algorithms are consistent with what is observed in the corresponding physical system. However, the extent to which any of the above methods are *hydrodynamic* at the meso-scale (in the sense that each should generate a surface of separation conforming with the boundary conditions obtaining at the deformable interface of tension between two viscous fluids[18] has not, to our knowledge, been assessed. Researchers have, for example, measured diphasic LBs' interfacial properties macroscopically, by considering certain interfacial configurations (shapes), then comparing with known results from hydrodynamics: so the most direct measurements of a model's interfacial tension are from Laplace Law results applied to (assumed) circular drops, or from the pressure tensor definition of surface tension on planar interfaces, see for example refs. 3 and 13 and references therein. The meso-scale hydrodynamics of the interface remains uninvestigated.

We show here, for example, that Laplace Law behaviour emerges as an average from richer interfacial conditions. Moreover, we observe that a diphasic segregation algorithm in the narrow interface limit will tend to generate an anisotropic surface in consequence of the underlying lattice (see also ref. 2). This anisotropy does not preclude static Laplace law behaviour, or qualitatively correct hydrodynamics in respect of *e.g.*, sheared drop burst: interfacial behaviour is useful and passes a first macroscopic test. But issues of anisotropy in the surface tension, and the quality of the interfacial behaviour on the meso-scale are clearly relevant.

At their most general, the hydrodynamic boundary conditions for normal and tangential stress transmission, on the meso-scale at the isothermal interface between two immiscible fluids without gradients in the interfacial tension are:[18,19]

$$\sigma^{R}_{x\beta} n_\beta - \sigma^{B}_{x\beta} n_\beta = \Sigma\left(\frac{1}{R_1} + \frac{1}{R_2}\right) n_x \quad (1)$$

$$\sigma'^{R}_{x\beta} t_\beta - \sigma'^{R}_{x\beta} t_\beta = 0 \quad (2)$$

Here Σ is the macroscopic surface tension, $\sigma_{x\beta}$ is the stress tensor, $\sigma'_{x\beta}$ is the viscous stress tensor[18] and the normal and tangent to the interface are represented by $\hat{n}$ and $\hat{t}$ respectively. R_1 and R_2 are the principle radii of curvature of the interface.[18]

The two dimensional Laplace law $\Sigma = \Delta p/R$ is a special case of eqn. (1) for zero flow. Whilst the Laplace law has been widely used to characterise multiphasic LBGKs, we suggest that it is the extent to which the more general condition of eqn. (1) is represented in diphasic LBGK hydrodynamics that is the significant measure. Moreover eqn. (1) applies *locally*, to all interfacial elements in all cases (hence our designation *mesoscopic*) unlike the Laplace Law, which applies to a particular (zero-flow) situation. Indeed the correspondence between the surface tension known from static Laplace Law tests and that surface tension which governs the meso-scale dynamic response of the interface [in eqn. (1)] remains to be assessed in a direct investigation of the normal stress condition.

In any diphasic LBGK fluid, a closed narrow interface maintaining a pressure difference might well have properties different from a simple planar interface but those properties should depend only upon the local orientation of the interface with respect to the lattice and not (*e.g.*) upon the flow field or its derivatives. Thus a meso-scale surface tension, assessed through conditions eqns. (1) and (2) is, we suggest, the most significant interfacial parameter. The need for some re-appraisal is further underlined by the results of previous study on macroscopic surface tension in our diphasic LBGK, reported in ref. 2 in which expressions for *pressure tensor* surface tension, for the two possible stable planar interface orientations, available to the lattice fluid in D2Q9 were derived. These expressions predict an anisotropy which is in good agreement with values measured from simulation and interface anisotropy and probably affects hydrodynamics on the mesoscale.

In this paper, then, we examine *with a generally applicable methodology* the extent to which general hydrodynamic conditions eqns. (1) and (2) are modelled by one particular derivative of the Gunstensen (Rothman–Keller) interface. As a by-product we indicate briefly some modifications which may improve the hydrodynamic properties of the Gunstensen-type diphasic LBGKs.

In Section we define our particular LBGK model, then (Section 3) examine, with a general method, the *tangential* properties of its interface, against the criterion of eqn. (2). Next we assess normal stress behaviour (Section 4).

Generally, in two dimensions, eqns. (1) and (2) may be rephrased into a statement of interfacial hydrodynamics better suited to direct assessment (Section 4). Section 4 also contains an account of one means by which meso-scale measures of *any* LBGK interface may be made. That is, the investigative methods developed in Sections 3 and especially 4 apply to other LBGK interface generating techniques.[12,14]

We present our conclusions in Section 5.

2 Model

Our model uses a core LBGK scheme on the square lattice designated D2Q9: Table 1 of ref. 2 defines its 9 velocities (c_i), $i = 1 \cdots 9$ (links). The density at position x, time t is designated red or blue, and denoted $R_i(x, t)$, $B_i(x, t)$.

Multi-component behaviour arises as colour segregation is imposed by a generalisation of the core LBGK collision step[11] which re-allocates colour to the (net) link density $N_i(x, t) = R_i(x, t + B_i(x, t)$, which is itself perturbed so as directly to insert anisotropy into the pressure tensor $P_{\alpha\beta}(x, t) = \Sigma_i N_i(x, t) c_{i\alpha} c_{i\beta}$.

We use an interface-generating perturbation modified from Gunstensen *et al.*[3] which narrows the interface width, activating this surface tension generating perturbation only on sites occupied by two colours:[2]

$$\Delta N_i(x, t) = \sigma C(x, t) \cos[2(\theta_f - \theta_i)] \quad (3)$$

Here σ is the surface tension parameter controlling the perturbation amplitude, θ_i is the angular orientation of link identified in the subscript and $\theta_f(x, t)$ is the direction of a local colour gradient $f(x, t)$:

$$f(x, t) = \sum_{i,j} (R_j(x + c_i, t) - B_j(x + c_i, t)) c_i \quad (4)$$

and the factor $C(x, t)$ is a weighting concentration factor:

$$C(x, t) = 1 - \left| \frac{\rho_B(x, t) - \rho_R(x, t)}{\rho_B(x, t) + \rho_R(x, t)} \right| \quad (5)$$

the role of which is not without foundation in hydrodynamics[2,20] and in parent lattice gas techniques.[21] A fuller account of our particular interfacial perturbation is contained in ref. 2.

It is appropriate to comment that the interface created after the manner just discussed has, as one expects, a minimum "energy" when aligned parallel with lattice velocity vectors. Any modification to an interfacial perturbation with the general form of eqn. (3) is unlikely to influence this tendency, which is the most significant cause of anisotropy in this model's interfacial tension.

3 Tangential stress condition

In this section we assess the tangential stress condition eqn (2) as it applies to our LBGK interfaces separating a blue/red/blue planar sandwich system (see Fig. 1) which is sheared in the the y-direction.

For this situation, hydrodynamics predicts a linear relation between shear stress and velocity gradient in the bulk of the separated fluids. Defining shear rate $\dot{\gamma}$ in the usual manner:

$$\frac{\partial u_y}{\partial z} = \dot{\gamma} \quad (6)$$

it is easy to show that, for separated, sheared blue and red fluids with different viscosities

$$\dot{\gamma}^{R} \nu^{R} = \dot{\gamma}^{B} \nu^{B} \quad (7)$$

where superscripts refer to the fluid colour in the obvious manner, symbol ν is fluid shear viscosity and $\dot{\gamma}$ the fluid shear

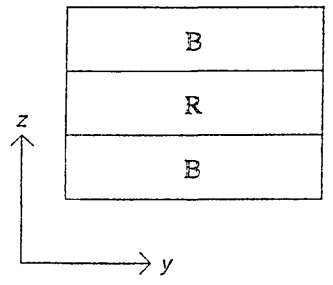

Fig. 1 Schematic of the lattice configuration for tangential stress examination. Periodic conditions were used to close all lattice boundaries, with horizontal forcing (Section 1.2) applied along sites in the lines at the top (bottom) of the top (bottom) blue layer.

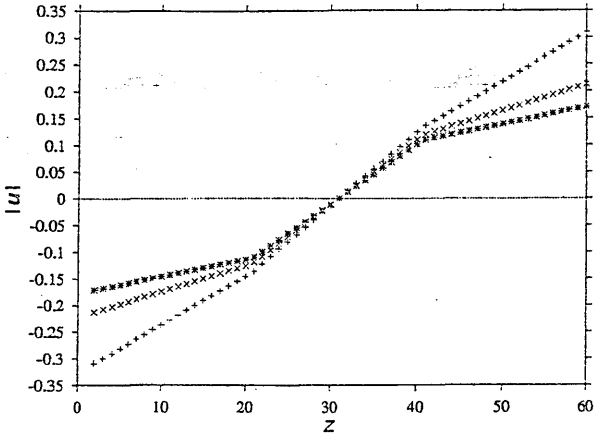

Fig. 2 Variation in y-averaged flow velocity $|u|$ against z for viscosity ratios of 1.5 : 1, 2.5 : 1 and 3.5 : 1.

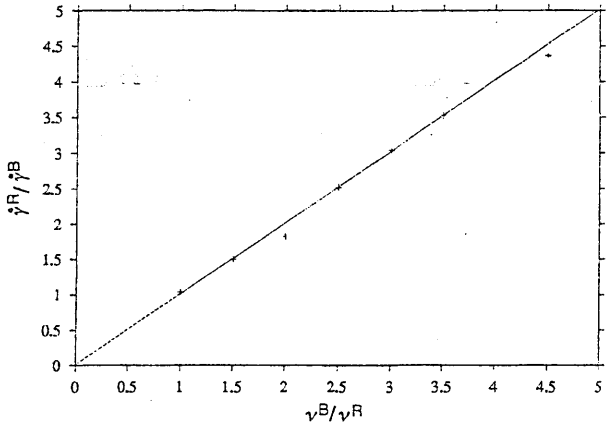

Fig. 3 Variation between $\dot{\gamma}^R/\dot{\gamma}^B$ against ν^B/ν^R.

rate. In addition to eqn. (7) the velocities of the separated red and blue components should match at the interface.

The transmission of tangential stress by our interface was assessed through eqn. (7), by examining the measured ratio between the separated fluids' different shear rates and comparing this with their set viscosities.

With periodic boundary conditions implemented in the y-direction a horizontal (shearing) flow was induced on the system of Fig. 1 by simply incrementing link densities to favour horizontal mass flux in opposite directions at the top and bottom of the lattice at each time step. This particular lattice-edge closure rule easily produces a lattice fluid shear rate controlled through the size to the *forcing* density increment (see *e.g.* ref. 22 for discussion).

The red/blue layers were set to different viscosities through the BGK relaxation parameter ω, the viscosity of mixed sites being controlled through an effective average relaxation parameter:

$$\omega_{\text{eff}} = \frac{\omega^R \rho^R + \omega^B \rho^B}{\rho^R + \rho^B} \tag{8}$$

At the shear rates used all our horizontal planar interfaces were observed to remain singular (one site thick). With a shear directed parallel to the interface, population of links by colour mass in the interfacial node was observed to be qualitatively similar with the static interfaces reported in ref. 2.

The *sandwich* system of Fig. 1 was evolved on a 90 × 60 lattice. Each layer was of approximately equal thickness. Layers were initialised with a viscosity ratio red : blue of 1.5 : 1, 2.5 : 1 and 3.5 : 1. The z-averaged shear rate was then measured in each horizontal fluid layer (in lattice units). Fig. 2, displays the result. It is important to note that the (fully) tangential velocity is clearly continuous across the interface, meeting the hydrodynamic condition of continuity of tangential velocity across an interface.

Separate fits to data from the red/blue layers established individual red/blue shear rates. These ratios correlate very well with the set ratios of red/blue fluid viscosity, as is clear from Table 1 which shows red/blue shear rate ratio against viscosity ratio. Regression to the data of Fig. 3 was found to lend good support to the expected relationship:

$$\dot{\gamma}^R/\dot{\gamma}^B = \nu^R/\nu^B \tag{9}$$

derived from eqn. (7). For the data in this study a surface tension parameter of $\sigma = 0.0125$ was used, with a shear forcing density increment of 0.02,[22] the viscosity ranges were $\nu^R = 0.0294$ (corresponding to a relaxation parameter of $\omega^R = 1.7$) and $0.0140 \leqslant \nu^B \leqslant 0.1471$ ($1.1 \leqslant \omega^B \leqslant 1.7$).

Clearly, these results support the conclusion that tangential stresses are correctly handled by our LBGK interface. This observation assists the analysis of the normal stress behaviour, investigated in the next section.

Table 1 Comparison of viscosity ratios with measured velocity gradient ratios

Viscosity ratio	Velocity gradient ratio
1 : 1.5	1 : 1.505
1 : 2.5	1 : 2.513
1 : 3.5	1 : 3.522

4 Normal stress condition

Consider a red drop in the y–z plane surrounded by a blue fluid of equal density and viscosity, deformed by a flow, which in the blue far-field approximates to a shear. A point on the interface is specified by radial distance r and polar angle θ. In two dimensions the drop deformation may be characterised by a single local radius of curvature $R(\theta)$. The relevant quantities are represented in Fig. 4, in which the unit normal, $\hat{n}$, and (single) unit tangent, $\hat{t}$ at the red/blue interface must be related through:

$$\hat{n}_y = -\hat{t}_z \quad \hat{n}_z = \hat{t}_y \tag{10}$$

When working in two dimensions it is possible to combine normal and tangential boundary conditions eqns. (1) and (2) into a more convenient form.

Using an obvious notation in which, *e.g.*, internal (red) velocity close to the interface is expressed v^R_α, the *normal* contraction of eqn. (1) may be written:

$$p^R - p^B + \sigma'^R_{\alpha\beta} n_\alpha n_\beta - \sigma'^B_{\alpha\beta} n_\alpha n_\beta = \frac{\Sigma}{R(\theta)} \tag{11}$$

where we have used the relationship $\sigma_{\alpha\beta} = p\delta_{\alpha\beta} + \sigma'_{\alpha\beta}$ between stress and viscous stress.[18] The analogous tangential contraction of eqn. (2) may be added to eqn. (11) and, on appeal to

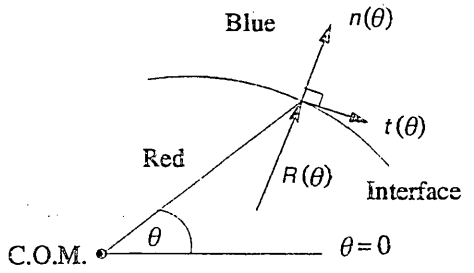

Fig. 4 Schematic of the unit normal and tangent vectors, drawn at a site on a discrete LBGK interface position characterised by angle θ. $R(\theta)$ represents the local radius of curvature of the interface.

the identities of eqn. (10), there results a modified statement of the normal stress condition, valid for two-dimensional situations:

$$p^{R}(\theta) - p^{B}(\theta) + 2\nu^{R}(\partial_y u_y^{R} + \partial_z u_z^{R}) - 2\nu^{B}(\partial_y u_y^{B} + \partial_z u_z^{B}) = \frac{\Sigma}{R(\theta)} \tag{12}$$

in which all derivatives and the hydrostatic pressures are evaluated approaching that interfacial location specified by the polar angle θ . Having already assumed incompressible flow, the separate divergences in eqn. (12) each vanish and for a two-dimensional fluid at the meso-scale:

$$\Delta p(\theta) = \frac{\Sigma}{R(\theta)}, \quad \Delta p(\theta) = p^{R}(\theta) - p^{B}(\theta) \tag{13}$$

in which, recall $R(\theta)$ is the *local* radius of curvature of the interface. So, in two dimensions the usual interfacial conditions are re-phrased into eqn. (13) and tangential stress eqn. (12). Looking back at eqn. (13) we can say that an LBGK model has "physical" hydrodynamics if the measured pressure difference divided by the local radius of curvature gives the same number at all interfacial positions θ.

The results of Section 3 clearly imply that tangential stress conditions eqn. (2) *are* met. To test the normal stress behaviour therefore, we can assess the extent to which diphasic LBGKs are described by eqn. (13).

From calculation on a flat interface, it has been shown that the surface tension of our particular diphasic LBGK varies with the interface's orientation relative to the underlying D2Q9 lattice.[9] And in the narrow interface limit any diphasic LBGK's *meso-scale* interfacial hydrodynamics might be also be complicated by anisotropy. In applying eqn. (13) then, the factor Σ is assumed to have angular variation and we write:

$$\Delta p(\theta) = \frac{\Sigma(\theta)}{R(\theta)} \tag{14}$$

Note we propose eqn. (14) for *2D only*, and then only when tangential stress continuity (Section 3) has been verified. Also, the angular variation of property $\Sigma(\theta)$ is an artifact of the particular model in use and of less interest than any method which may limit its amplitude. Indeed if $\Sigma(\theta)$ is made independent of θ, the hydrodynamics of the technique improves.

Further to assess any two-dimensional diphasic LBGK's hydrodynamics through compliance with eqn. (14), the pressure difference $\Delta p(\theta)$ and local radius of curvature $R(\theta)$ must be obtained for a general angular position θ on the interface (Fig. 4). Our examination of the transmission of normal stress across a red/blue interface therefore proceeds by describing the means by which radius of curvature and pressure jump measurements may be performed on the steady-state of a well-deformed drop.

4.1 Radius of curvature measurements

Take a red drop sheared to a steady-state deformation in a blue fluid (see ref. 22). To determine $R(\theta)$, the centre of red mass is first located from moments of red mass.[22] The coordinates (y, z) of each interface (mixed colour) site, relative to the drop centre may then be used to calculate the polar angle θ subtended by the radius vector (Fig. 4). The interfacial unit normal vector $\hat{n}$ at position θ can be calculated using a Frenet–Serret formula[23]

$$\frac{\mathrm{d}\hat{t}}{\mathrm{d}s} = \kappa\hat{n} \tag{15}$$

where $\hat{t}$ is the unit tangent vector, s is arc length and κ such that $\kappa^{-1} = R(\theta)$. From eqn. (15), the radius of curvature $R(\theta)$ can now be written in terms of the y and z components of the unit tangent:

$$\frac{1}{R(\theta)} = \left|\frac{\mathrm{d}\hat{t}}{\mathrm{d}s}\right| = \left[\left(\frac{\mathrm{d}\hat{t}_y}{\mathrm{d}s}\right)^2 + \left(\frac{\mathrm{d}\hat{t}_z}{\mathrm{d}s}\right)^2\right]^{1/2} \tag{16}$$

in which the square bracket terms must now be written as θ-derivatives. Write

$$\frac{\mathrm{d}\hat{t}}{\mathrm{d}s} = \frac{\mathrm{d}\hat{t}}{\mathrm{d}\theta}\frac{\mathrm{d}\theta}{\mathrm{d}s} = \frac{\mathrm{d}}{\mathrm{d}\theta}\frac{\mathrm{d}r}{\mathrm{d}s}\left|\frac{\mathrm{d}r}{\mathrm{d}\theta}\right|^{-1} \tag{17}$$

where θ is the polar angle, and we have used the definition of the unit tangent $\hat{t}$:

$$\hat{t} = \frac{\mathrm{d}r}{\mathrm{d}s} \tag{18}$$

Noting that:

$$\left|\frac{\mathrm{d}r}{\mathrm{d}\theta}\right|^{-1} = \left[\left(\frac{\mathrm{d}y}{\mathrm{d}\theta}\right)^2 + \left(\frac{\mathrm{d}z}{\mathrm{d}\theta}\right)^2\right]^{-1/2} \tag{19}$$

We may rewrite eqn. (17) using eqns. (18) and (19) as:

$$\frac{\mathrm{d}\hat{t}}{\mathrm{d}s} = \left|\frac{\mathrm{d}r}{\mathrm{d}\theta}\right|^{-1}\frac{\mathrm{d}}{\mathrm{d}\theta}\frac{\mathrm{d}r}{\mathrm{d}s} = \left|\frac{\mathrm{d}r}{\mathrm{d}\theta}\right|^{-1}\frac{\mathrm{d}}{\mathrm{d}\theta}\left[\frac{\mathrm{d}r}{\mathrm{d}\theta}\left|\frac{\mathrm{d}r}{\mathrm{d}\theta}\right|^{-1}\right] \tag{20}$$

Performing the differentiations in eqn. (20) we obtain, for the y and z components of the unit tangent vector, at an interfacial location specified by θ

$$\frac{\mathrm{d}\hat{t}_y}{\mathrm{d}s} = \left|\frac{\mathrm{d}r}{\mathrm{d}\theta}\right|^{-2}\left[\frac{\mathrm{d}^2y}{\mathrm{d}\theta^2} - \frac{\mathrm{d}y}{\mathrm{d}\theta}\left|\frac{\mathrm{d}r}{\mathrm{d}\theta}\right|^{-2}\left(\frac{\mathrm{d}^2y}{\mathrm{d}\theta^2}\frac{\mathrm{d}y}{\mathrm{d}\theta} + \frac{\mathrm{d}^2z}{\mathrm{d}\theta^2}\frac{\mathrm{d}z}{\mathrm{d}\theta}\right)\right] \tag{21}$$

$$\frac{\mathrm{d}\hat{t}_z}{\mathrm{d}s} = \left|\frac{\mathrm{d}r}{\mathrm{d}\theta}\right|^{-2}\left[\frac{\mathrm{d}^2z}{\mathrm{d}\theta^2} - \frac{\mathrm{d}z}{\mathrm{d}\theta}\left|\frac{\mathrm{d}r}{\mathrm{d}\theta}\right|^{-2}\left(\frac{\mathrm{d}^2y}{\mathrm{d}\theta^2}\frac{\mathrm{d}y}{\mathrm{d}\theta} + \frac{\mathrm{d}^2z}{\mathrm{d}\theta^2}\frac{\mathrm{d}z}{\mathrm{d}\theta}\right)\right] \tag{22}$$

The local radius of curvature around a site specified by θ is thus obtained from eqn. (23) (reproduced below) using eqns. (21) and (22) (above) for the s-derivatives of the y and z components of the unit tangent.

$$\frac{1}{R(\theta)} = \left|\frac{\mathrm{d}\hat{t}}{\mathrm{d}s}\right| = \left[\left(\frac{\mathrm{d}\hat{t}_y}{\mathrm{d}s}\right)^2 + \left(\frac{\mathrm{d}\hat{t}_z}{\mathrm{d}s}\right)^2\right]^{1/2} \tag{23}$$

To obtain approximations for the derivatives in eqn. (21), consider the interface site coordinates (y, z) to be functions of θ and write their respective Fourier sine/cosine series representations, each with period π:

$$y(\theta) \approx \frac{a_0}{2} + \sum_n [a_n \sin(n\theta) + b_n \cos(n\theta)] \tag{24}$$

$$z(\theta) \approx \frac{a_0'}{2} + \sum_n [a_n' \sin(n\theta) + b_n' \cos(n\theta)] \tag{25}$$

Clearly, derivatives like the $\mathrm{d}^2z/\mathrm{d}\theta^2$ occurring in eqn. (21) may now be written explicitly in terms of a_0, a_n, a_0', a_n' and b_n' and in turn Fourier amplitudes a_0, a_n and b_n etc. may be approx-

imated at given (measured) θ by numerical integration:

$$a_0 = \frac{1}{\pi}\int_{-\pi}^{\pi} y(\theta)\,\mathrm{d}\theta \approx \frac{1}{\pi}\sum y(\theta_i)\,\Delta\theta_i \quad (26)$$

$$a_n = \frac{1}{\pi}\int_{-\pi}^{\pi} y(\theta)\sin(n\theta)\,\mathrm{d}\theta \approx \frac{1}{\pi}\sum y(\theta_i)\sin(n\theta_i)\,\Delta\theta_i \quad (27)$$

$$b_n = \frac{1}{\pi}\int_{-\pi}^{\pi} y(\theta)\cos(n\theta)\,\mathrm{d}\theta \approx \frac{1}{\pi}\sum y(\theta_i)\cos(n\theta_i)\,\Delta\theta_i \quad (28)$$

$$\Delta\theta_i = |\,\theta_i - \theta_{i-1}\,| \quad (29)$$

where $\Delta\theta_i$ is the (small but irregular) angular interval between neighbouring interfacial sites.

The local radius of curvature, at given θ was thus determined, from a fit to the whole drop interface using eqns. (21)–(23) with the appropriate derivatives obtained from the Fourier components given in (*e.g.*) eqn. (26). As a check, raw co-ordinates (y, z) were obtained from the Fourier components identified in eqn. (26). Fig. 5 displays results for a deformed drop (undeformed radius $R = 40$, $\sigma = 0.005$ and $\omega = 1.5$). By trial and error, fifteen Fourier harmonics ($n < 15$) were found to be sufficient to obtain good agreement between measured and interpolated interface positions.

Fig. 6 graphs the radius of curvature $R(\theta)$ measured for an undeformed drop, which, despite some asymmetry (attributable to the fact that the interface is narrow), exhibits periodicity (over intervals $-\pi \leqslant \theta \leqslant 0$ and $0 \leqslant \theta \leqslant \pi$). The mean value of the collected radius data gives a value of $\bar{R} = 40.236$.

4.2 Pressure 'jump' measurements

Fig. 7 plots pressure (density) and colour against horizontal distance from an undeformed drop centre. Clearly pressure oscillates close to a sharp colour interface, which oscillation, on the meso-scale, must be regarded as an artifact of a Gunstensen-type interface. Other diphasic LBGK algorithms also show variation in density across the interfacial region. What is essentially microscopic physics presenting at the mesoscale is an acknowledged aspect of LBGK simulation in general. Here, to measure a hydrodynamic pressure jump (in a way which will generalise to any diphasic LBGK) we measure

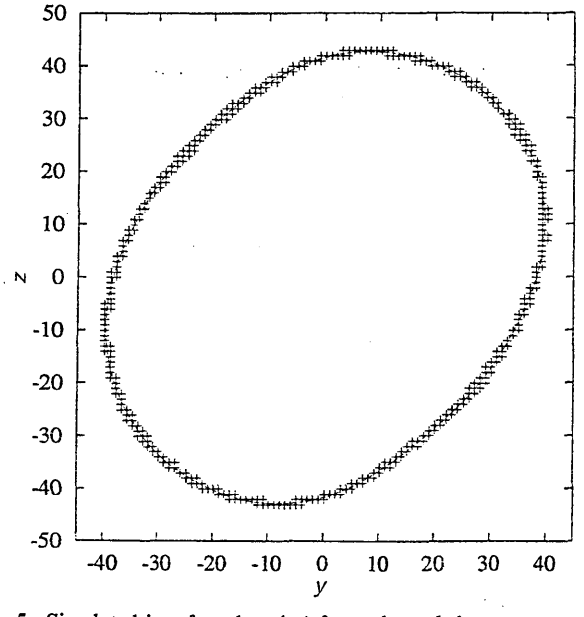

Fig. 5 Simulated interface data (+) for a sheared drop, superposed over the discrete Fourier fit to the interface for a drop with $R = 40$, $\sigma = 0.005$ and $\omega = 1.5$, (solid line).

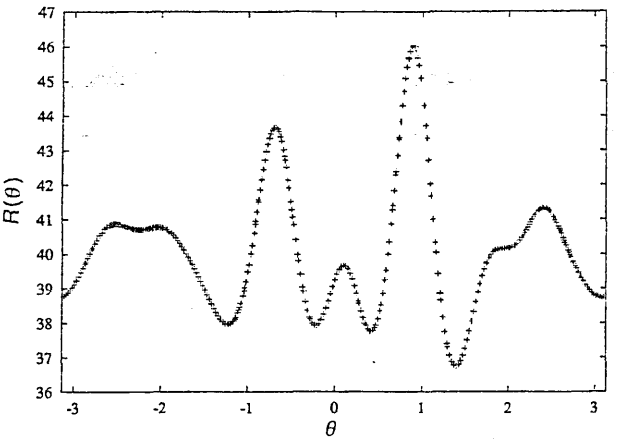

Fig. 6 Radius of curvature $R(\theta)$ against θ for the undeformed drop.

$\Delta p(\theta)$ between two points in the separated liquids which lie as close as possible to the colour interface, are characterised by the same θ, but which lie outside the region in which pressure is influenced by the particular segregation algorithm in use.

Shrinking/expanding the Fourier fit to the interface, by 5 lattice sites (a model-dependent number, small compared with simulation length scales, conditioned by the minimum simulated drop radius) one finds a pair of contours, concentric and locally parallel with the sharp colour interface. One point on each contour may be identified by a value of θ characterising some interfacial node. The two points inevitably lie off-lattice so interpolation between nodes was used to infer red (blue) pressure p(R) [p(B)] and hence hydrostatic pressure jump at polar angle θ. Fig. 8 shows the variation of p(R) and p(B) with polar angle θ. Both sets of data show similar periodic fluctuations. The mean pressure outside the drop is $p \approx 0.6$ (local density $\rho/3$) resulting from an initial value $\rho = 1.8$. The data of Fig. 8 were extracted from a static drop on a 150 × 150 lattice with initial radius $R = 40$, $\omega = 1.5$ and interfacial $\sigma = 0.005$. Internal pressure data exhibits the flattest profile, and does not correlate to the drop radius of curvature as well as the external pressure variation.

4.3 Measurements of meso-scale surface tension

After the discussions of the last two sections we are now in a position to evaluate $R(\theta)$ and $\Delta p(\theta)$ for drops of any shape, and therefore obtain a meso-scale surface tension for our model from eqn. (14).

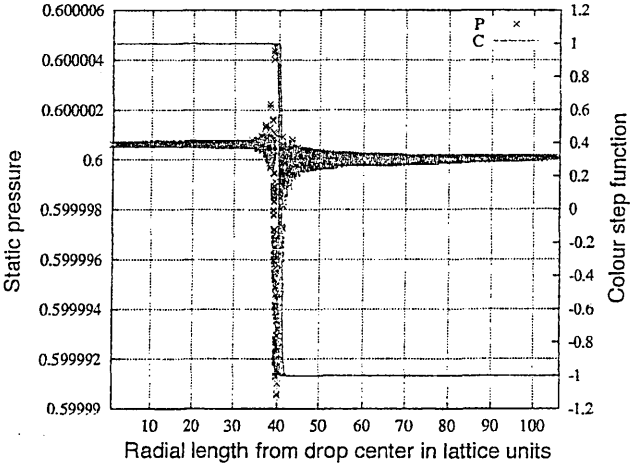

Fig. 7 Pressure and colour interface location as a function of normalised distance from the drop centre. Note that the colour interface is narrow ("singular"), whilst there is a clear oscillation in the pressure close to the interface, especially inside, in the red fluid.

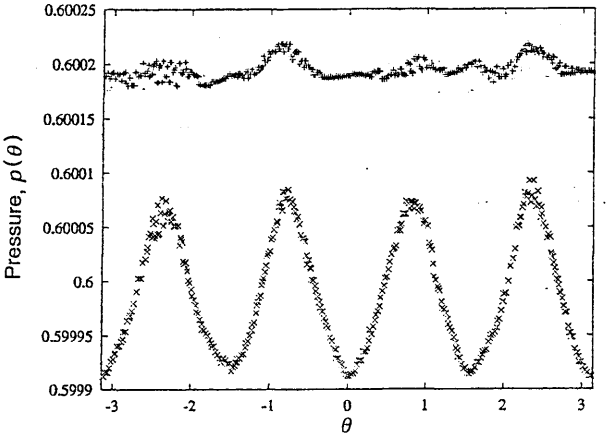

Fig. 3 Variation of static fluid pressure p with polar angle θ, inside the drop the symbol + is used.

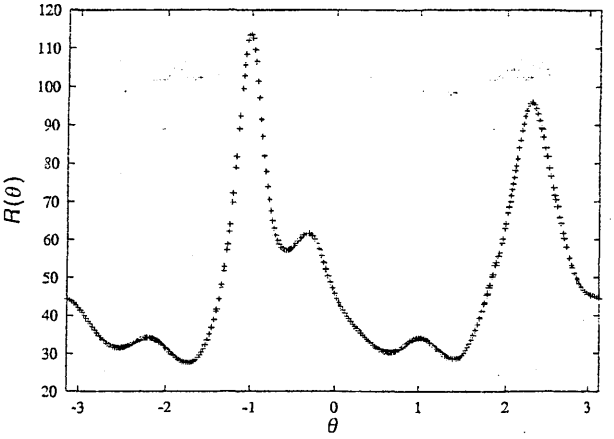

Fig. 10 Radius of curvature $R(\theta)$ against θ for the deformed drop of Fig. 5.

Mesoscopic surface tension $\Sigma(\theta)$, when plotted against polar angle θ (Fig. 9: simulation details as in Fig. 8), has periodic structure consistent with the D2Q9 lattice and confirms that the mesoscopic surface tension $\Sigma(\theta)$, defined through eqn. (14) is anisotropic. With a minimum (maximum) value of $\Sigma(\theta)$, $\Sigma(\theta)_{\min} \approx 0.005$ ($\Sigma(\theta)_{\max} \approx 0.011$), the degree of surface tension anisotropy may be *quantified* by anisotropy factor:

$$A_\sigma = \frac{\Sigma(\theta)_{\max}}{\Sigma(\theta)_{\min}} \tag{30}$$

for the data of Fig. 9, $A_\sigma \approx 2.3$. Note, a single parameter such as A_σ cannot resolve all issues of interface anisotropy: there is in any sharp interface a tendency to adhere to lattice directions (observed in a correlation between measured surface tension and the direction of the interfacial tangent). However, whilst a close examination of the interface's constitution reveals it is mostly single site, its colour structure cannot be compared with that considered in ref. 2, which treats highly uniform, symmetric, *planar* interfaces with symmetric colour distribution and no density gradient or microcurrent.[2] Whilst the drop interface does tend to attach to the lattice (lying parallel to lattice directions) nowhere do we expect there to occur a zero pressure jump or a constant radius of curvature, so the variation observed in Fig. 9 is not covered by theory.[2]

A *standard* Laplace formula measurement of *macroscopic* surface tension is obtained from the mean static pressure inside the drop $\bar{p}^R$ (over a radius of $r \leqslant 32$ lattice units from the drop centre), the external mean pressure $\bar{p}^B$ (over nodes at radius $r \geqslant 48$: as is customary in the literature) and the radius of the drop (taken as the initialised radius of 40 lattice units) using:

$$\Sigma = R(p^{-R} - p^{-B}) \tag{31}$$

For the same drop, *standard* Laplace surface tension $\Sigma = 0.00772$ is recorded, the value of which is close to the mean mesoscopic surface tension, $\bar{\Sigma}(\theta) = 0.00797$, obtained from the data in Fig. 9. The usual Laplace Law surface tension is approximately the average of the local meso-scale surface tension data.

With a *deformed* (sheared) drop we notice strong local peaks in the radius of curvature (Fig. 10), corresponding with locations where the interface becomes tangent to lattice links, equivalent to a tendency of the interface to attach to D2Q9 lattice-link directions. With a narrow interface, curvature spikes are an artifact of the lattice: the former is inclined to align locally parallel with lattice link directions. Though the radius of curvature spikes are more apparent in the meso-scale data for a sheared drop, the underlying angular variation in surface tension (Fig. 11) is very similar to that obtained in static tests (Figs. 8 and 9).

Deformation changes the populations of different interfacial sites and the drop elongates along directions parallel to diagonal D2Q9 lines, with increasing applied shear. This process is clear from comparison of Figs. 9 and 11: equivalent stationary values of mesoscopic surface tension occur at angular positions θ which are slightly offset as a result of shape changes. For example, the same maximum value of mesoscopic surface tension occurs when the interface is parallel to the short links in the z-direction, around $\theta = 0$ rad in an undeformed drop

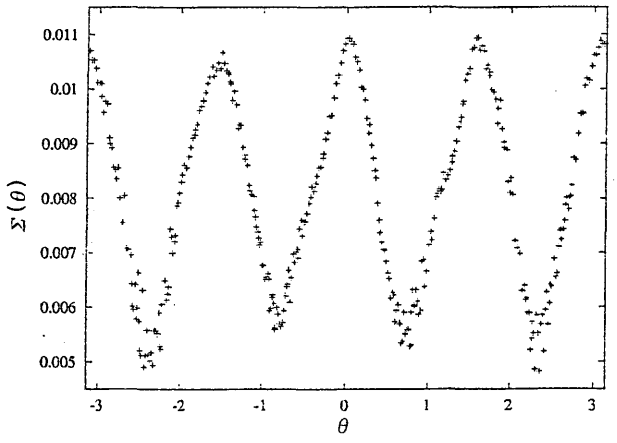

Fig. 9 Variation of macroscopic surface tension $\Sigma(\theta)$ with rotational angle θ.

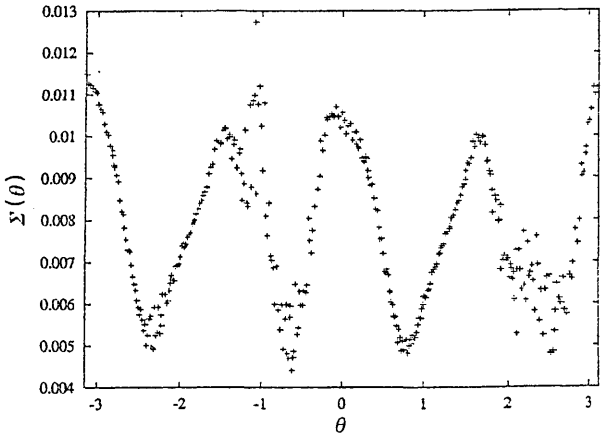

Fig. 11 Variation of macroscopic surface tension $\Sigma(\theta)$ with rotational angle θ for a deformed drop (corresponding radius of curvature data is in Fig. 10).

(Fig. 9) and around polar angle $\theta \approx -0.15$ rad (Fig. 11) in a *deformed*, sheared drop.

That the absolute shape of the drop does not influence the range of observed mesoscopic surface tensions or the interfacial orientations (relative to the lattice) at which the stationary values of surface tension are recorded leads us to the conclusion that, for our Gunstensen-type model, meso-scale surface tension anisotropy is primarily determined by local interfacial orientation, not by macroscopic detail (overall drop shape) and it should be possible to modify the mesoscopic surface tension behaviour using a *local* rule, that is, without recourse to details of the drop shape (*e.g.* radius of curvature).

Qualitatively then, static and deformed drops simulated using our diphasic LBGK model show a surface tension structure generally consistent with the lattice symmetry and "usual" macroscopic Laplace Law surface tension. Of course, for an LBGK interface to support hydrodynamical boundary conditions the meso-scale surface tension should produce flat profiles in Figs. 9 and 11. By modifying a model's interfacial segregation rule one might improve the isotropy of meso-scale surface tension and hence make the LBGK model's interfacial boundary conditions conform better with the defining eqns. (1) and (2).

Now, pressure tensor calculations appear to be a qualitatively correct description of the meso-scale surface tension of drops, so we write:[2]

$$\Sigma(\theta) \sim \frac{\sigma}{\omega} \tag{32}$$

where $\sigma(\omega)$ is the surface tension perturbation amplitude (LBGK relaxation parameter).

To improve meso-scale surface tension anisotropy in any LBGK model, one can vary σ to compete with the measured meso-scale interfacial tension. The detail of the following discussion depends upon the particular model of our study but the general methodology can be applied to any LBGK interface generating rule through its interface parameter.

Meso-scale surface tension should depend only upon the local interface orientation on the lattice. So taking the local colour field direction θ_f (or, in other models, the density gradient) to lie perpendicular to the local interface tangent, one can parametrise interface orientation on the lattice using θ_f, hence decrease $\Sigma(\theta)_{max}$ and increase $\Sigma(\theta)_{min}$ by contriving θ_f dependence in perturbation amplitude σ:

$$\Delta N_i(x, t) = \sigma g(\theta_f) C(x, t) \cos[2(\theta_f(x) - \theta_i)] \tag{33}$$

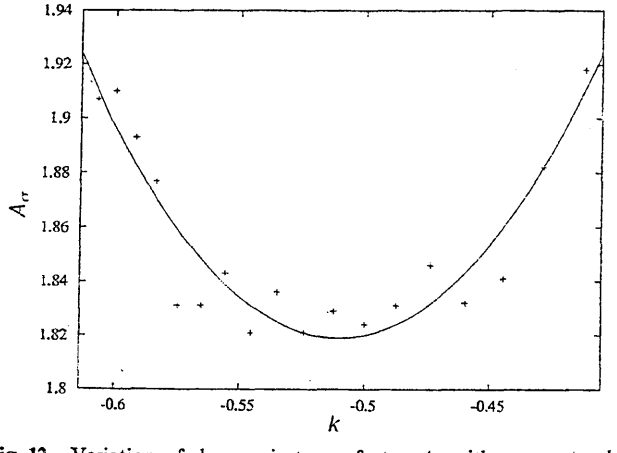

Fig. 12 Variation of drop anisotropy factor A_σ with parameter k, close to the minimum in A_σ. The continuous line fit has the form $ax^2 + bx + c$ for $a = 9.525$, $b = 9.714$ and $c = 4.296$. Outside the range shown anisotropy increases monotonically.

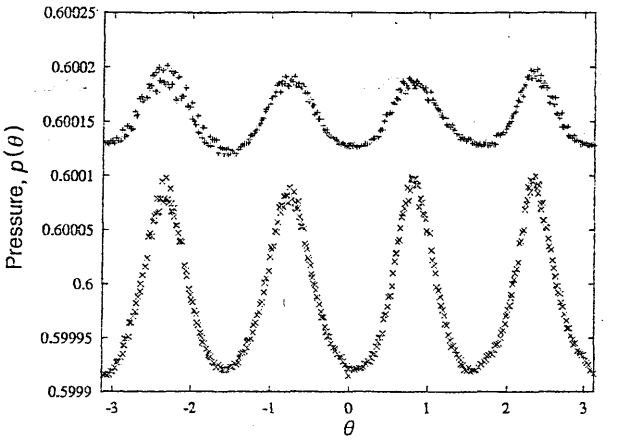

Fig. 13 Variation of static fluid pressure p with rotational angle θ, close to the interface (but see Fig. 8).

where factor $g(\theta_f) = g(\theta_f + \pi/2)$ promotes surface tension isotropy. For our particular interface we may choose

$$g(\theta_f) = \{1 + k\cos^2[2\theta_f(x)]\} \tag{34}$$

in which k is a real parameter $-1 \leqslant k \leqslant 0$ (see Figs. 10 and 11) which may be optimised by considering undeformed drops, for which $\theta_f \approx \theta$, the polar angle of an interfacial length element. Considering eqns. (33) and (34):

$$\Sigma(\theta)' \approx g(\theta)\Sigma(\theta) \tag{35}$$

where $\Sigma(\theta)'$ $[\Sigma(\theta)]$ is the meso-scale surface tension, at polar angle θ from the modified (original) model. From Fig. 9 $\Sigma(\theta)_{max} = \Sigma(0)$, $\Sigma(\theta)_{min} = \Sigma(\pi/4)$ so stating interfacial isotropy as $\Sigma(0)' = \Sigma(\pi/4)'$ use eqn. (35) and definition eqn. (34) to obtain:

$$A_\sigma = \frac{g(\pi/4)}{g(0)} = \frac{1}{1 + k} \tag{36}$$

where we have used *e.g.* $g(0) = 1 + k$. Using a measured value of 2.3 for A_σ we estimate $k = -0.52$, which is supported by simulation (Fig. 12). Comparing Figs. 13 and 8, we note better correlation between pressures on the red and blue sides of our interface, which acts qualitatively to adjust interfacial tension as desired. But the radius of curvature has an essentially unchanged angular variation (from Fig. 10) so Fig. 13 shows only limited reduction of the amplitude of the variation of surface tension, compared with the unmodified algorithm (Fig. 9). Figs. 12–14 were obtained for an undeformed drop of initial radius $R = 40$ on lattices of edge 150×150 with $\sigma = 0.005$ and $\omega = 1.5$.

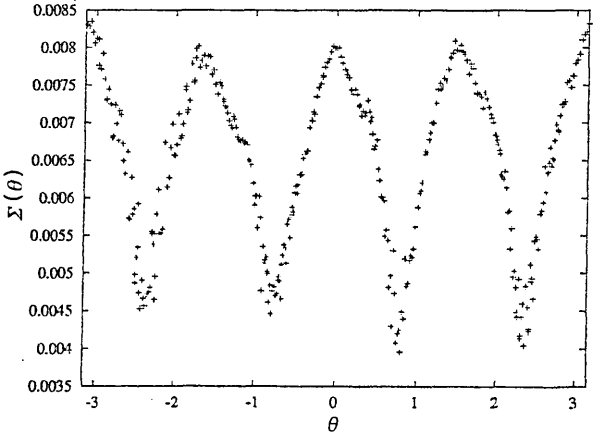

Fig. 14 Variation of macroscopic surface tension $\Sigma(\theta)$ with rotational angle θ.

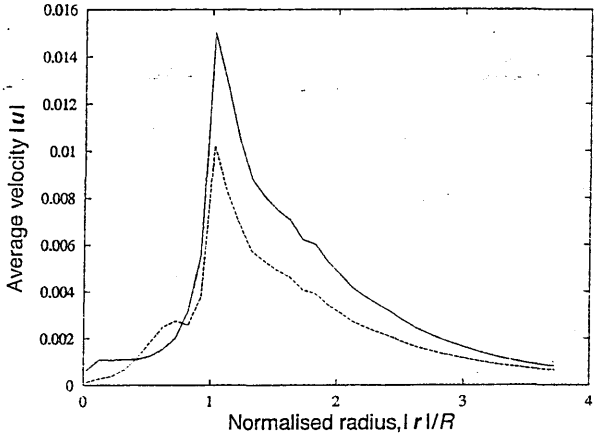

Fig. 15 Variation of $|u|$, microcurrent flow speed measured in units of lattice spacing per time step, against normalised distance from the drop centre, $|r|/R$ at $\sigma = 0.005$ for the unmodified interface (solid line) and the modified interface (broken line) at $k = -0.524$

Fig. 15 shows the spatial variation of microcurrent speed, $|u|$ for our steady-state drop. The solid line shows the angular-averaged magnitude of microcurrent velocity using the unmodified interface perturbation, the broken line with lower maxima shows the magnitude of microcurrent activity using the new algorithm at $k = -0.52$. Comparisons between microcurrents induced in Gunstensen–Rothman–Keller derivative and *e.g.* Shan–Chen interfaces[24] show $|u|_{max}$ is twice as large in the former for similar interface perturbation parameters σ.[25] However a similar process of calibration on a Shan–Chen type model should be straightforward, and would enable that model further to reduce microcurrent intensity.

5 Conclusions

Using as a vehicle a minimalist segregation algorithm, after Gunstensen *et al.*,[3] implemented over a D2Q9 LBGK algorithm, we have highlighted the need *locally* to evaluate the surface tension in any diphasic LBGK, used in the limit of narrow interfaces for simulations in which interfacial hydrodynamics is important.

To assist an analysis we have developed the means by which the general hydrodynamics of the interface may be quantified in two-dimensional LBGK simulations and we have presented a method by which the parameters [local interfacial curvature, pressure difference (see below)] may be obtained for discrete models. From this platform we have measured, at the meso-scale, the anisotropy inherent in our class of LBGK interface from a consideration of stresses across the interface.

Assessing the transmission of tangential stresses across planar interfaces in our LBGK model, *via* simulation measurements of the relationship between the separated fluid shear rates and viscosities, we obtain good hydrodynamics (velocity and stress continuity). The examination of normal stress transmission was supported by a Fourier interface investigation technique developed in Section 4, which is quite general in two dimensions and makes no assumptions about the shape of the fluid drop.

We illustrate how a simple modification to an interfacial algorithm can be used to improve interface properties [eqn. (34)] by adding a compensating oscillation in the interfacial parameter which makes a drop's internal and external pressures correlate with local interface orientation relative to the lattice. But unlike pressure, the interface's local radius of curvature is, we suggest, influenced by the tendency of the interface to adhere to lattice directions, which is probably inevitable in any narrow interface. A diphasic LBGK density perturbation can, on general grounds, do little to adjust this. However we do produce a reduction in the magnitude of the microcurrent.

The local radius of curvature measurement in Fig. 10 is dominated by the interface's tendency to adhere to the lattice. Probably it represents the best attainable (most isotropic) radius of curvature variation for a drop resolved on a D2Q9 lattice as Fig. 10 was found to contain similar structure to an initialised *unevolved* drop: Fig. 10 shows how circular a single-site interface drop can be made on the lattice. Pressure differences do not appear to drive radius of curvature and we suggest that the interface in all classes of LBGK interface (and thereby radius of curvature) needs to be liberated from the lattice to allow the shape of the interface, as it were, more scope to adapt to local flow conditions. One means to achieve this might be to ensure that the colour field always lies normal to interface *i.e.* that the interface always lies perpendicular to the local colour gradient and that the segregating colour fluxes always direct along the colour field (in the present model segregating colour is allocated according to a tractable rule which does not ensure that the flux lies perpendicular to the interface).

References

1 M. R. Swift, W. R. Osborn and J. M. Yeomans, *Phys. Rev. Lett.*, 1995, **75**, 830.
2 I. Halliday, C. M. Care and S. P. Thompson, *Phys. Rev. E*, 1998, **57**(1), 514.
3 A. K. Gunstensen, D. H. Rothman, S. Zaleski and G. Zanetti, *Phys. Rev. A*, 1991, **43**(8), 4320.
4 U. Frisch, D. d'Humieres, B. Hasslacher, P. Lallemand, Y. Pomeau and J. P. Rivet, *Complex Syst.*, 1987, **1**, 649 and references therein.
5 R. Benzi, S. Succi and M. Vergassola. *Phys. Rep.*, 1992, **22**(3), 145.
6 Y. H. Qian, S. Succi and S. A. Orszag, *Annu. Rev. Comput. Phys.*, 1995, **3**, 195.
7 H. Chen, S. Chen and W. H. Matthaeus, *Phys. Rev. A*, 1992, **45**(8), R5339.
8 D. d'Humieres, P. Lallemand and U. Frisch, *Europhys. Lett.*, 1986, **56**, 1505.
9 F. Higuera and J. Jimenez, *Europhys. Lett.*, 1989, **9**, 7, 663.
10 F. Higuera, S. Succi and R. Benzi, *Europhys. Lett.*, 1989, **9**(4), 345.
11 Y. H. Qian, D. d'Humieres and P. Lallemand, *Europhys. Lett.*, 1992, **17**(6), 479.
12 X. W. Shan and H. D. Chen, *Phys. Rev. E*, 1994, **49**(4), 2941.
13 I. Halliday and C. M. Care, S. Thompson and D. White, *Phys. Rev. E*, 1996, **54**(3), 2573.
14 A. J. Wagner and J. M. Yeomans, *J. Mod. Phys. C*, 1997, **8**(4), 773.
15 E. Orlandini, M. R. Swift and J. M. Yeomans, *Europhys. Lett.*, 1995, **32**, 463.
16 E. Orlandini, G. Gonnella and J. M. Yeomans, *Physica A*, 1997, **240**(1–2), 277.
17 D. H. Rothman and S. Zaleski, *Rev. Mod. Phys.*, 1994, **52**, 1417.
18 L. D. Landau and E. M. Lifshitz, *Fluid Mechanics*, Pergamon Press, Oxford, UK, 1966.
19 G. K. Batchelor, *An Introduction to Fluid Mechanics*, Cambridge University Press, Cambridge, UK, 1973.
20 J. S. Rawlinson and B. Widom, *Molecular Theory of Capilarity*, Oxford University Press, London, UK, 1989.
21 D. H. Rothman and J. M. Keller, *J. Stat. Phys.*, 1988, **52**(3–4), 1119.
22 I. Halliday and C. M. Care, *Phys. Rev. E*, 1995, **53**(3), 1602.
23 M. R. Speigel, *Vector analysis and an introduction to Tensor analysis, Schaum's Outline Series*, McGraw–Hill, New York, USA, 1959.
24 S. Chen, G. D. Doolen, K. Eggert, D. Grunau and Y. E. Loh, *Phys. Rev. A*, 1994, **43**(12), 7053.
25 S. Hou, X. Shan, Q. Zou, G. D. Doolen and W. E. Soll, *J. Comput. Phys.*, 1997, **138**(2), 695.

Paper 8/09793C